

**Computational studies of the
electronic structure of transition
metal and p-block compounds**

Eva Linnea Forslund

University College London

Thesis submitted for the degree of Ph.D. in Chemistry



ProQuest Number: U643440

All rights reserved

INFORMATION TO ALL USERS

The quality of this reproduction is dependent upon the quality of the copy submitted.

In the unlikely event that the author did not send a complete manuscript and there are missing pages, these will be noted. Also, if material had to be removed, a note will indicate the deletion.



ProQuest U643440

Published by ProQuest LLC(2016). Copyright of the Dissertation is held by the Author.

All rights reserved.

This work is protected against unauthorized copying under Title 17, United States Code.
Microform Edition © ProQuest LLC.

ProQuest LLC
789 East Eisenhower Parkway
P.O. Box 1346
Ann Arbor, MI 48106-1346

Abstract

A series of calculations, using time-dependent density functional theory as implemented in the Amsterdam Density Functional (ADF) program, have been carried out on 2,3-dialkynyl-1,4-diazabuta-1,3-diene palladium molecules and their complexes in order to determine their electronic excitation energies for comparison with experimental UV/Vis absorption spectra. A molecular orbital explanation is presented for the bathochromic shift which occurs when hydrogen is substituted for a dimethyl amino-group in the para position of the aryl rings of the free ligands. The near infrared (NIR) absorption in the free diazabutadiene is found to be a HOMO→LUMO transition, and the bathochromic shift was found to be due to a destabilising antibonding interaction between the $N_{NMe_2} p_\pi$ and the aryl ring in the HOMO. It was found that palladium stabilises the LUMO and hence complexation reduces the HOMO-LUMO gap, causing a further bathochromic shift of the NIR absorption.

The bond energies of the diatomic halogens ($F_2 \rightarrow I_2$) have been studied, using the ADF program, to gain an understanding of why F_2 has an unusually low bond energy. The low F-F bond energy was found to be the result of a lower than expected electrostatic energy at the equilibrium bond length. This in turn is due to large electron-electron repulsion of F charge clouds. The gain in the electrostatic energy that occurs when the bond length is decreased from equilibrium is, however, outweighed by the increase in Pauli repulsion energy which is greater in F_2 than in the heavier halogens due to the more rapidly varying orbital overlap.

The potential energy surface of the $ClO + HO_2$ reaction has been studied using the ADF program and the results compared with published data obtained using various

ab initio and hybrid-DFT methods. The reaction was found to take place either on a singlet surface to form HCl and O₃ via a transition state, or on the triplet surface to form HOCl and O₂(³Σ) without any activation barrier being present. No other transition state besides the one mentioned above could be found due to a variety of computational problems. Similar problems occurred when using the Gaussian 98 program, suggesting that DFT calculations on these type of radical reactions should be treated with caution.

Abbreviations

ADF	-Amsterdam Density Functional
AO	-Atomic Orbital
BO	-Born-Oppenheimer
CCSD(T)	-Coupled Cluster with Single, Double and perturbative Triple excitations
COSMO	-Conductor-like Screening Model
DAD	-1,4-diazabuta-1,3-diene
DCM	-Dichloromethane
DFT	-Density Functional Theory
GGA	-Generalised Gradient Approximation
GTO	-Gaussian-type Orbital
HF	-Hartree-Fock
HOMO	-Highest Occupied Molecular Orbital
i-Pr (ⁱ Pr)	-iso-propyl
L	-Ligand
LDA	-Local Density Approximation
LUMO	-Lowest Unoccupied Molecular Orbital
M	-Metal
Me	-Methyl
MO	-Molecular Orbital
MP2	-Møller-Plesset second-order perturbation theory

NIR	-Near Infrared
PDT	-Photodynamic therapy
R, R'	-Substituents
SCF	-Self-Consistent Field
SOC	-Spin-Orbit Coupling
STO	-Slater-type Orbital
TD-DFT	-Time-dependent Density Functional Theory
TDHF	-Time-dependent Hartree-Fock
XC	-Exchange-Correlation
ZORA	-Zeroth Order Regular Approximation

Acknowledgement

First of all I would like to thank both my supervisors. Dr. Rüdiger Faust for giving me the opportunity to do a PhD at UCL. Dr. Nikolas Kaltsoyannis for introducing me to the world of computational chemistry and for all your encouragement and help.

Thanks to Emma O'Grady for valuable discussions throughout the past few years and for your help with proofreading this thesis.

Thanks to everyone, past and present, in G19 and G25, and the Faust group for making the atmosphere so pleasant.

Thanks to the Chemistry Department for the teaching assistant scholarship.

At last I would like to thank my parents for all their support and encouragement, not only during my years in London but through all my life.

Contents

1	Theoretical and Computational Considerations	1
1.1	Schrödinger Equation	2
1.2	Hartree-Fock Approximation	3
1.3	History of DFT	6
1.4	Exchange-Correlation Functional	8
1.5	Basis Sets	11
1.6	Calculating Excitation Energies using Time-Dependent Density Functional Theory	13
1.7	Relativistic Effects	15
1.8	The Amsterdam Density Functional Code	18
1.8.1	The Conductor-like Screening Model of Solvation	18
1.8.2	Ziegler-Rauk Energy Decomposition Scheme	21
1.9	Other Computational Methods	22
1.10	Overview of Thesis	23
2	General computational and experimental details	25
2.1	Computational details	25
2.2	Experimental details	26

3	Electronic Transition Energies in 1,4-diazabuta-1,3-diene Compounds and their Complexes with Palladium	28
3.1	Introduction	28
3.2	Determining the Most Suitable Computational Parameters	33
3.2.1	Basis Set	34
3.2.2	Exchange-Correlation Functional	36
3.2.3	Solvent Surface	37
3.2.4	Conclusions	37
3.3	Comparison of Experimental and Calculated Geometries	39
3.3.1	Gas-phase Molecular Geometries	39
3.3.2	Molecular Geometry in Solution	40
3.3.3	Conclusions	42
3.4	Electronic Transitions and UV/Vis Spectra of 1,4-diazabuta-1,3-dienes	44
3.4.1	Comparison of the Calculated Electronic Absorption Spectrum of 2 with the Experimentally Determined Spectrum of 1	44
3.4.2	Comparison of the Calculated and Experimental Electronic Absorption Spectrum of 1	47
3.4.3	Comparison of the Calculated Electronic Absorption Spectrum of 6 with the Experimentally Determined Spectrum of 5	50
3.4.4	Comparison of the Calculated Spectrum of 10 with the Experimentally Determined Spectrum of 9	54
3.4.5	Comparison of the Calculated Spectrum of 14 with the Experimentally Determined Spectrum of 13	55

3.4.6	Conclusions	58
3.5	Electronic Transitions and UV/Vis Spectra of 1,4-diazabuta-1,3-diene Palladium(II) complexes	60
3.5.1	Importance of Exchange-Correlation Functional in Palladium Complexes	60
3.5.2	Importance of Basis Set in Palladium Complexes	64
3.5.3	Comparison of Experimental and Calculated Geometries of the Palladium Complexes	66
3.5.4	The Calculated Electronic Structure of 4 and Comparison of the Calculated Electronic Absorption Spectrum of 4 with the Experimentally Determined Spectrum of 3	67
3.5.5	Comparison of the Calculated Electronic Absorption Spec- trum of 8 with the Experimentally Determined Spectrum of 7	73
3.5.6	Comparison of the Calculated Electronic Absorption Spec- trum of 12 with the Experimentally Determined Spectrum of 11	78
3.5.7	Comparison of the Calculated Electronic Absorption Spec- trum of 16 with the Experimentally Determined Spectrum of 15	81
3.5.8	Further Studies of Electronic Excitation Energies in Diaza- butadiene Palladium Complexes	84
3.5.9	Solvent Dependence of 7	89
3.5.10	Conclusions	91

4	The Strength of the X₂ Bond; X=F, Cl, Br, I	93
4.1	Introduction	93
4.2	Determining the Most Suitable Computational Parameters	97
4.2.1	Exchange-Correlation Functional	97
4.2.2	Basis Set	105
4.2.3	Spin-Orbit Coupling	107
4.2.4	Conclusions	108
4.3	Population Analysis	108
4.4	Energy Decomposition	110
4.5	Conclusions	117
5	Investigations of the Potential Energy Surface of the ClO + HO₂	
	Reaction	119
5.1	Introduction	119
5.2	Computational Details	123
5.3	Studies of the Potential Energy Surface using the ADF Program . . .	124
5.3.1	Singlet Surface	124
5.3.2	Triplet Surface	129
5.4	Studies of the Potential Energy Surface using the Gaussian 98 Program	131
5.5	Conclusions	133
A	Procedure for the synthesis of N,N'-bis(phenyl)-1,6-bis(triisopropylsilyl)-	
	hexa-1,5-diyne-3,4-diimine palladium dichloride (compound 3, chapter 3)	134
	Bibliography	135

List of Figures

1.1	COSMO surfaces	20
3.1	General structure of the N,N'-phenyl-2,3-dialkynyl-1,4-diazabuta-1,3-dienes.	30
3.2	General structure of the N,N'-phenyl-2,3-dialkynyl-1,4-diazabuta-1,3-diene metal complexes.	31
3.3	Schematic representation of the DAD ligands and corresponding palladium complexes discussed in this study.	33
3.4	The relative total bonding energy of 2 as a function of the N-C ₁ -C ₁ '-N dihedral angle.	41
3.5	The change in transition energies and oscillator strength when gradually changing the C ₁ -N-C ₄ -C ₅ dihedral angle, i.e. rotation of the aryl rings.	42
3.6	The relative bond energy of 2 as a function of the C ₁ -N-C ₄ -C ₅ dihedral angle.	43
3.7	The experimental UV/Vis absorption spectrum of 1 and the simulated spectrum of 2 . The intensity of the longest wavelength peak in the simulated spectrum of 2 has been set equal to that in 1	44
3.8	Three dimensional representations of selected MO's of 2	46

3.9	The experimental and simulated UV/Vis absorption spectrum of 1 . The intensity of the longest wavelength peak in the experimental spectrum has been set equal to that in the simulated spectrum.	48
3.10	The experimental UV/Vis absorption spectrum of 5 and the simu- lated spectrum of 6 . The intensity of the longest wavelength peak in the simulated spectrum of 6 has been set equal to that in 5	52
3.11	Three-dimensional representation of the HOMO (32b) of 6	52
3.12	The simulated spectrum of 4 using two different exchange correlation functionals; LDA(VWN) and GGA(BP86).	61
3.13	Molecular orbital energy level diagram for 4	68
3.14	Three dimensional representations of selected MOs of 4	69
3.15	The experimental UV/Vis absorption spectrum of 3 (solid line) and the simulated spectrum of 4 (dashed line). The intensity of the most intense band in the simulated spectrum of 4 has been set equal to that of the longest wavelength transition band in 3	71
3.16	Molecular orbital energy level diagram of 8	75
3.17	The experimental UV/Vis absorption spectrum of 7 (solid line) and the simulated spectrum of 8 (dashed line). The intensity of the longest wavelength peak in 7 has been set equal to that of the second longest wavelength peak in the simulated spectrum of 8	75
3.18	Three dimensional representations of selected MOs of 8	77
3.19	Molecular orbital energy level diagram for 12	79
3.20	Molecular orbital energy level diagram for 16	82
3.21	Molecular orbital energy level diagrams for 4 , 8 , 12 and 16	85
3.22	Molecular orbital energy level diagrams for 2 , 6 , 4 and 8	88

3.23	Absorption spectra for 7 in different solvents. The dielectric constant is given next to the solvent.	89
4.1	Difference between X-only and VWN as the LDA option using two common GGA functionals and the QZ4P basis set. Red=BP86, green=PW91.	101
4.2	A selection of calculated bond energies for X ₂ (X=F, Cl, Br, I) using different GGA functionals with X-only for the LDA part. Blue=Perdew, red=PBEc and green=PW91c.	103
4.3	Decomposition of the bond energy, <i>E</i> , in F ₂ when changing the F-F bond distance. <i>E</i> ^{elstat} =electrostatic energy; <i>E</i> ^{Pauli} =Pauli repulsion energy; <i>E</i> ^{oi} =orbital interaction energy.	111
4.4	Energy decomposition analysis terms at equilibrium bond distance. .	112
4.5	Pauli repulsion energy (hashed line) and total overlap (solid line) as a function of change in bond length from <i>r</i> _{eqm}	116
5.1	The energies of the stationary points on the ClO + HO ₂ potential energy singlet and triplet surface relative to a zero for the reactants, as obtained at the CCD//CCSD(T) level of theory.	125
5.2	Ball and stick representations of the stationary points on the ClO + HO ₂ singlet potential energy surface as obtained at CCD level of theory.	125
5.3	Ball and stick representations of the stationary points on the ClO + HO ₂ singlet potential energy surface.	127
5.4	The energies of the stationary points on the ClO + HO ₂ potential energy surface relative to a zero for the reactants using the BP86 functional and the TZP basis set.	128

5.5	Ball and stick representations of the stationary points on the ClO + HO ₂ triplet potential energy surface as obtained at CCSD(T) level of theory.	129
5.6	The relative energy as a function of the O1-H distance using min4 (hashed line) or ts6 (solid line) as the fixed geometry.	130

List of Tables

3.1	Comparison of the effect of different aryl substituents and metals on the longest wavelength absorption in DCM.	31
3.2	Calculated wavelengths (nm), transition energies (eV) and oscillator strengths and orbital characteristics of the bands in the UV/Vis spectra of planar 2 with different basis sets using the LDA.	35
3.3	Calculated wavelengths (nm), transition energies (eV) and oscillator strengths for planar 2 with different exchange-correlation functionals and the DZP basis set. Transitions with the same MO character (not given) are grouped together horizontally.	36
3.4	Calculated wavelengths (nm), transition energies (eV) and oscillator strengths for planar 2 with different solvent surfaces using the LDA(VWN) functional and the DZP basis set. Transitions with the same MO character are grouped together horizontally.	38
3.5	Selected computational and experimental geometric parameters for DAD molecules. Bond lengths are given in Å and bond/dihedral angles are given in °. The atom and compound numbering scheme is given in figure 3.3 on page 33.	40

3.6	Experimental and calculated wavelengths and energies, and calculated orbital characteristics of the bands in the UV/Vis spectra of 1 and 2 . All transitions are of ${}^1B \leftarrow {}^1A$ symmetry.	45
3.7	Experimental and calculated wavelengths and energies, and calculated orbital characteristics of the bands in the UV/Vis spectra of 5 and 6 . All transitions are of ${}^1B \leftarrow {}^1A$ symmetry.	50
3.8	Calculated wavelength (nm), energies (eV), oscillator strengths and excitation coefficients, calculated for 10 and obtained experimentally for 9 . The calculated orbital characteristics are also presented.	57
3.9	Calculated wavelength (nm), energies (eV), oscillator strengths and excitation coefficients, calculated for 14 and obtained experimentally for 13 . The calculated orbital characteristics are also present.	57
3.10	Calculated wavelengths (nm), transition energies (eV) and oscillator strengths for the band around 400 nm in 4 , using different exchange correlation functionals and rotating the aryl rings around $C_1-N-C_4-C_5$	62
3.11	Calculated wavelengths (nm), transition energies (eV) and oscillator strengths for the band around 400 nm in 4 , using different XC-functionals and with the aryl rings fixed at $C_1-N-C_4-C_5=62^\circ$. The XC-functional used in the geometry optimisation is given first, followed by the XC-functional used in the calculation of excitation energies.	63

3.12	Calculated wavelengths (nm), transition energies (eV) and oscillator strengths for 4 at the geometry optimised with and without a 4f polarisation function in the basis set of palladium. The transition energies are calculated with the same basis set that was used to optimise the geometry.	65
3.13	Selected experimental and computational geometric parameters for 11 and 12 respectively. Bond lengths are given in Å, bond/dihedral angles are given in °.	66
3.14	Experimental and calculated wavelengths and energies, and calculated orbital characteristics of the bands in the UV/Vis spectra of DAD Palladium complexes. Calculated wavelengths and energies have been modified according to equation 3.1.	71
3.15	Experimental and calculated wavelengths and energies, and calculated orbital characteristics of the bands in the UV/Vis spectra of DAD Palladium complexes. Calculated wavelengths and energies have been modified according to equation 3.1.	76
3.16	Wavelength (nm), energies (eV), extinction coefficients and oscillator strengths, calculated for 12 and obtained experimentally for 11 . The calculated orbital characteristics are also presented.	78
3.17	Wavelength (nm), energies (eV), extinction coefficients and oscillator strengths, calculated for 16 and obtained experimentally for 15 . The calculated orbital characteristics are also presented.	81
3.18	Calculated wavelength (nm), energies (eV) and oscillator strengths for H, NMe ₂ , F and Cl substituted complexes (adjusted by equation 3.1).	87

3.19	Calculated and experimental wavelength (nm) and energies (eV) for the low energy transition in 8 in different solvents (adjusted by equation 3.1).	90
4.1	The effect of the London dispersive energy (E_L) on the dissociation energy (D_0) of the X_2 molecules according to two different studies. Energies in kJ/mol.	94
4.2	Bond energies (kJ/mol) for the diatomic halogen molecules. No zero point energies (ZPE) are included unless stated.	98
4.3	Selection of calculated bond lengths (\AA) using different XC-functionals. X-only was used for the LDA part of the XC-functional.	104
4.4	Selection of calculated vibrational frequencies (cm^{-1}) using different XC-functionals. X-only was used for the LDA part of the XC-functional.	105
4.5	Bond energies (kJ/mol) obtained using different basis sets. No spin-orbit coupling was included.	106
4.6	Bond lengths, total bonding energies and frequencies calculated using the X-only/PW91x/PBEc functional and QZ4P basis set.	109
4.7	% contribution to valence π_g , π_u and σ_g MOs. Minimum contribution 1%.	110
4.8	Sum of all overlaps in the S -matrix and the electrostatic energy for F_2 , Cl_2 , Br_2 and I_2 at their equilibrium bond distance.	114
4.9	Optimised bond distance r (\AA) and electrostatic energy (kJ/mol) for the first three diatomic molecules in the chalcogen series and the halogen series.	115

4.10	Energy decomposition of the bond energy (kJ/mol) for F_2 at different bond distances.	115
5.1	Possible reaction channels for the $ClO + HO_2$ reaction.	120

Chapter 1

Theoretical and Computational Considerations

In this thesis three different projects in the field of computational chemistry are presented; a study of the electronic transition energies in 1,4-diazabuta-1,3-diene compounds and their palladium complexes, a bond energy decomposition analysis of the X_2 bond ($X=F$, Cl, Br or I) and finally a study of the potential energy surface of the $ClO + HO_2$ reaction.

The majority of the calculations in all three studies have been carried out using Density Functional Theory (DFT) and thus I will start by explaining the theory behind this methodology and the different DFT applications employed in the works presented herein. A short introduction to some *ab initio* methods used will also be given.

DFT is based on the electron density-dependent energy functional in contrast to most other electronic structure theories which contain the wavefunction dependent energy functional. Despite this, DFT has many similarities with traditional Hartree-Fock (HF) theory (particularly in the way in which it is applied to molecular systems)

since in the 1960s when DFT was developed, HF theory was already mature and so it made sense to follow a similar route to HF theory. Thus a brief introduction to HF theory will be given before introducing DFT. Some typical features of DFT will then be discussed and a description of the Amsterdam Density Functional (ADF) program will be given together with some of its applications.

1.1 Schrödinger Equation

The Schrödinger equation can be used to describe any molecular electronic system and is written as:

$$\hat{H}\Psi = E\Psi \quad (1.1)$$

where, in atomic units,

$$\hat{H} = -\frac{1}{2} \sum_{i=1}^N \nabla_i^2 - \frac{1}{2} \sum_{A=1}^M \frac{1}{M_A} \nabla_A^2 - \sum_{i=1}^N \sum_{A=1}^M \frac{Z_A}{r_{iA}} + \sum_{i=1}^N \sum_{j>i}^N \frac{1}{r_{ij}} + \sum_{A=1}^M \sum_{B>A}^M \frac{Z_A Z_B}{R_{AB}} \quad (1.2)$$

M indexes the nuclei and N the electrons. The first two terms in \hat{H} are the kinetic energy of the electrons and the nuclei. The other terms are the potential energy due to nucleus-electron, electron-electron and nucleus-nucleus interactions. The Laplacian operator, ∇^2 , is the sum of the differential operators

$$\nabla^2 = \frac{\partial^2}{\partial x^2} + \frac{\partial^2}{\partial y^2} + \frac{\partial^2}{\partial z^2} \quad (1.3)$$

Since the mass of a nucleus is so much greater than that of an electron, the nuclei are essentially stationary compared to the electrons. This leads to a first approximation of the Schrödinger equation called the Born-Oppenheimer approximation. If the nuclei are in a fixed position their kinetic energy is zero and the potential energy due to nucleus-nucleus repulsion is constant. The simplified Hamiltonian can thus

be written as

$$\hat{H} = -\frac{1}{2} \sum_{i=1}^N \nabla_i^2 - \sum_{i=1}^N \sum_{A=1}^M \frac{Z_A}{r_{iA}} + \sum_{i=1}^N \sum_{j>i}^N \frac{1}{r_{ij}} \quad (1.4)$$

and the energy obtained from this Hamiltonian is added together with the potential energy from the nucleus-nucleus repulsion to obtain the total energy of the system.

To find the most accurate wavefunction all electronic structure theories employ the Variation principle to some extent. The Variation principle states that the exact energy can only be found if the exact wavefunction is used and any other energy is higher than the real energy, i.e.

$$\langle \Psi | \hat{H} | \Psi \rangle \geq \langle \Psi_0 | \hat{H} | \Psi_0 \rangle \quad (1.5)$$

with Ψ_0 being the exact wavefunction.

To find this exact wavefunction, the functional $E[\Psi]$ needs to be minimised by searching through all acceptable N -electron wavefunctions.

$$E_0 = \min_{\Psi \rightarrow N} E[\Psi] = \min_{\Psi \rightarrow N} \langle \Psi | \hat{T} + \hat{V}_{ne} + \hat{V}_{ee} | \Psi \rangle \quad (1.6)$$

An acceptable wavefunction has to be quadratic integrable and continuous everywhere. Added to this is the criterion of antisymmetry on interchanging two electrons, to obey the Pauli exclusion principle.

$$\Psi(\vec{x}_1, \vec{x}_2, \dots, \vec{x}_i, \vec{x}_j, \dots, \vec{x}_N) = -\Psi(\vec{x}_1, \vec{x}_2, \dots, \vec{x}_j, \vec{x}_i, \dots, \vec{x}_N) \quad (1.7)$$

1.2 Hartree-Fock Approximation

Since it is virtually impossible to go through all acceptable N -electron wavefunctions to find the minimum energy and hence the exact function, a subset is created. To do this, most wavefunction based quantum chemical methods make use of the HF approximation.

The wavefunction can be approximated by a Slater determinant of N one-electron wavefunctions called spin-orbitals or molecular orbitals (MO's), $\phi(\vec{x})$, where the columns represent the spin-orbitals and the rows represent the electrons.

$$\Phi = \frac{1}{\sqrt{N!}} \begin{vmatrix} \phi_1(\vec{x}_1) & \phi_2(\vec{x}_1) & \dots & \phi_N(\vec{x}_1) \\ \phi_1(\vec{x}_2) & \phi_2(\vec{x}_2) & \dots & \phi_N(\vec{x}_2) \\ \vdots & \vdots & & \vdots \\ \phi_1(\vec{x}_N) & \phi_2(\vec{x}_N) & \dots & \phi_N(\vec{x}_N) \end{vmatrix} \quad (1.8)$$

The spin-orbitals have to be orthonormal, i.e. they have to be orthogonal in space and normalised so that the probability of finding an electron in the orbital is unity. They can be approximated as a linear combination of atomic orbitals (LCAO) or basis functions, χ ,

$$\phi_i = \sum_{y=1}^b c_{yi} \chi_y \quad (1.9)$$

where c_{yi} is a coefficient and b is the total number of functions required to represent ϕ_i . The basis functions will be discussed further in section 1.5. The spin-orbitals are the only flexible part in the Slater determinant and are therefore the part that is varied to obtain the lowest energy of the subset. This is done through the use of the Lagrangian multipliers, leading ultimately to the HF equation which may be written as

$$\hat{f}_i \phi_i = \varepsilon_i \phi_i \quad i = 1, 2, \dots, N \quad (1.10)$$

Here the Lagrangian multipliers, ε_i , can be seen as orbital energies and Koopmans' theorem states that ε_i is equal to the negative of the ionization energy, $-I_i$. The Fock operator can be expressed as

$$\hat{f}_i = -\frac{1}{2} \nabla_i^2 - \sum_A^M \frac{Z_A}{r_{iA}} + V_{\text{HF}}(i) \quad (1.11)$$

The first two terms are the kinetic energy of the electron in the i -th spin-orbital and the potential energy due to electron-nuclei attraction. The last term is the HF potential which allows the electron-electron repulsion to be accounted for in an average way by a simple one-electron operator instead of the complicated $1/r_{12}$ operator. The HF potential is expressed by

$$V_{\text{HF}}(\vec{x}_1) = \sum_j^N (\hat{J}_j(\vec{x}_1) - \hat{K}_j(\vec{x}_1)) \quad (1.12)$$

\hat{J} is the Coulomb operator and can be seen as the potential an electron in spin-orbital ϕ_i experiences due to the average charge distribution of an other electron in spin-orbital ϕ_j . \hat{K} , the exchange operator, does not have a simple physical interpretation (there is no classical analogue) but arises from the antisymmetry requirement.

To solve the HF equation, one has to use iterative methods. First, a set of basis functions, χ_y are chosen together with initially guessed coefficients, c_{yi} . These are used to calculate \hat{J} and \hat{K} which in turn are used to determine the Fock operator, \hat{f} . The Fock operator and the basis functions are then used to solve the determinant

$$\det(F_{zy} - \varepsilon_i S_{zy}) = 0 \quad (1.13)$$

where F_{zy} are the elements of the Fock-matrix given by

$$F_{zy} = \langle \chi_z | \hat{f}(1) | \chi_y \rangle \quad (1.14)$$

and S_{zy} is the overlap matrix given by

$$S_{zy} = \langle \chi_z | \chi_y \rangle \quad (1.15)$$

This will then give values for ε_i that can be input into the Roothaan-Hall equation

$$\sum_{y=1}^b c_{yi} (F_{zy} - \varepsilon_i S_{zy}) = 0 \quad (1.16)$$

to give new coefficients, c_{yi} . This cycle is repeated until neither ε_i or c_{yi} are improved compared to the previous cycle. The final coefficients, c_{yi} are used to obtain ϕ_i which can be used to calculate the total energy of the system. This method is called the self-consistent field (SCF) method.

1.3 History of DFT

DFT dates back to the 1920's when Thomas and Fermi first suggested that the ground state energy can be expressed in terms of electron density (see ref 1 and references therein). This has the advantage that the density is only dependent on three spatial variables, independent of the number of electrons in the system, whereas the wavefunction is dependent on three spatial variables and one spin variable for each electron in the system.

This Thomas-Fermi model is based on a uniform electron gas, similar to a metal, in which no exchange and correlation effects are taken into account.

$$E_{\text{TF}}[\rho(\vec{r})] = \frac{3}{10}(3\pi^2)^{2/3} \int \rho^{5/3}(\vec{r})d\vec{r} - Z \int \frac{\rho(\vec{r})}{r}d\vec{r} + \frac{1}{2} \int \int \frac{\rho(\vec{r}_1)\rho(\vec{r}_2)}{r_{12}}d\vec{r}_1d\vec{r}_2 \quad (1.17)$$

The kinetic energy is harshly approximated whereas the nucleus-electron and electron-electron repulsion are treated in a classical way. Thomas and Fermi could not prove that it was physically correct to describe the energy in terms of the electron density, but it seemed reasonable.

In 1964 Hohenberg and Kohn proved that the ground-state electronic energy can be determined completely by the electron density, ρ .

$$E[\rho] = T[\rho] + V_{\text{ee}}[\rho] + V_{\text{ne}}[\rho] \quad (1.18)$$

$E[\rho]$ is the total energy, $T[\rho]$ the electronic kinetic energy, $V_{\text{ee}}[\rho]$ the electron-electron

interaction energy and $V_{\text{ne}}[\rho]$ is the nucleus-electron interaction energy. The first theorem of Hohenberg and Kohn states that the external potential is a unique functional of the electron density and since the external potential determines the Hamiltonian, the ground state is a unique functional of the electron density. Their second theorem shows the validity of the variation principle for the energy, based on the electron density instead of the traditional wavefunction. These two theorems became the basis of modern DFT and Kohn later (1998) shared the Nobel Prize in chemistry for his contributions to DFT.

Kohn and Sham suggested a few years later that the total electronic energy of a system can be written as

$$E[\rho] = T_{\text{non-int}}[\rho] + J[\rho] + V_{\text{ne}}[\rho] + E_{\text{XC}}[\rho] \quad (1.19)$$

where the first term represents the kinetic energy of a fictitious system with non-interacting electrons that has the same density as the real interacting system, $J[\rho]$ accounts for the Coulombic interaction between electrons and V_{ne} is the potential energy due to nucleus-electron interactions. The first three terms of equation 1.19 can be calculated exactly whereas the last term, the Exchange-Correlation energy,

$$E_{\text{XC}}[\rho] = (T[\rho] - T_{\text{non-int}}[\rho]) + (E_{\text{ee}}[\rho] - J[\rho]) = T_{\text{c}}[\rho] + E_{\text{ncl}}[\rho] \quad (1.20)$$

can only be approximated. The non-classical potential energy, E_{ncl} , contains the self-interaction energy due to the difference between the hypothetical and true kinetic energy as well as the exchange and the correlation energy, i.e. the non-Coulombic part of the electron-electron interaction.

Just as for the Hartree-Fock approximation, the variational principle is applied and orbitals are determined through iteratively solving the Kohn-Sham one-electron

equation

$$\left(-\frac{\nabla^2}{2} + v_{\text{eff}}(\vec{r})\right)\phi_i = \varepsilon_i\phi_i \quad (1.21)$$

where the effective potential, v_{eff} , is given by:

$$v_{\text{eff}}(\vec{r}) = \int \frac{\rho(\vec{r}_2)}{r_{12}} d\vec{r}_2 + V_{\text{XC}}(\vec{r}_1) - \sum_A^M \frac{Z_A}{r_{1A}} \quad (1.22)$$

The effective potential is chosen such that the ground state density of interacting electrons, $\rho_0(\vec{r})$ is

$$\rho_0(\vec{r}) = \sum_i^N \sum_s |\phi_i(\vec{r}, s)|^2 \quad (1.23)$$

The first approximation in DFT comes from the potential due to the exchange-correlation energy, V_{XC} . If the exact form of E_{XC} and V_{XC} (its functional derivative) were known, then DFT would be in principle exact. This contrasts with HF theory in which the Slater determinant does not represent the real system but is just an approximation.

1.4 Exchange-Correlation Functional

Since the only term in the Kohn-Sham equation that can not be stated exactly is the exchange-correlation (XC) functional, this is where the emphasis on improvements must lie. Currently there is no structured way to improve these functionals as there is no clear way of knowing what works and what doesn't. However, there are some general features of successful functionals and they will be discussed here.

It is customary to treat the XC energy as two individual terms, the exchange term and the correlation term. The basis for the XC-functionals is to view them as representing a uniform electron gas. This means that the electrons move on a positive background and that the system in total is neutral. The number of electrons,

N , and the volume, V , are considered to approach infinity and the density, $N/V = \rho$, is constant everywhere. The constant density is far from true in most molecular systems where the electron density usually changes rapidly, but the uniform electron gas is the only system for which the exchange and correlation functionals can be solved exactly or at least to very high accuracy.

The simplest form of XC-functional is the local density approximation (LDA). The XC energy, $E_{\text{XC}}^{\text{LDA}}$ can be written as

$$E_{\text{XC}}^{\text{LDA}}[\rho] = \int \rho(\vec{r}) \varepsilon_{\text{XC}}(\rho(\vec{r})) d\vec{r} \quad (1.24)$$

$\varepsilon_{\text{XC}}(\rho(\vec{r}))$ is the XC energy per particle. If the spin is taken into account the XC-energy is instead given by

$$E_{\text{XC}}^{\text{LDA}}[\rho_{\alpha}, \rho_{\beta}] = \int \rho(\vec{r}) \varepsilon_{\text{XC}}(\rho_{\alpha}(\vec{r}), \rho_{\beta}(\vec{r})) d\vec{r} \quad (1.25)$$

The exchange part, ε_{X} , can be expressed by the Slater X_{α} exchange

$$\varepsilon_{\text{X}} = -\frac{9}{8} \frac{3^{1/3}}{\pi} \alpha \rho^{1/3} \quad (1.26)$$

where $\alpha=2/3$ corresponds to a uniform electron gas.²

The most widely used functional for the correlation part, ε_{C} , is the functional developed by Vosko, Wilk and Nusair, which employs an analytical interpolation formula.³ This functional, denoted VWN, is often combined with the Slater exchange functional, S, to give the SVWN XC-functional.

If the information about the density is not only obtained from the density at a particular point, but also from the changes in density through the gradient, $\nabla\rho(\vec{r})$, the electron gas is no longer homogenous and changes in the electron density can be taken into account. Functionals that include the gradient are called Generalised

Gradient Approximations, GGA, and their general expression can be written as

$$E_{XC}^{GGA}[\rho_\alpha, \rho_\beta] = \int f(\rho_\alpha, \rho_\beta, \nabla\rho_\alpha, \nabla\rho_\beta) \quad (1.27)$$

The number of GGA functionals available is extensive and new functionals are constantly appearing. However, some of the most commonly used functionals for the exchange part are Becke's 1988 functional (B88 or just B),⁴ and Perdew and Wang's 1986 or 1991 functional (PW86x, PW91x).^{5,6} For the correlation part, Perdew and Wang's PW91c functional is commonly used as is Lee, Yang and Parr's (LYP)⁷⁻⁹ and Perdew's correlation functionals.¹⁰

The obvious step up from GGA would be to include another variable in the XC-functionals. This has been done in the so called meta-GGA functionals. These make use not only of the density and its gradient as in GGA, but also of a third factor which often is the laplacian, i.e. the kinetic energy density.

$$E_{XC}^{\text{meta-GGA}}[\rho_\alpha, \rho_\beta] = \int f(\rho_\alpha, \rho_\beta, \nabla\rho_\alpha, \nabla\rho_\beta, \gamma_\alpha, \gamma_\beta) \quad (1.28)$$

These functionals have the computational setback that it is difficult to optimise the geometry due to the XC-potential often being non-local and orbital-dependent. Instead meta-GGA often acts as a post-GGA method and uses the orbitals determined at the GGA level. This limits the use of meta-GGA functionals and they have not yet proved popular among users.

Another relatively new approach to the XC-functionals are the so-called hybrid functionals. These make use of a certain amount of the exact exchange energy that can be calculated from the Slater determinant of the HF approach, and apply approximate functionals for the correlation energy and the remaining exchange energy. This method has proven very successful and has in many ways taken over from the

traditional XC-functionals. One of the most commonly used hybrid functionals is the B3LYP functional which uses the Becke88 exchange and the LYP correlation as the approximate functionals.¹¹

1.5 Basis Sets

To describe molecular orbitals all *ab initio* and density functional methods in practice rely on the selection of appropriate basis sets. The MOs are thus unknown functions expanded in a set of known functions (the basis set). A basis set is complete (has the best single determinant wavefunction that can be obtained) if an infinite number of functions are used, as the unknown MO function can then be expanded exactly from an infinite set of known functions. This leads to a trade-off between calculation time and accuracy. Since a complete basis set is impossible in practice, there will always be an absolute error in the calculated result. Therefore the primary goal is to make the error as small and consistent as possible. The number of functions needed has to be selected for the user's requirements, but because of the absolute errors it is meaningless to compare two molecules calculated with different basis sets.

The basis functions mainly used in the presented work are Slater Type Orbitals (STO). These are a collection of atomic orbitals that can be written as

$$\chi_{\zeta,n,l,m}(r, \theta, \varphi) = NY_{l,m}(\theta, \varphi)r^{n-1}e^{-\zeta r} \quad (1.29)$$

where $Y_{l,m}$ are the spherical harmonic functions where the subscript indicates the orbital angular momentum and magnetic quantum number dependence. N is the normalisation constant, ζ is the orbital exponent and r, θ and φ represent the polar coordinates.

Another commonly used basis set type in electronic structure calculations is the Gaussian Type Orbital (GTO).

$$\chi_{\zeta,n,l,m}(r, \theta, \varphi) = NY_{l,m}(\theta, \varphi)r^{2n-2-l}e^{-\zeta r^2} \quad (1.30)$$

GTOs are generally less accurate than STOs, which better represent ‘real’ atomic functions, and approximately three times as many GTOs compared to STOs are required to reach the same level of accuracy. However, integrals involving $e^{-\zeta r^2}$ dependence (GTOs) are easier to compute than those involving $e^{-\zeta r}$ (STOs) because they are suited for analytical integration and hence GTOs dominate most *ab initio* codes. The computational implementation of DFT generally requires numerical integration for the XC potential and this makes the STOs a more appropriate choice than GTOs. The ADF code, used extensively in this work, uses STOs as its basis sets.

Basis sets can have different size and complexities. The larger the number of functions the more complex the basis set. The minimum number of functions to describe the electrons of a neutral atom determines the contents of the minimum basis set. For the first row in the periodic table this means two s-functions (1s, 2s) and one set of p-functions (2p_x, 2p_y and 2p_z). The first step to improve the basis set is to double the number of functions leading to the first row element being described by four s-functions (1s, 1s', 2s and 2s') and two set of p-functions (2p and 2p'). This allows a better description of the electron distribution, especially when the electron distribution is asymmetric, e.g. in a bond. This double basis set is called double zeta (DZ) where zeta (ζ) comes from the exponent of the STO basis function. Usually the core electrons are kept as simple as possible and only the valence electrons are given the double basis set (split valence basis). The next levels are called triple zeta

(TZ), quadruple zeta (QZ) and so on.

Polarisation functions, i.e. higher angular momentum functions, can also be added. p-orbitals can be used to polarise atoms with valence s-orbitals, d-orbitals for p-orbitals etc. The higher angular momentum functions make it possible to accurately describe fluctuations in the electron distribution around an atom which is essential in methods that include electron correlation. One single polarisation (P), added to a DZ basis set, forms a double zeta with polarisation (DZP). The next level is called double polarisation (2P) and so on.

Sometime these basis functions are not accurate enough and diffuse functions have to be used. Diffuse functions are basis functions with a small exponent and are needed when it is of importance to describe the valence electrons accurately, i.e. calculations of anions or excited states or polarisability-dependent properties.

1.6 Calculating Excitation Energies using Time-Dependent Density Functional Theory

The calculation of excitation energies with DFT is more complex than the calculation of static ground state properties. The Kohn-Sham eigenvalues do not have any real physical meaning and thus Koopmans' theorem does not exist in DFT. One method to calculate the excitation energies from the ground state density is the Δ SCF method but this is both time consuming and not very accurate. A relatively recent development is the time-dependent DFT (TD-DFT), which allows the user to calculate a wide range of frequency dependent molecular properties such as van der Waals dispersion coefficients, frequency-dependent polarisabilities and hyperpolarisabilities, optical activities and Raman scattering intensities.¹² One of

the most popular uses of TD-DFT is to calculate excitation energies and this will be described here.^{13,14}

The range of molecules that can be used in TD-DFT calculations is comparable to those that can be calculated in the ground state SCF calculations, and linear scaling techniques have recently been developed to allow even larger molecules to be calculated using TD-DFT.

The basic equation behind time-dependent methods is the time-dependent Schrödinger equation which is given by

$$\hat{H}(\vec{r}, t)\Psi(\vec{r}, t) = i\frac{\partial}{\partial t}\Psi(\vec{r}, t) \quad (1.31)$$

Extending this to DFT, the Kohn-Sham time-dependent equation is

$$\left[-\frac{1}{2}\nabla_i^2 + v_{\text{eff}}(\vec{r}, t)\right]\phi_i(\vec{r}, t) = i\frac{\partial}{\partial t}\phi_i(\vec{r}, t) \quad (1.32)$$

where the effective potential, $v_{\text{eff}}(\vec{r}, t)$ is given by

$$v_{\text{eff}}(\vec{r}, t) = v_{\text{ext}}(\vec{r}, t) + \int \frac{\rho(\vec{r}_2, t)}{r_{12}} d\vec{r}_2 + v_{\text{XC}}(\vec{r}, t) \quad (1.33)$$

$v_{\text{ext}}(\vec{r}, t)$ is the external potential, that is, the Coulombic field and, if present, any external field. $v_{\text{XC}}(\vec{r}, t)$ is the time-dependent XC potential. TD-DFT is, just as time-independent DFT, built on the direct connection between the density and the external potential. This was proved by Runge and Gross whose theorem states that the time-dependent density uniquely determines the external potential which in turn uniquely determines the time-dependent wave function.¹⁵ In contrast to the time-dependent HF equation which only takes into account the exchange effects, TD-DFT also includes all correlation effects and thus calculates excitation energies that are, in theory, exact.

The excitation energy from the i -th orbital, ω_i , can be obtained from an eigenvalue equation

$$\Omega F_i = \omega_i^2 F_i \quad (1.34)$$

where F_i is the single determinant of KS orbitals from which the oscillator strengths can be obtained. To begin, the determinant F_i has to be guessed. Ω is given by

$$\Omega_{ia\sigma,jb\tau} = \delta_{\sigma\tau}\delta_{ij}\delta_{ab}(\varepsilon_{a\sigma} - \varepsilon_{i\sigma})^2 + 2\sqrt{(\varepsilon_{a\sigma} - \varepsilon_{i\sigma}K_{ia\sigma,jb\tau})\sqrt{(\varepsilon_{b\tau} - \varepsilon_{j\tau})}} \quad (1.35)$$

where a and b refer to unoccupied orbitals whereas i and j refer to occupied orbitals. σ and τ refer to the spin of the electron. δ_{ij} , δ_{ab} and $\delta_{\sigma\tau}$ are the Kronecker delta that are 1 if $i = j$, $a = b$, $\sigma = \tau$ and 0 otherwise. If K is set to zero, the excitation energies are the difference between eigenvalues of occupied and unoccupied orbitals. This has proven to be a good approximation and a good initial guess. K is a matrix that contains and can be divided into the Coulomb part and the XC part.

$$K_{ia\sigma,jb\tau}^{\text{Coul}} = \int \int \left[\phi_{i\sigma}(\vec{r}_1)\phi_{a\sigma}(\vec{r}_1) \times \frac{1}{r_{12}}\phi_{j\tau}(\vec{r}_2)\phi_{b\tau}(\vec{r}_2) \right] d\vec{r}_1 d\vec{r}_2 \quad (1.36)$$

$$K_{ia\sigma,jb\tau}^{\text{XC}}(\omega) = \int \int [\phi_{i\sigma}(\vec{r}_1)\phi_{a\sigma}(\vec{r}_1) \times f_{\text{XC}}^{\sigma\tau}(\vec{r}_1, \vec{r}_2, \omega)\phi_{j\tau}(\vec{r}_2)\phi_{b\tau}(\vec{r}_2)] d\vec{r}_1 d\vec{r}_2 \quad (1.37)$$

f_{XC} is the XC kernel which determines the first-order change in the time-dependent XC potential due to the applied electric perturbation. In equation 1.37 ω indicates the functional's frequency dependence and the exchange-correlation part of K is therefore time-dependent.

1.7 Relativistic Effects

When a particle of mass, m_0 , moves with a velocity, ν , the actual relativistic mass, m , is given by the formula:

$$m = \frac{m_0}{\sqrt{1 - \frac{\nu^2}{c^2}}} \quad (1.38)$$

From this, it can be seen that a slowly moving particle possesses an actual mass almost equal to the rest mass whereas a quickly moving particle will have significantly increased mass.

In atomic units, the velocity of an electron in the 1s shell of an atom is approximately equal to the atomic number, Z , which makes it clear that the heavier the atom is, the greater the relativistic mass increase will be of the electron. Therefore relativity needs to be included in calculations with heavy atoms to give accurate results.

The Bohr radius is dependent on the mass through $1/m$, so when including relativistic effects the radius decreases as the atomic number increases. The result of this is that the 1s-orbital is contracted. The outer s-orbitals are also somewhat contracted which has traditionally been explained as arising from the orthogonality constraint on the orbitals. However, it is now believed that the contraction of the higher valence orbitals is due to mixing in of higher energy orbitals.¹⁶ A more compact s-orbital results in a more effective screening of the nuclear charge which in turn affects the orbitals with higher angular momentum. p-orbitals are mainly unaffected but d- and f-orbitals become radially more extended.

To include relativistic effects, the particle has to be described using four coordinates, three in space and one in time. The time-dependent Schrödinger equation contains second-order partial derivatives with respect to x , y and z but first-order with respect to t which is not relativistically correct. To solve this problem Dirac produced an equation which treats all four space-time components as first-order.

$$\left[-i\hbar \left(\alpha_x \frac{\partial}{\partial x} + \alpha_y \frac{\partial}{\partial y} + \alpha_z \frac{\partial}{\partial z} \right) + \beta mc^2 + V(x, y, z) \right] \Psi = i\hbar \frac{\partial \Psi}{\partial t} \quad (1.39)$$

α_x , α_y , α_z and β are 4×4 -matrices. This leads to the requirement that Ψ has to

be a four-component column vector and thus there are in principle four solutions to equation 1.39; two giving a positive energy with a solution corresponding to a particle of mass m_e and charge $+e$, and two giving a negative energy with a solution corresponding to the same mass as the other two but with charge $-e$. The two negative energy solutions correspond to the two possible spin states of an electron. The positive energy states correspond to positronic wave functions, hence Dirac predicted the existence of the positron, which was discovered a few years later (1932) by Carl D. Anderson.

To include the entire four component Dirac equation in a study of molecules of a reasonable size, is practically impossible. It is more common to derive atomic basis sets using the Dirac equation, and then on a molecular level to use for example the quasi-relativistic Pauli formalism¹⁷ or the zeroth order regular approximation (ZORA).¹⁸

The Pauli formalism is based on the approximation that $E - V \ll 2mc^2$. However, at a certain distance close to the nucleus, this approximation does not hold due to the electrostatic energy, V , becoming more negative.

The ZORA approach, which usually give more accurate results than the Pauli formalism, expands the energy in $E/(2mc^2 - V)$ and makes use of the approximation $E \ll 2mc^2 - V$. This holds even close to the nucleus.

As noted above, the Dirac equation directly includes the electron spin, thus allowing the inclusion of spin-orbit coupling (SOC) in relativistic calculations. SOC stems from the interaction of an electron's magnetic moment due to the spin angular momentum, with the magnetic field that is generated by its own orbital motion, the orbital angular momentum l . This interaction is dependent on the total angular momentum j which can take the values $j = l \pm \frac{1}{2}$. The spin-orbit coupling increases

as the nuclear charge increases and decreases as l increases. When the spin-orbit coupling is weak the Russell-Saunders coupling scheme can be used but fails for heavier molecules where the coupling is greater. For those molecules the jj -coupling is more appropriate.

1.8 The Amsterdam Density Functional Code

The Amsterdam Density Functional (ADF) package is a Fortran program based on the Kohn-Sham approach to DFT, and offers a wide range of functionalities such as geometry optimisation, frequencies, excitation energies etc.¹⁹⁻²⁴ It is developed by the Theoretical Chemistry groups of the Vrije University in Amsterdam and Groningen University, the Netherlands, and University of Calgary, Canada.

ADF uses STOs as basis functions to generate the atoms. The fragment approach to build up a molecule in ADF will be described in detail in section 1.8.2. ADF supports many XC-functionals (LDA, GGA and meta-GGA) but since it is a pure DFT program, no hybrid-DFT functionals are available.

Relativistic effects are offered either through the Pauli formalism or the ZORA approach (see section 1.7) and solvent effects can be taken into account through the COSMO algorithm that has been implemented via GEPOL93 (see section 1.8.1).²⁵

1.8.1 The Conductor-like Screening Model of Solvation

The computational description of molecules in a vacuum or in the gas-phase that has been developed over the past several decades now allows us to carry out calculations and make predictions with high accuracy. However, the techniques for computationally describing systems in solution are not as well developed. Even so,

it is greatly desirable to be able to include solvent effects. Many physical properties alter in a solvent system and it is therefore important to be able to calculate these with just as high an accuracy as for systems in the gas phase.

To accurately describe the solute molecule in a solvent on the molecular scale is difficult, mainly because of the many solvent molecules around the solute molecule that not only interact with the solute but also with each other. There are a number of different approaches to describe the solvent/solute system. One such approach uses a dielectric continuum model, with a dielectric medium as solvent with permittivity ϵ and with the solute embedded in a cavity. A charge distribution is created at the interface between the solvent and the solute, where the solvent has the opposite sign of the charge distribution in the solute. One big problem is how to describe the interactions at the interface. Klamt has developed an algorithm known as the conductor-like screening model (COSMO) of solvation.²⁶⁻²⁸ It aims not only to describe ellipsoidal or spherical surfaces but any arbitrary surface. To do this the surface is divided into a number of segments. Each segment possesses a center r_μ , a surface area S_μ and a charge q_μ . The solvation energy, E^S , is then given by

$$E^S = \sum_A \sum_\mu \frac{Z_A q_\mu}{|R_A - r_\mu|} + \frac{1}{2} \sum_{v \neq \mu} \sum_\mu \frac{q_v q_\mu}{|r_\mu - r_v|} + \sum_\mu 1.07 \sqrt{\frac{4\pi}{S_\mu}} q_\mu^2 + \sum_\mu \int_V q_\mu V_\mu(r) \rho(r) dr \quad (1.40)$$

where Z_A is the nuclear charge at R_A . The solvation energy thus contains contributions from the nucleus-surface and the surface-surface electrostatic interactions (given by the first and second term respectively) as well as the electrostatic interactions within each segment (given by the third term). The final term represents the interaction between the electron density, $\rho(r)$, and a surface in which the surface charge has been distributed with a potential $q_\mu V_\mu$.

ADF offers four different approaches to construct the surface in COSMO; WSURF, ASURF, ESURF and KLAMT.²⁹ WSURF is the van der Waals surface (see figure 1.1(a)), ASURF is the accessible surface, i.e. the surface generated by the centre of the solvent molecules rolling on the van der Waals surface (see figure 1.1(b)) and ESURF is the van der Waals surface that is accessible by the solvent molecules with cusps in the intersecting region (see figure 1.1(c)). KLAMT can be seen as first creating the ASURF surface and then subtracting the radius of the solvent.

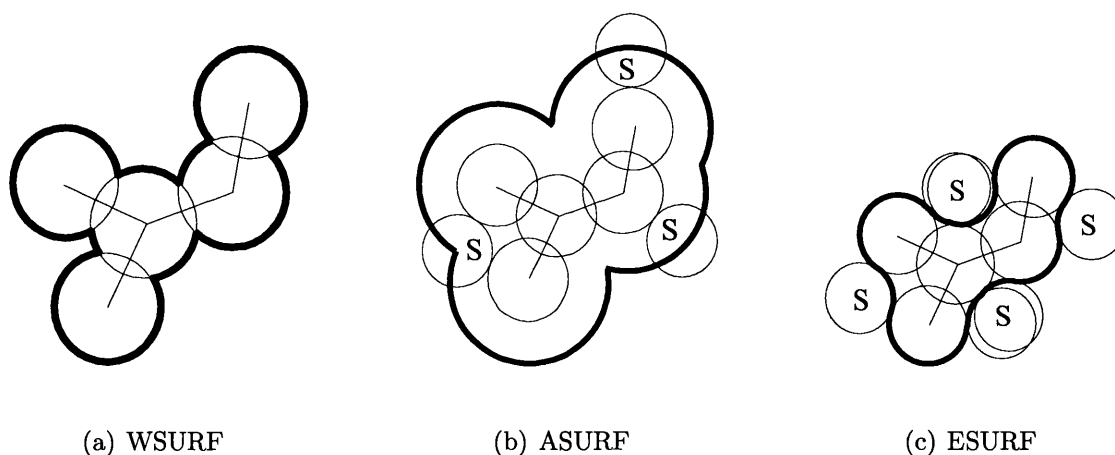


Figure 1.1: COSMO surfaces

The main concern in a calculation using the COSMO approach is to describe the surface interactions accurately which makes it important to use the correct solvent radius and van der Waals radius of the solute. Since the solvent is seen as a sphere in COSMO but in reality the shape of a molecule is often non-spherical, it can be difficult to choose the right radius. In this study the central carbon atom of the solvent (usually CH_2Cl_2) was chosen as the centre of the sphere, and the solvent radius was calculated as the distance from the central atom to the atom furthest away, plus that atom's van der Waals radius. Alternatively, the centre of mass, m can also be used as the centre of the sphere. The coordinates of the centre can then

be calculated using:

$$\begin{aligned}
 x &= \frac{m_1}{m} \times x_1 + \frac{m_2}{m} \times x_2 \dots + \frac{m_i}{m} \times x_i \\
 y &= \frac{m_1}{m} \times y_1 + \frac{m_2}{m} \times y_2 \dots + \frac{m_i}{m} \times y_i \\
 z &= \frac{m_1}{m} \times z_1 + \frac{m_2}{m} \times z_2 \dots + \frac{m_i}{m} \times z_i
 \end{aligned}
 \tag{1.41}$$

1.8.2 Ziegler-Rauk Energy Decomposition Scheme

ADF defines the molecular bonding energy as the energy difference between the molecular fragments in their final position and at infinite separation. The composition of a molecule in ADF starts with two unperturbed fragments or atoms, with electron density ρ_A and ρ_B , that are positioned in their final molecular position to give a superposition of fragment densities, $\rho_A + \rho_B$. The interaction energy between these fragments is the traditional electrostatic energy, E^{elstat} . At long interatomic distances this energy approaches zero. As the fragments approach each other the electrostatic energy becomes more negative. This is due to the stabilising nucleus-electron attraction that outweighs the electron-electron repulsion. According to general electrostatics and Gauss' law, the electron-electron repulsion becomes smaller as the electron clouds begin to interpenetrate. Thus, the bigger the orbital overlap, the smaller the electron-electron interaction. At very short distances, much closer than the equilibrium bond distance, the nucleus-nucleus repulsion causes a significant destabilisation of the electrostatic energy.

The next step is to alter the superposition of electron densities by making sure that the antisymmetry constraint (Pauli principle) is followed. The antisymmetry constraint brings about a reduction in the electron density in the overlap region and thus a reduction (destabilisation) in energy. This energy is therefore called the Pauli

repulsion energy, E^{Pauli} . It should be noted that the bigger the orbital overlap is, the bigger the Pauli repulsion will be due to the larger area in which the electron density is reduced.

The last step allows the electronic wavefunction to relax to self-consistency. This is done by allowing the virtual orbitals to mix with the occupied orbitals. This has the opposite effect on the electron density in the overlap region to the antisymmetrisation in the second step and thus has a stabilising effect on the energy. This energy is called the orbital interaction energy, E^{oi} .

ADF allows for a breakdown of the bond energy into each of these three energies³⁰ and they are computed using the transition state procedure developed by Ziegler and Rauk.^{31,32}

1.9 Other Computational Methods

A few other computational methods besides DFT have been employed in this thesis work; Hartree-Fock (HF), Møller-Plesset second-order perturbation theory (MP2) and coupled cluster with single, double and triple excitations (CCSD(T))(for further information see ref 17).

The HF method has been described in brief in section 1.2. The major disadvantage of this method is the exclusion of correlation effects that, for instance, often results in too low bond energies. The aim of all of the post-HF methods mentioned is to begin with the HF Slater determinant and to account for electron correlation from this.

The MP2 method uses the HF wave function as the unperturbed wavefunction and then adds a perturbation term to second order to include the correlation effects

that are non-existent in HF. This method usually gives good results in geometry optimisations and bond energy calculations but a relatively large basis set is required to get good results and the correlation energy is somewhat overestimated.

The CCSD(T) method has proven very accurate, especially for systems which can be well-represented by a single Slater determinant (e.g. molecules with large HOMO/LUMO gaps). However, the computational cost is significantly higher than in DFT. All single and double excitation determinants are calculated whereas the contributions from the triple excited state are calculated from the formula given by MP4 and added to the energy. To include all triple excitation determinants are too computationally demanding and is only applicable on very small systems. The double excitations are most important to include since they account for most of the correlation effects.

1.10 Overview of Thesis

As already mentioned, three projects will be presented in this thesis. First, however, the computational and experimental details will be described in chapter 2. Following that the first project, a study of the electronic transition energies in 1,4-diazabut-1,3-diene compounds and their palladium complexes will be presented (chapter 3). First an introduction to the chemistry of 1,4-diazabut-1,3-dienes and their metal complexes will be given, followed by a discussion of the results obtained from this study. The second project, a bond energy analysis of the X_2 bond ($X=F, Cl, Br, I$), will then be presented (chapter 4) in the same manner as the previous chapter; first an introduction and then a discussion of the results obtained in this study. Finally, the last project, a study of the potential energy surface of the $ClO+HO_2$ reaction,

will be presented (chapter 5).

Chapter 2

General computational and experimental details

2.1 Computational details

All calculations have been carried out on Compaq ES40 and Digital Personal Workstation 433au computers using the Amsterdam Density Functional (ADF) program versions 2.3, 1999, 2000 and 2002 unless otherwise stated.¹⁹⁻²⁴

Molecular orbital plots were generated using the program MOLDEN, written by G. Schaftenaar of the CAOS/CAMM Centre, Nijmegen, The Netherlands. The same 'space' value, 0.05, has been used for all plots. The ADF binary output files (TAPE21) were converted to MOLDEN format using the program ADFrom99 written by F. Mariotti of the University of Florence.³³

Slater-type orbital basis sets were employed and their quality was varied as mentioned in each relevant section. If nothing else is stated, the basis sets were uncontracted, valence only with the frozen core approximation employed; carbon (1s), nitrogen (1s), silicon (2p), chlorine (2p) and palladium (3d). Scalar relativistic

corrections were included via the ZORA method where stated. No spin-orbit coupling has been taken into account unless otherwise stated. The choice of exchange-correlation functional is varied as mentioned in each relevant section. The ADF numerical integration parameters was set to 4 and the energy gradient convergence criterion was set to 1×10^{-3} au \AA^{-1} in all geometry optimisations unless otherwise stated. Excitation energies were computed using the time-dependent methods implemented in ADF.¹² Solvent effects were included, where stated, using the COSMO of solvation.²⁶⁻²⁸

2.2 Experimental details

Although the majority of my work has been computational, I have also done a bit of experimental work. All reactions were carried out in pre-dried glassware under nitrogen atmosphere. The reagents were purchased from commercial suppliers and used without further purification. Solvents were purified and dried according to customary procedures.³⁴ Tlc was carried out using silica 60 F₂₅₄ plates (Merck) and the spots were visualised using a UV-lamp.

N,N'-bis(phenyl)-1,6-bis(triisopropylsilyl)-hexa-1,5-diyne-3,4-diimine palladium dichloride (compound 3, chapter 3) was synthesised as described in appendix A. The melting point was determined on a Reichert hotstage and is uncorrected. ¹H and ¹³C NMR spectra were recorded on Bruker AMX400 spectrometer in CDCl₃ with residual chloroform (7.24 ppm ¹H, 77.00 ppm ¹³C) as an internal reference. The IR-spectrum was recorded on a Shimadzu 8700 FT-IR instrument as a KBr disc. The UV-spectrum was recorded on a Perkin Elmer Lambda 40 spectrometer. The extinction coefficient is given in units of M¹cm⁻¹. The mass spectrum was recorded

on a VG ZAB SE machine.

N,N'-bis(4'-dimethylaminophenyl)-1,6-bis(triisopropylsilyl)-hexa-1,5-diyne-3,4-diimine palladium chloride (compound 7, chapter 3) was synthesised according to the literature procedures³⁵ in order to measure the UV-spectra in different solvents (see section 3.5.9). UV-spectra were recorded as mentioned above.

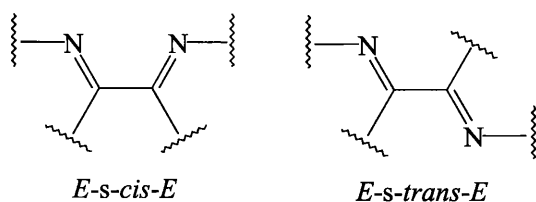
Chapter 3

Electronic Transition Energies in 1,4-diazabuta-1,3-diene Compounds and their Complexes with Palladium

3.1 Introduction

1,4-diazabuta-1,3-diene (DAD) compounds have many uses, mainly due to the ease with which their steric and electronic properties can be tuned by changing the substituents. Synthetically they have applications as building blocks in constructing 4-, 5- and 6-membered heterocycles and in olefin polymerisation.³⁶

Most DAD molecules adopt a planar *s-trans* conformation with both C=N bonds in an *E* configuration (*E-s-trans-E*) but the free rotation around the central C-C bond also makes it possible for DAD to adopt a *E-s-cis-E* or gauche conformation. The *trans* conformation is usually the favoured conformation because it alleviates the interactions between the nitrogen lone pairs as well as the steric interactions



between the substituents in the 2 and 3 positions. Bulky substituents in the 2 and 3 positions cause steric interactions that give rise to the less symmetrical gauche conformation. It has been found that most DADs have a rotational barrier, when going from the *s-trans* to the *s-cis*, ranging from 20 to 28 kJ/mol.³⁷ This is important in their coordination chemistry as the *s-cis* conformation is needed if the DAD is to act as a chelate.

The DAD has excellent coordination behaviour and can coordinate to a metal either by its nitrogen lone pairs or by the π -C=N.^{37,38} It can therefore act as a 2-, 4-, 6- or 8-electron donor in chelating, terminal or bridging arrangements. In its *s-trans* conformation it can use only one lone pair at a time to donate two electrons to a metal in the unidentate coordination mode. By rotating around the central C-C bond to the *s-cis* conformation, it can use both lone pairs (four electrons) and work as a chelate. It may also act as 6- or 8-electron donor by using one or two C=N bonds to donate electrons to a second metal but there are few examples of these and they are not very stable.

The steric and electronic properties of DAD molecules can be tuned by varying the substituents on the nitrogens or on the central carbons, or by complexation with a transition metal. Substitution at the 2 and 3 position has been somewhat restricted (to H, Me or fused aryl). However, recently Faust *et al.* have found that attaching acetylene substituents in these positions not only opens the door to a wider choice of substituents but also results in a bathochromic shift of the longest wavelength

absorption in the UV/Vis spectra.^{39,40} They developed a synthetic route, which involves the condensation of an acetylenic diketone and two amines, that is both straightforward and gives satisfactory yields.

In 1999 Faust *et al.* also carried out semi-empirical calculations on a number of acetylenic DADs (see figure 3.1) using the PM3 parameter set as implemented in Mac-Spartan.⁴⁰ They found that the introduction of the acetylenic moiety lowers the energy of the LUMO, making the acetylenic DADs easier to reduce than the non-acetylenic DADs. The two molecular halves in the 4-NH₂/4-NO₂ substituted molecule were found to have the LUMO centered on the NO₂ half and the HOMO centered on the NH₂ half, indicating these DADs have two halves that are covalently bound but largely decoupled electronically. This was supported by electrochemical results and is explored further in this chapter.

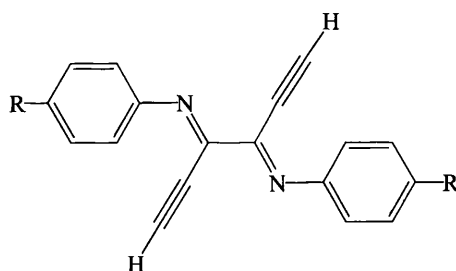


Figure 3.1: General structure of the N,N'-phenyl-2,3-dialkynyl-1,4-diazabuta-1,3-dienes.

The interest in these 2,3-dialkynyl-1,4-diazabuta-1,3-diene molecules and their metal complexes (see figure 3.2) stems from their potential as photosensitisers in the near infrared (NIR) region. Chromophores that absorb light in this region of the electromagnetic spectrum can be used, for instance, in optical recording systems, as photoreceptors in laser printers or as fluorescent dyes in DNA-sequencing.^{41,42} In medicine the natural chromophores in human tissue and in blood are relatively

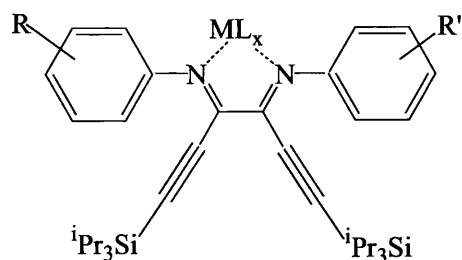


Figure 3.2: General structure of the N,N'-phenyl-2,3-dialkynyl-1,4-diazabuta-1,3-diene metal complexes.

Table 3.1: Comparison of the effect of different aryl substituents and metals on the longest wavelength absorption in DCM.

R	R'	ML _x	λ[nm](ε[M ⁻¹ cm ⁻¹])
H	H	PdCl ₂	425(12700) ^a
4-NO ₂	4-NO ₂	PdCl ₂	436(12900) ^b
4-NMe ₂	H	PdCl ₂	744(11200) ^b
4-NMe ₂	4-NO ₂	PdCl ₂	777(15600) ^b
4-NMe ₂	4-NMe ₂	PdCl ₂	781(15600) ^b
4-NMe ₂	4-NMe ₂	CuBr	598(22700) ^b
4-NMe ₂	4-NMe ₂	NiBr ₂	684(32500) ^b

^a see appendix A, ^b see ref 35

transparent in the NIR region and thereby allow deeper light penetration which is very useful in, for example, photodynamic therapy (PDT).⁴³

As can be seen in table 3.1 the presence of an electron-donating dimethylamino group in the 4-position of one or both the phenyl moieties results in a bathochromic shift of the longest wavelength absorption compared to the unsubstituted or the 4-NO₂ substituted complexes. Altering the metal-halogen unit also has an effect; PdCl₂ gives a red shift compared to NiBr₂ and CuBr but this is at the expense of a reduced extinction coefficient.

In order to gain further insight into the electronic absorption spectra of DADs and their transition metal complexes, TD-DFT has been employed. The aim was to

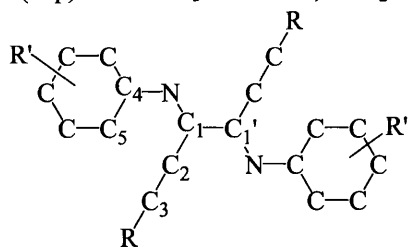
gain knowledge of the nature of the electronic transitions and to aid the design of molecules with the correct photophysical properties for PDT, specifically molecules with a strong NIR absorption. The effect of *para* substitution as well as the effect of complexation with PdCl₂ on the electronic transitions has been investigated and the computational results are compared with experimental data.

First a number of DADs were studied to establish a good model chemistry and to gain an insight into the effect of the *para* substituent on the electronic transitions. Then the same DADs were studied as part of PdCl₂ complexes to further establish the effect of the *para* substituent and the effect of the complexation on the electronic transitions. Finally the effect of the solvent on the electronic transitions was investigated. Part of this work has been published (see reference 44).

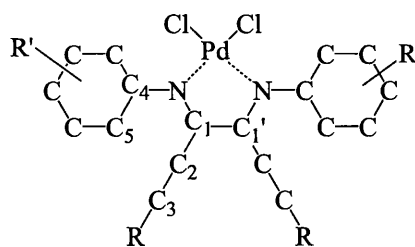
3.2 Determining the Most Suitable Computational Parameters

Several different DAD molecules that have been chosen as computational targets for the present study are represented in figure 3.3 together with the experimentally studied systems. The specific acetylenic (indicated by R) and aryl (indicated by R') substituents are shown, as is the numbering system that will be adopted.

Compound	R	R'	Compound	R	R'
1 (exp, calc)	ⁱ Pr ₃ Si	H	3 (exp)	ⁱ Pr ₃ Si	H
2 (calc)	H	H	4 (calc)	H	H
5 (exp)	ⁱ Pr ₃ Si	4-Me ₂ N	7 (exp)	ⁱ Pr ₃ Si	4-Me ₂ N
6 (calc)	H	4-Me ₂ N	8 (calc)	H	4-Me ₂ N
9 (exp)	ⁱ Pr ₃ Si	4-NO ₂	11 (exp)	ⁱ Pr ₃ Si	4-NO ₂
10 (calc)	H	4-NO ₂	12 (calc)	H	4-NO ₂
13 (exp)	ⁱ Pr ₃ Si	4-NO ₂ , 4-Me ₂ N	15 (exp)	ⁱ Pr ₃ Si	4-NO ₂ , 4-Me ₂ N
14 (calc)	H	4-NO ₂ , 4-Me ₂ N	16 (calc)	H	4-NO ₂ , 4-Me ₂ N
17 (exp)	C ₆ H ₅	H			
18 (exp)	ⁱ Pr ₃ Si	3,5-Me ₂			



(a) DAD



(b) DAD complexes

Figure 3.3: Schematic representation of the DAD ligands and corresponding palladium complexes discussed in this study.

These molecules are large by the standards of quantum chemistry and it was therefore important to establish a computational model, i.e. a set of computational parameters, that reproduce experimental results and that are at the same time computationally feasible. Planar **2** in the *E-s-trans-E* orientation was chosen as a

system on which to establish the computational model. The *E-s-trans-E* orientation was chosen as this arrangement is found crystallographically for **17** and **18**,⁴⁰ and although experimentally the aryl rings are found to be substantially rotated out of the plane, the planar structure was adopted to ensure highest possible symmetry (C_{2h}). This ensures efficient computation in the trial calculations.

3.2.1 Basis Set

The effect of basis set was investigated in planar **2** by varying the basis set from single zeta (SZ) to double zeta plus a single polarization function (DZP) and finally to triple zeta plus two polarization functions (TZ2P). The geometry was fully optimised under C_{2h} symmetry constraints at the LDA (VWN) level³ in each case and the optimised geometry was then used to calculate singlet-singlet transition energies and the corresponding oscillator strengths. The results are presented in table 3.2. It can be seen that the four lowest energy transitions do not alter in character with expanding basis set whereas the transitions below 200 nm do experience a change in MO character. Even if it might seem like some of the high energy transitions in table 3.2 are identical in character, the character given is only the most significant contribution and many others with almost the same percentage contributions are also responsible for that specific transition.

When going from the SZ basis set to the DZP basis set, a significant bathochromic shift is observed for transitions above 200 nm. Expanding the basis set further, to TZ2P, shows little improvement and only small bathochromic shifts of a few nm are observed. Thus it is concluded that the DZP basis set is adequate for further studies.

Table 3.2: Calculated wavelengths (nm), transition energies (eV) and oscillator strengths and orbital characteristics of the bands in the UV/Vis spectra of planar **2** with different basis sets using the LDA.

SZ		DZP		TZ2P		Principal character of initial and final MOs
Wavelength (Energy)	Osc. St.	Wavelength (Energy)	Osc. St.	Wavelength (Energy)	Osc. St.	
356(3.48)	0.84	404(3.07)	0.91	409(3.03)	0.91	DAD π_2 / aryl e_1 \rightarrow DAD π_3 / aryl e_1 (92% SZ; 95% DZP; 95% TZ2P)
240(5.16)	0.16	271(4.57)	0.17	274(4.52)	0.16	DAD π_1 / aryl e_1 / acetylene π \rightarrow DAD π_4 / aryl e_1 / acetylene π^* (78% SZ; 75% DZP; 72% TZ2P)
223(5.56)	0.18	235(5.28)	0.12	237(5.23)	0.15	DAD π_2 / aryl e_1 / acetylene π \rightarrow DAD π_3 / aryl e_1 (64% SZ; 70% DZP; 49% TZ2P)
187(6.62)	0.13	195(6.37)	0.20	201(6.16)	0.18	DAD N p \rightarrow acetylene π^* (74% SZ; 81% DZP; 55% TZ2P)
				192(6.45)	0.11	C ₁ -C _{1'} π / acetylene π \rightarrow acetylene π^* (53%)
				184(6.73)	0.50	aryl e_1 / DAD N p_π / acetylene π \rightarrow aryl e_2 / DAD N p_π / acetylene π^* (29%)
				182(6.82)	0.31	DAD N p / acetylene π \rightarrow aryl e_1 (78%)
				181(6.86)	0.23	DAD π_2 / aryl e_1 \rightarrow DAD π_3 / aryl e_1 (25%)
				181(6.86)	0.19	DAD π_2 / aryl e_1 \rightarrow DAD π_3 / acetylene π^* (22%)
				178(6.96)	0.38	DAD π_2 / aryl e_1 \rightarrow DAD π_3 / acetylene π^* (39%)
				177(7.01)	0.27	DAD π_2 / aryl e_1 / acetylene π \rightarrow aryl e_2 (23%)
		174(7.14)	0.33			DAD π_2 / aryl e_1 \rightarrow DAD π_3 / acetylene π^* (19%)
156(7.96)	0.40					DAD π_2 / aryl e_1 \rightarrow DAD π_3 / acetylene π^* (33%)
148(8.39)	0.16					DAD π_2 / aryl e_1 / acetylene π \rightarrow DAD N p_π / aryl e_2 (38%)
146(8.50)	0.49					C ₁ -C _{1'} π / aryl a \rightarrow aryl e_2 (19%)

3.2.2 Exchange-Correlation Functional

The introduction of gradient corrections to density functional calculations carries a significant computational overhead, although for many purposes it is necessary to include such corrections to obtain good results. To investigate if this is the case for the systems under study here, some of the most widely used functionals, PW91,⁶ BLYP^{4,7-9} and BP86,^{4,10} were applied to calculations of transition energies in planar **2**. As for section 3.2.1, the geometry was optimised and the singlet-singlet electronic transition energies and oscillator strengths were calculated.

Similar to what was seen when the basis set was altered, the change in XC-functional altered the character of transitions with wavelengths below 200 nm. It would appear that the high energy transitions in this system are much more sensitive to the choice of computational parameters than the low energy transitions. Table 3.3 shows the results for the four lowest energy transitions only.

Table 3.3: Calculated wavelengths (nm), transition energies (eV) and oscillator strengths for planar **2** with different exchange-correlation functionals and the DZP basis set. Transitions with the same MO character (not given) are grouped together horizontally.

LDA(VWN)		PW91		BLYP		BP86	
Wavelength (Energy)	Osc. St.	Wavelength (Energy)	Osc. St.	Wavelength (Energy)	Osc. St.	Wavelength (Energy)	Osc. St.
404(3.07)	0.91	404(3.07)	0.89	399(3.11)	0.86	405(3.06)	0.88
271(4.57)	0.17	273(4.54)	0.20	272(4.56)	0.21	273(4.53)	0.20
235(5.28)	0.12	237(5.23)	0.13	235(5.26)	0.14	238(5.21)	0.13
195(6.37)	0.20	192(6.45)	0.12	192(6.44)	0.19	192(6.45)	0.22

It can be seen that inclusion of gradient corrections does not significantly alter any of the energies, the oscillator strengths or the MO characters of these transitions.

This is in contrast to the majority of the data reported by Matsuzawa *et al.*, but in agreement with their findings for benzene.⁴⁵ Since the primary interest of this study involves only the lower energy transitions, the computationally cheaper LDA approach was applied to subsequent calculations.

3.2.3 Solvent Surface

As the experimentally recorded absorption spectra have been obtained in solution, solvent effects were incorporated in the calculations using the COSMO approach (see section 1.8.1). Except when the influence of the polarity of the solvent was investigated (see section 3.5.9), DCM was the solvent of choice for all electronic transition energy calculations since this solvent was used when recording the experimental absorption spectra. ADF offers four different methods for modelling the COSMO solvent surface; ASURF, WSURF, ESURF and KLAMT.²⁹ Their effects on the electronic transitions of planar **2** were studied. In each case, the geometry was optimised and the singlet-singlet electronic transition energies and oscillator strengths were calculated. Table 3.4 shows that the choice of surface has little impact on the lower energy transitions and their oscillator strengths. The KLAMT surface was found to be the most stable method and hence was employed throughout the present work.

3.2.4 Conclusions

From the above discussion, it was concluded that a good computational model, which is computationally tractable, uses the DZP basis set in conjunction with the VWN parameterisation of the LDA and includes DCM as a solvent via the Klamt

Table 3.4: Calculated wavelengths (nm), transition energies (eV) and oscillator strengths for planar **2** with different solvent surfaces using the LDA(VWN) functional and the DZP basis set. Transitions with the same MO character are grouped together horizontally.

ESURF		WSURF		ASURF		KLAMT	
Wavelength (Energy)	Osc. St.	Wavelength (Energy)	Osc. St.	Wavelength (Energy)	Osc. St.	Wavelength (Energy)	Osc. St.
407(3.05)	0.91	408(3.04)	0.90	404(3.07)	0.91	404(3.07)	0.91
271(4.57)	0.17	272(4.56)	0.16	272(4.56)	0.16	271(4.57)	0.17

surface. Unless otherwise stated these are the parameters employed throughout the calculations reported in this chapter. Further studies on the basis set and XC-functional dependence of the electronic transition energies in palladium complexes will be discussed in section 3.5.

3.3 Comparison of Experimental and Calculated Geometries

3.3.1 Gas-phase Molecular Geometries

Before carrying out analysis of the electronic transitions, a comparison was made between the calculated geometries of selected compounds obtained in the gas-phase, i.e. without inclusion of the solvent, and those determined experimentally on similar systems. For these calculations, the symmetry was relaxed to C_2 , i.e. the planarity constraint was removed. Selected geometric parameters from the calculations and previous X-ray crystallographic studies are collected in table 3.5.

The general agreement between theory and experiment is satisfactory, with most bond lengths calculated to within 0.03 Å of the experimental values. The comparatively long central C_1-C_1' bond is computationally found to be slightly shorter than experiment. Compared with experiment, the calculated C_1-C_2 distance is slightly short and the acetylenic C_2-C_3 distance is slightly long. The C_1-N bond length shows the best agreement between calculated and experimental values, whereas the largest discrepancy (0.05 Å) is found for the $N-C_4$ bond length. As will be discussed later, the rotation of the phenyl rings had a pronounced effect on the absorption spectra and pleasingly, both the experimental and the calculated angles show that the aryl rings are significantly rotated out of the plane (indicated by $\angle C_1-N-C_4-C_5$ values greater than 50°). The exception to this occurs in the molecule with dimethyl amino substituents in the para position of the aryl rings (**6**), for which a coplanar geometry is favoured. However, further studies revealed that the potential energy surface for rotation of the aryl rings around the $N-C_4$ bond in **6** is very flat, with

Table 3.5: Selected computational and experimental geometric parameters for DAD molecules. Bond lengths are given in Å and bond/dihedral angles are given in °. The atom and compound numbering scheme is given in figure 3.3 on page 33.

Comp.	$r(\text{C}_1\text{-C}_1')$	$r(\text{C}_1\text{-N})$	$r(\text{C}_1\text{-C}_2)$	$r(\text{C}_2\text{-C}_3)$	$r(\text{N-C}_4)$	$r(\text{C}_3\text{-Si})$
1(calc)	1.468	1.286	1.406	1.217	1.384	1.815
2(calc)	1.474	1.280	1.412	1.207	1.380	-
6(calc)	1.472	1.289	1.418	1.210	1.364	-
17(exp) ⁴⁰	1.491	1.282	1.441	1.185	1.427	-
18(exp) ⁴⁰	1.491	1.272	1.442	1.196	1.427	1.847

Comp.	$\angle\text{N-C}_1\text{-C}_1'$	$\angle\text{N-C}_1\text{-C}_2$	$\angle\text{C}_1\text{-N-C}_4\text{-C}_5$
1(calc)	117.8	125.0	52.0
2(calc)	117.3	126.2	53.0
6(calc)	116.5	129.4	0.0
17(exp) ⁴⁰	117.8	125.2	55.1
18(exp) ⁴⁰	118.3	124.0	80.9

structures between 0° and 35° being almost isoenergetic. Thus, these results show that gas-phase ADF calculations satisfactorily reproduce the experimental (X-ray) geometries.

3.3.2 Molecular Geometry in Solution

The *E-s-trans-E* orientation invoked in the calculated geometries so far is found in the X-ray structures of **17** and **18**.⁴⁰ To find out which of the *s-cis* and *s-trans* conformations is favoured computationally in the present target systems, the barrier to rotation around the C₁-C_{1'} bond in planar **2** was calculated, including the effects of DCM as a solvent. Figure 3.4 shows that *s-trans* structure is 20 kJ/mol more stable than the *s-cis* structure and that the *s-cis* to *s-trans* conversion barrier has a somewhat higher value of 32 kJ/mol. From this and from the X-ray structures it

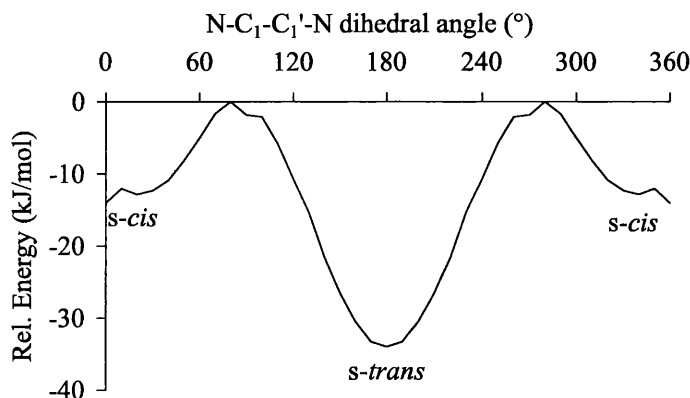


Figure 3.4: The relative total bonding energy of **2** as a function of the N-C₁-C₁'-N dihedral angle.

was concluded that the *s-trans* conformation is very likely dominant in solution and was therefore used for further studies.

As mentioned earlier, the orientation of the aryl rings around the N-C₄ bond is important since the angle of rotation greatly affects the absorption spectra. Investigation of the energies, intensities and MO characters of the longest wavelength transition in **2** showed that, as the C₁-N-C₄-C₅ dihedral angle is changed from 10° to 30°, the wavelength increases and the oscillator strength is more than doubled. Further increase of the dihedral angle causes a decrease in the oscillator strength and a further increase of the wavelength values (see figure 3.5). Even more significant changes occur for the short wavelength transitions. These changes make it particularly important to calculate the C₁-N-C₄-C₅ dihedral angle correctly. Therefore, both aryl rings in **2** were simultaneously rotated from $\angle C_1-N-C_4-C_5=0^\circ$ to 90° and the total bond energy was calculated at each $\angle C_1-N-C_4-C_5$ value (the step size was max 10°). C₂ symmetry was retained but all other geometric parameters were allowed to optimise. The potential energy surface for rotation of the aryl rings around the C-N bond turns out to be quite shallow ($\Delta < 20$ kJ/mol), as can be seen

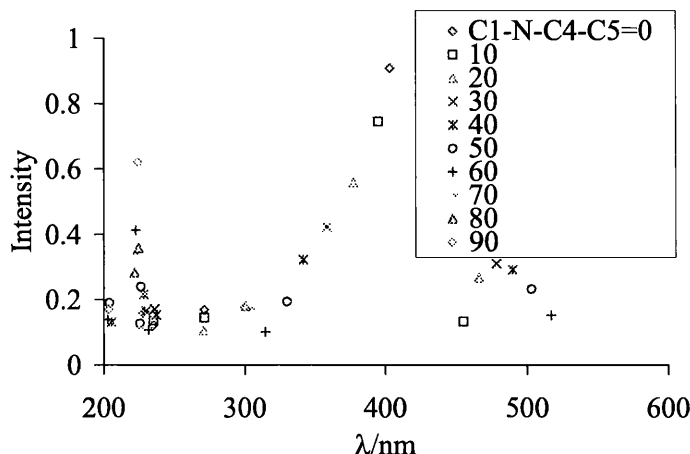


Figure 3.5: The change in transition energies and oscillator strength when gradually changing the $C_1-N-C_4-C_5$ dihedral angle, i.e. rotation of the aryl rings.

in fig 3.6. It was therefore concluded that it is possible that more than one conformation contributes to the absorption spectrum in solution. To account for the presence of these conformations, the calculated oscillator strengths were weighted by Boltzmann factors derived from their relative energies. The relatively shallow energy minimum for the rotation of the aryl rings causes all conformations at $C_1-N-C_4-C_5=50\pm 10^\circ$ to significantly influence the absorption spectrum for **2**.

3.3.3 Conclusions

Good agreement was found between the geometric parameters of calculated DAD molecules and those determined experimentally. It is especially pleasing that the calculated $C_1-N-C_4-C_5$ dihedral angle is considerably larger than 0° , i.e. the aryl rings are significantly rotated out of the plane of the DAD backbone which is in agreement with experiment. This dihedral angle proved to be very important when it came to calculating the electronic transition energies, as the energy and intensity

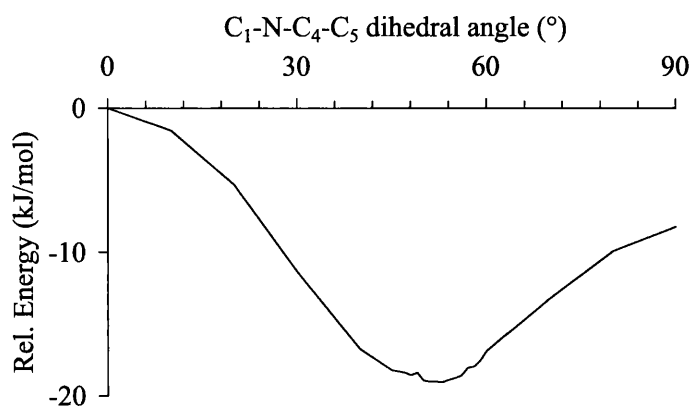


Figure 3.6: The relative bond energy of **2** as a function of the C₁-N-C₄-C₅ dihedral angle.

of the key low energy transitions were found to be strongly dependent upon the aryl ring dihedral angle as shown in figure 3.5. Given that the potential energy surface for rotation of the aryl rings around the N-C₄ vector is very shallow in all cases, it was concluded that electronic transitions would occur in solution from molecules with a variety of aryl ring orientations, and that the experimental spectra could not, therefore, be modelled correctly by a single molecular geometry. This was taken into account by calculating the electronic transition energies and intensities for molecules with aryl ring orientation around the potential energy minimum, with subsequent weighting of the transitions by a Boltzmann factor derived from the relative energies of the geometric structures.

3.4 Electronic Transitions and UV/Vis Spectra of 1,4-diazabuta-1,3-dienes

3.4.1 Comparison of the Calculated Electronic Absorption Spectrum of **2** with the Experimentally Determined Spectrum of **1**

The experimentally determined UV/Vis spectrum of **1**⁴⁰ is shown in figure 3.7, and the wavelengths of the first two bands are given in table 3.6. The calculated spectrum of **2** also shows two low energy bands, with maxima at 334 and 505 nm. Although the peaks in the calculated spectrum are shifted by 129 and 69 nm compared to the experimental spectrum of **1**, this corresponding to 0.84 and 0.96 eV, such discrepancies are common using TD-DFT and shifts of up to 1 eV are not unusual.^{14,46-48}

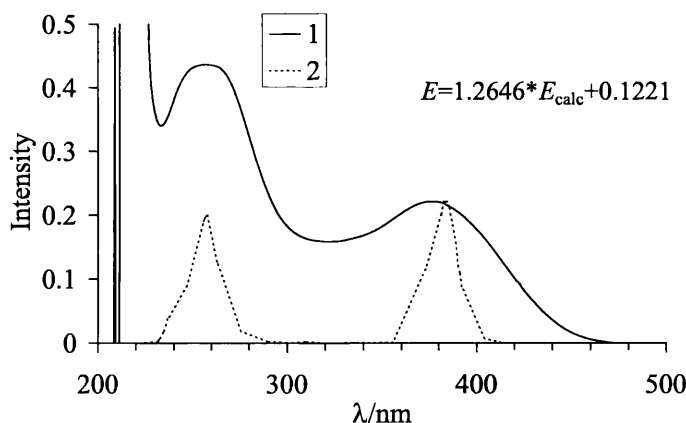


Figure 3.7: The experimental UV/Vis absorption spectrum of **1** and the simulated spectrum of **2**. The intensity of the longest wavelength peak in the simulated spectrum of **2** has been set equal to that in **1**.

In order to better compare the experimental and calculated spectra the calculated

Table 3.6: Experimental and calculated wavelengths and energies, and calculated orbital characteristics of the bands in the UV/Vis spectra of **1** and **2**. All transitions are of ${}^1B \leftarrow {}^1A$ symmetry.

λ_{max}/nm (Energy/eV)			Principal character of initial and final MOs
Comp. 1 (exp) ⁴⁰	Comp. 1 (calc)	Comp. 2 (calc)	
376(3.30)	391(3.17)	384(3.23)	DAD N p / aryl $e_1 \rightarrow$ DAD π_3 (97%, 2 ;95%, 1) ${}^i\text{Pr}_3\text{Si } \sigma \rightarrow$ DAD π_3 (96%)
265(4.68)	264(4.69)	258(4.80)	DAD π_2 / acetylene $\pi \rightarrow$ DAD π_3 (65%, 2 ; 50%, 1 , plus acetylene $\pi \rightarrow$ DAD π_3 (26%))
	262(4.73)	254(4.88)	DAD N p / aryl $e_1 \rightarrow$ acetylene π^* / DAD π_4 (59%, 2 ; 67%, 1)
	253(4.90)	238(5.21)	acetylene $\pi \rightarrow$ DAD π_3 (83%, 2 ;65%, 1)
	246(5.04)		acetylene π / ${}^i\text{Pr}_3\text{Si } \sigma \rightarrow$ acetylene π^* / DAD π_4 (69%)
	235(5.27)		${}^i\text{Pr}_3\text{Si } \sigma \rightarrow$ acetylene π^* / DAD π_4 (79%)
	226(5.48)		${}^i\text{Pr}_3\text{Si } \sigma$ / DAD N p / acetylene \rightarrow DAD π_3
	223(5.56)		${}^i\text{Pr}_3\text{Si } \sigma$ / acetylene \rightarrow DAD π_3
	219(5.66)		${}^i\text{Pr}_3\text{Si } \sigma$ / acetylene \rightarrow DAD π_3

energies were shifted according to equation 3.1

$$E = 1.2646 * E_{\text{calc}} + 0.1221 \quad (3.1)$$

with E_{calc} being the calculated transition energy in eV and E being the adjusted transition energy in eV. Figure 3.7 shows the adjusted calculated spectrum. Hereafter all references to calculated electronic transitions are to the transition energies that have been shifted according to equation 3.1. The calculated transition wavelengths and energies of **2** are collected in table 3.6.

In constructing figure 3.7, the long wavelength peak in both experimental and calculated spectra has been set to the same intensity. Clearly the intensity of the calculated short wavelength peak (258 nm) is underestimated. It is unclear whether

this discrepancy is due to the large atmospheric O₂ absorption peak in the experimental spectrum, just above 200 nm, enhancing this high energy peak such that in reality this peak should be of lower intensity, or due to the calculation underestimating the intensity.

Also given in table 3.6 are the principal characters of the calculated transitions in **2**. The longest wavelength band is found to be due to a $^1B \leftarrow ^1A$ transition made up almost entirely (97%) of promotion of an electron from the HOMO (23b) to the LUMO (25a). Figure 3.8 shows that the HOMO is a mixture of the e_1 level of the aryl rings and the DAD N out of plane lone pairs, while the LUMO is predominantly made up of DAD π_3 character.

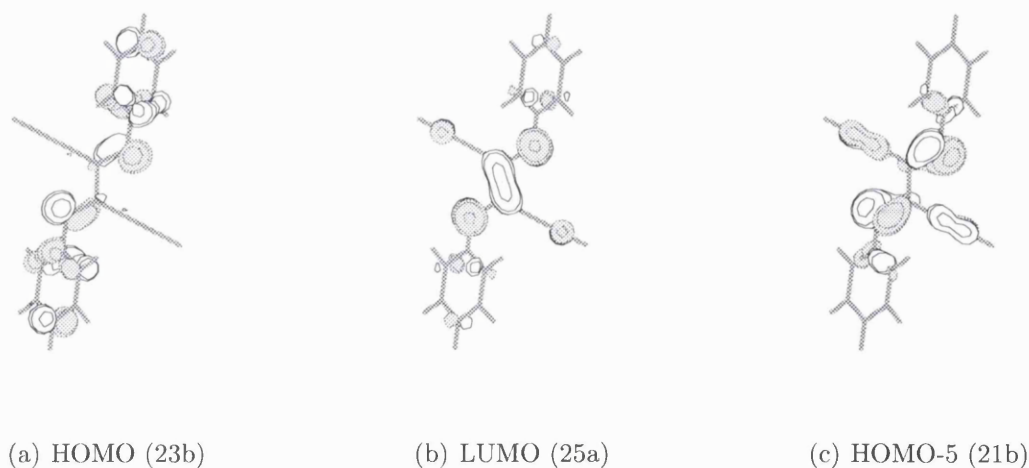


Figure 3.8: Three dimensional representations of selected MO's of **2**.

In the shorter wavelength band (at 258 nm), the destination orbital is again the LUMO but now the starting orbital is the HOMO-5 (21b, figure 3.8(c)), which is a mixture of DAD π_2 and the acetylenic π bonding level. An additional, less intense transition can be found that is almost isoenergetic with the 258 nm transition. This transition at 254 nm is due to the promotion of an electron from the HOMO-1 (24a)

to the LUMO+1 (24b), the characters of which are summarised in table 3.6. This band also has a high energy shoulder at 238 nm, due to the HOMO-7 (20b) to the LUMO (25a).

3.4.2 Comparison of the Calculated and Experimental Electronic Absorption Spectrum of **1**

Thus far, the experimental spectrum of **1**, which has $^i\text{Pr}_3\text{Si}$ groups attached to the acetylene units has been compared with the computed spectrum of a simplified structure in which the large $^i\text{Pr}_3\text{Si}$ groups were replaced by H atoms. The motivation for this was computational feasibility; $^i\text{Pr}_3\text{Si}$ substituted molecules are very large to be considered by full quantum mechanical approach and, as described in the previous section, it seems that the calculated spectrum of the H substituted system can be used to interpret that obtained experimentally on the $^i\text{Pr}_3\text{Si}$ substituted molecule. Despite this conclusion, an investigation into how the H \rightarrow $^i\text{Pr}_3\text{Si}$ substitution affects the simulated spectra was considered important, and hence the electronic transition energies of **1** were calculated. These calculations proved to be extremely time consuming, even on EV68 Compaq ES40 computers.

Calculation of the total molecular bonding energy as a function of C₁-N-C₄-C₅ dihedral angle produces results very similar to those shown in figure 3.6 for **2**, with the minimum energy conformation occurring at just above 50°. As before, the electronic transition energies of the conformations around the minimum energy structure were calculated, and these were Boltzmann-weighted in order to construct the computational absorption spectrum. This is shown in figure 3.9, with the transition energies and assignments collected in table 3.6. Comparison of figures 3.9 and figure 3.7 and examination of table 3.6 reveal that the introduction of $^i\text{Pr}_3\text{Si}$ groups

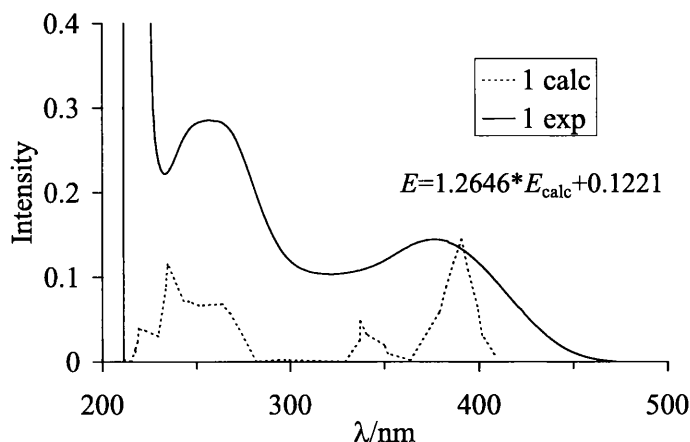


Figure 3.9: The experimental and simulated UV/Vis absorption spectrum of **1**. The intensity of the longest wavelength peak in the experimental spectrum has been set equal to that in the simulated spectrum.

significantly increases the complexity of the calculated absorption spectrum. Encouragingly, however, the three significant transitions found for **2** (384, 258 and 254 nm) are also present in **1** (391, 264 and 262 nm). The longest wavelength peak in the calculated spectrum of **1** was, as in **2**, due almost entirely to the promotion of an electron from the HOMO to the LUMO (53b→55a), the characters of which are the same for both **1** and **2**. Unlike in **2**, however, the calculations found a less intense transition in **1** at 337 nm, which lies quite close to the longest wavelength peak. While the starting orbital was now the HOMO-6 (51b), which is almost entirely localised on the ${}^i\text{Pr}_3\text{Si}$ fragments, the destination orbital is the same as in the longest wavelength transition, i.e. the LUMO.

The next calculated transition is at 264 nm, and is, in orbital terms, the closest equivalent of the 258 nm absorption found in **2**. The destination MO of the electron promotion primarily (50%) responsible for this absorption, is again the DAD π_3 LUMO, while the starting MO is the HOMO-8 (49b). A second promotion, which is

not present in **2**, also contributes significantly to this transition (26%), involving the mainly acetylenic π bonding HOMO-11 level and the LUMO. As with the longest wavelength transition, the 264 nm transition in **1** is slightly shifted bathochromically compared with the analogous transition in **2**.

The calculations for **1** found a transition almost isoenergetic with that of 254 nm found for **2**. Similar to **2**, this transition, at 262 nm, contains a significant amount of HOMO-1 (54a) \rightarrow LUMO+1 (54b) character. The next calculated transition, at 253 nm, is equivalent to the low intensity 238 nm transition in **2**, i.e. the primary MO character of this transition is the HOMO-11 acetylene π level \rightarrow DAD π_3 LUMO (55a). A whole series of transitions in a narrow wavelength/energy range (*c.* 245-220 nm) can then be found. None of these transitions are found in **2** and, consistent with this, all of the starting MOs in the associated electron promotions contain a significant amount of σ character from the $^i\text{Pr}_3\text{Si}$ units.

It was not completely clear from these calculations whether it was necessary to include the $^i\text{Pr}_3\text{Si}$ groups in order to adequately model the experimental absorption spectrum of **1**. As discussed in section 3.4.1, the experimental spectrum of **1** can be assigned on the basis of calculations on the model compound **2**. Inclusion of the $^i\text{Pr}_3\text{Si}$ groups in the computational model produces the more complicated spectrum shown in figure 3.9, but still results in more or less the same assignment of the bands.

3.4.3 Comparison of the Calculated Electronic Absorption Spectrum of **6** with the Experimentally Determined Spectrum of **5**

It has been found experimentally that introducing the strongly electron donating Me₂N group at the para position of the aryl rings results in a large bathochromic shift of the longest wavelength transition in the UV/Vis spectrum (see section 3.1). This is illustrated by comparing the data for compound **5**⁴⁰(given in table 3.7) with that of compound **1**, given in table 3.6. There are several things to note from this comparison. Firstly, the longest wavelength peak is bathochromically shifted by 110 nm compared with **1**. In contrast, the shorter wavelength peak of **1** (at 265 nm) is unchanged in **5**, although the peak displays a long wavelength shoulder in **5**, at 322 nm, which is not visible in **1**. Finally, it is noticeable that, by contrast to **1**, the 486 nm peak in the spectrum of **5** is significantly more intense than that at 264 nm.

Table 3.7: Experimental and calculated wavelengths and energies, and calculated orbital characteristics of the bands in the UV/Vis spectra of **5** and **6**.

All transitions are of ¹B←¹A symmetry.

λ_{max}/nm (Energy/eV)		Principal character of initial and final MOs
Comp. 5 (exp) ⁴⁰	Comp. 6 (calc)	
486(2.55)	418(2.96)	Me ₂ N N π / aryl e ₁ / DAD π_2 → DAD π_3 (96%)
322, sh.(3.85)	311(3.98)	DAD N p → DAD π_3 (97%)
	293(4.23)	Me ₂ N N π / aryl e ₁ / DAD π_3 → DAD π_4 / acetylene π^* (88%)
264(4.69)	251(4.94)	Me ₂ N N π / aryl e ₁ / π_3 → aryl e ₂ (71%)
	248(5.00)	DAD π_2 / aryl e ₁ / acetylene π → DAD π_3 (82%)
	229(5.41)	acetylene π → DAD π_3 (93%)

In order to gain insight into these observations, the electronic transitions of **6**,

a model for **5**, were calculated. As with **2**, it was assumed that the *E-s-trans-E* orientation prevails in solution. However, in contrast to **2**, as noted in section 3.3, it was found that the most stable orientation of the aryl rings is for a C₁-N-C₄-C₅ dihedral angle of 0°. Furthermore, the total molecular bonding energy was found to be largely unaffected by increasing this dihedral angle up to *c.* 35°, so there is a wider range of structures that contribute to the absorption spectrum than was found for **2**. It should also be noted that the Me₂N groups are almost coplanar with the aryl rings in the optimised geometries, implying sp² hybridisation at the dimethylamino N atoms.

The calculated transition wavelengths for **6** are given in table 3.7 and the calculated spectrum is shown in figure 3.10. The calculations agree with experiment in that they find that the longest wavelength transition in **6** is significantly shifted bathochromically compared with that of **2**. The computational shift of 34 nm is less than was observed experimentally (110 nm), but is, nevertheless, quite substantial. It is pleasing to note that this shift in energy is accompanied by a change in the character of the starting orbital responsible for this transition. Thus, while the finishing orbital is once again the DAD π₃ LUMO, the starting MO (32b HOMO) is now a mixture of DAD π₂, aryl e₁ and crucially, the π AO of the N atoms of the dimethylamino groups. This MO is shown in figure 3.11, from which it can be seen that the Me₂N N atom contribution is substantial. This is an important result as it directly connects the Me₂N substitution on the aryl ring and the bathochromic shift of the longest wavelength transition.

The calculations found three absorptions in **6**, which are equated with the higher energy experimental band (at 264 nm in **5**). These were calculated to have corrected (eq 3.1) wavelengths of 251, 248 and 229 nm respectively (see table 3.7), of which

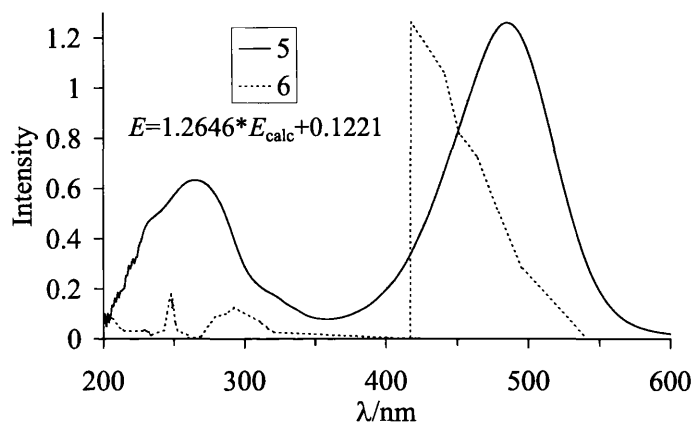


Figure 3.10: The experimental UV/Vis absorption spectrum of **5** and the simulated spectrum of **6**. The intensity of the longest wavelength peak in the simulated spectrum of **6** has been set equal to that in **5**.

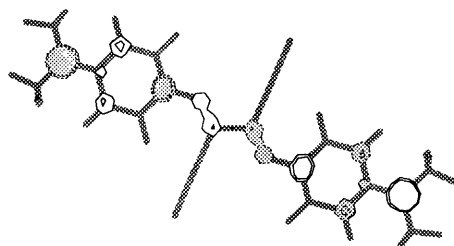


Figure 3.11: Three-dimensional representation of the HOMO (32b) of **6**.

the 248 nm transition is the most intense. The destination orbital for this transition is mainly the DAD π_3 LUMO (34a). The LUMO is quite similar to the LUMO of **2** and the localisation properties of the MOs responsible for the 248 nm transition are broadly similar to the analogous transition in **2** (258 nm). Unlike in **2**, however, there are two starting MOs (30b HOMO-4 and 29b HOMO-6), promotions from which make up 44% and 38% respectively of the overall ${}^1B \leftarrow {}^1A$ transition. These starting MOs are a mixture of DAD π_2 and acetylene π (as for **2**), with an additional contribution from aryl e_1 . Crucially, none of the MOs that give rise to the 248 nm absorption (30b, 29b and 34a) has a major contribution from the dimethylamino N atoms, explaining why the energy of the higher energy transition is largely unaffected by the para substituents on the aryl rings.

Of the two remaining calculated transitions in **6**, that are equated with the experimental band at 264 nm, the longer wavelength absorption (at 251 nm) is primarily composed of the promotion of an electron from the HOMO-1 (33a) to the LUMO+3 (34b). The HOMO-1 is a mixture of DAD π_3 , aryl e_1 and dimethylamino N π , the latter perhaps explaining why an analogous transition is not seen in **2**. The LUMO+3 is of aryl e_2 character. The higher energy transition, at 229 nm, is calculated to be very weak, and is equivalent to the somewhat more intense 238 nm transition found in **2**.

The third aspect of the experimental spectrum of **5** is the 322 nm shoulder, which is not seen for **1**. The calculated transitions at 311 and 293 nm for **6** are equated with this shoulder. Of the two transitions, the 293 nm is the more intense, and is primarily due to promotion of an electron from the HOMO-1 (33a) to the LUMO+1 (33b), of mixed DAD π_4 / acetylene π^* character.

When comparing the spectra of **2** and **1** (figure 3.7), the calculated and exper-

imental intensities of the longest wavelength peak were arbitrarily set to be equal. If the same is done for **5** and **6** (figure 3.10) it is found that the calculated intensity of the 248 nm peak is significantly smaller than the equivalent experimental band. Thus, as with **1** and **2**, the calculation does not reproduce exactly the relative intensities of the two peaks. However, the calculation does find that the longer wavelength peak in **6** is significantly more intense than the short wavelength peak, as is found experimentally in **5**.

3.4.4 Comparison of the Calculated Spectrum of 10 with the Experimentally Determined Spectrum of 9

Having examined the effect of Me₂N substitution on the UV/Vis spectrum, the effect of replacing the electron donating Me₂N by the electron withdrawing NO₂ was examined. Table 3.8 lists the calculated wavelengths, transition energies and oscillator strengths of **10** compared with the experimental data of **9**.⁴⁰ In contrast to **5**, no bathochromic shift of the long wavelength band was observed in either the calculated spectrum of **10** or the experimentally obtained spectrum of **9**.

The experimental spectrum of **9** contains three absorption bands with the long wavelength band (at 360 nm) being the weakest. The other two bands (at 302 and 230 nm) have approximately the same intensity.

Computationally, a transition at 381 nm (modified, eq 3.1) was found in **10** and equated to the band found experimentally at 360 nm. This transition is due to promotion of an electron from the HOMO (31b) to the LUMO (33a). The HOMO is, just as in **2**, of aryl e₁ and DAD N p character. The LUMO also agrees well with the findings in the other molecules in that it was found to be of DAD π₃ character. The MO characters for the calculated transitions can be seen in table 3.8.

The second peak, that was experimentally found at 302 nm, was computationally found to be due to two transitions at 284 and 268 nm. Of these, the transition at 284 nm, which is a HOMO to LUMO+2 transition, was found to be the most intense transition. The LUMO+2 is of O-N-O π^* and DAD N p_π character. The less intense transition, at 268 nm, is a transition from the HOMO-4 (30a) to the LUMO+1 (32b). The HOMO-4 is made up of the acetylenic π level and the e_1 level of the aryl rings whereas the LUMO+1 is mainly of O-N-O π^* character.

The highest energy experimental band at 230 nm was computationally found to be due to two almost isoenergetic transitions. Both of these are at 219 nm and are due to transitions from the HOMO-15 (24b) to the LUMO (33a) and from the HOMO-9 (27b) to the LUMO+2 (34a). The HOMO-9 is of NO₂ O π and N_{NO₂}-C σ character and HOMO-15 was of acetylene π and DAD N p character. Just as with the previously discussed molecules, the intensities of these high energy transitions are significantly underestimated.

3.4.5 Comparison of the Calculated Spectrum of **14** with the Experimentally Determined Spectrum of **13**

The interest in **13** stems from the existence of an electron donating substituent (Me₂N) in the para position of one aryl ring and an electron withdrawing substituent (NO₂) on the other. It has been suggested by Faust et al.⁴⁰ that **13** consists of two electronically decoupled molecular halves (see section 3.1). These workers carried out semi-empirical calculations on a model for **13** containing an NH₂ and an NO₂ substituent. The HOMO was found to be mainly located on the electron-rich amine half of the molecule and the LUMO on the electron-poor nitro half.

Table 3.9 compares the calculated wavelengths, transition energies and oscillator

strengths of **14** with the experimental data of **13**. **14** was the only molecule in which C_2 symmetry, for obvious reasons, could not be applied. The calculations were instead carried out without any symmetry constraints. Experimentally, three peaks are found of which one, at 302 nm, is a shoulder on the high energy peak. The other two peaks are of similar intensity.

The long wavelength peak found experimentally at 468 nm, was computationally found at 465 nm (modified, eq 3.1). This transition is due to promotion of an electron from the HOMO (64a) to the LUMO+1 (66a). The HOMO is found to be very similar to the HOMO found by Faust et al. for the NH_2/NO_2 substituted molecule. The orbital is made up of the e_1 level of the dimethyl amino substituted aryl ring and the dimethyl amino N π AO. The LUMO+1 was found to be of DAD π_3 and O-N-O π^* character.

A number of high energy transitions were found and were equated to the highest energy peak at 258 nm. The most intense of these is a transition at 283 nm. This transition is a transition from the HOMO-7 (57a) to the LUMO (65a, 33%), and from the HOMO-2 (62a) to the LUMO+1 (66a, 24%). The HOMO-7, situated on the NO_2 half of the molecule, is of acetylene π and aryl e_1 character. The LUMO is, in agreement with the findings of Faust *et al.*, located on the electron-poor half of the molecule, and is of O-N-O π^* , aryl e_1 and DAD N p_π character. The HOMO-2 on the other hand, is located on the electron-rich NMe_2 part of the molecule and is of dimethyl amino N π and DAD N p character.

Computationally, a third peak at 688 nm was found. This transition, which could not be equated to any absorption peak of **13** listed in table 3.9, is a HOMO to LUMO transition which can be seen as a kind of push-pull transition, with the electron going from the electron-rich half to the electron-poor half.

Table 3.8: Calculated wavelength (nm), energies (eV), oscillator strengths and excitation coefficients, calculated for **10** and obtained experimentally for **9**. The calculated orbital characteristics are also presented.

Comp. 9 (exp)		Comp. 10 (calc)		Principal character of initial and final MOs
λ_{max} (Energy)	Ext. coeff.	λ_{max} (Energy)	Osc. St.	
360(3.44)	11400	381(3.25)	0.22	DAD N p / aryl $e_1 \rightarrow$ DAD π_3 (94%)
302(4.10)	21100	284(4.36)	0.30	DAD N p / aryl $e_1 \rightarrow$ DAD N p_π / O-N-O π^* (46%)
230(5.39)	19200	268(4.63)	0.12	aryl e_1 / acetylene $\pi \rightarrow$ O-N-O π^* (61%)
		219(5.65)	0.09	DAD N p / acetylene $\pi \rightarrow$ DAD π_3 (44%)
		219(5.65)	0.09	O π / N_{NO_2} -C $\sigma \rightarrow$ DAD N p_π / O-N-O π^* (43%)

Table 3.9: Calculated wavelength (nm), energies (eV), oscillator strengths and excitation coefficients, calculated for **14** and obtained experimentally for **13**. The calculated orbital characteristics are also present.

Comp. 13 (exp)		Comp. 14 (calc)		Principal character of initial and final MOs
λ_{max} (Energy)	Ext. coeff.	λ_{max} (Energy)	Osc. St.	
		688 (1.80)	0.26	Me_2N aryl e_1 / Me_2N N $\pi \rightarrow$ NO_2 DAD N p_π / NO_2 aryl e_1 / O-N-O π^* (85%)
468 (2.65)	18400	465 (2.66)	0.27	Me_2N aryl e_1 / Me_2N N $\pi \rightarrow$ DAD π_3 / O-N-O π^* (80%)
302 (4.10), sh	11500	283 (4.38)	0.15	NO_2 aryl e_1 / NO_2 acetylene $\pi \rightarrow$ NO_2 DAD N p_π / NO_2 aryl e_1 / O-N-O π^* (33%)
258 (4.80)	17800			

3.4.6 Conclusions

The results of TD-DFT studies of the electronic transition energies of substituted diazabutadienes have been reported. Comparison of the simulated spectrum of **2** with the experimentally determined spectrum of **1** proved quite successful. The two experimental peaks above *c.* 200 nm were reproduced computationally, although calculation overestimates the wavelength of both peaks by *c.* 100 nm, a discrepancy not atypical of current TD-DFT methods. The longest wavelength peak was found to be due to promotion of an electron from the HOMO (of aryl e_1 and DAD N p character) to the DAD π_3 LUMO. The higher energy absorption is assigned to a predominantly DAD π_2 (with some acetylene π) \rightarrow DAD π_3 transition.

It was found that it was not necessary to include the computationally demanding $^i\text{Pr}_3\text{Si}$ substituents on the acetylenes to understand the experimental spectrum of **1** and hence the smaller and less computationally demanding H substituted acetylene units could be used (**2**).

The Me_2N substituted molecule was studied and the calculated transitions of **6** have been compared with those found experimentally for **5**. Experimentally, the higher energy peak in the spectra of both **1** and **5** lies at almost the same wavelength (265 and 264 nm), implying that the MO nature of the corresponding electronic transition is unaffected by *para* substitution of the aryl rings with dimethylamino groups. Computationally it was found that the main associated electronic transition in **6** is very similar to that discussed above for **2**, and has very little Me_2N character. By contrast, the longest wavelength peak in the spectrum of **5** is significantly bathochromically shifted with respect to the analogous peak in **1**. This is computationally rationalised by the significant Me_2N character of the HOMO in **6**,

leading to reduction in the HOMO-LUMO gap compared with **2**, and hence to a longer wavelength transition.

The high energy peak that was shown to be unaffected by *para* substitution by H (**1**) and Me₂N (**5**), was also found in the experimental spectra of **9** (NO₂ substituted) and **13** (NO₂ and Me₂ substituted) which had peaks at 230 and 258 nm. It was also found that the longest wavelength transition found computationally for **10** (381 nm) was a HOMO → LUMO transition of the same character as the transition found in **2** (384 nm). **14**, on the other hand, was found to have a long wavelength transition (465 nm) of similar character to the transition in **6** (418 nm).

It can thus be concluded that an electron donating *para* substituent such as Me₂N causes a bathochromic shift of the long wavelength transition due to interaction of the N lone pair with the π system on the aryl ring.

3.5 Electronic Transitions and UV/Vis Spectra of 1,4-diazabuta-1,3-diene Palladium(II) complexes

3.5.1 Importance of Exchange-Correlation Functional in Palladium Complexes

Given that transition metal complexes are often computationally more difficult than main group molecules, it was not certain in advance if the model chemistry developed for the free ligands would be appropriate for the Pd complexes. It was therefore decided to investigate the use of gradient corrections, as was done for the free ligands (see section 3.2.2). BP86 was used to optimise the geometry of **4** (figure 3.3, page 33) and the result compared with that obtained using the VWN functional. The basis set used was DZP, except for Pd for which a larger basis set of ADF type IV (see next section) was used. Relativistic effects were taken into account through the ZORA approach and DCM was included as a solvent using COSMO.

The potential energy minimum for aryl ring rotation in **4** was shifted to a larger angle (from 56° to 62°) when introducing gradient corrections to the XC-functional. In the free ligands there was such a shallow minimum that a small shift of dihedral angle was more or less insignificant; all conformations within 10° of the minimum contribute to the spectrum. However, it was found (see section 3.5.3 below) that the complexes possess a deeper energy well for aryl ring rotation than the free ligands, which results in only one conformation having a significant contribution to the spectrum and therefore the shift in minimum energy structure on moving from VWN to BP86 causes a difference in the final spectrum. Figure 3.12 compares the

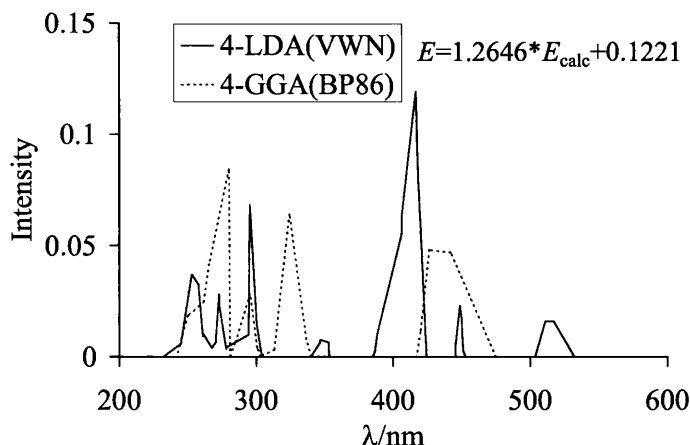


Figure 3.12: The simulated spectrum of **4** using two different exchange correlation functionals; LDA(VWN) and GGA(BP86).

calculated spectra obtained for **4** using LDA(VWN) and GGA(BP86).

For the ligand, it was seen (section 3.3) that both the intensities and the excitation energies change when the aryl rings are rotated. One question to be answered was whether or not the differences seen in figure 3.12 are due solely to the rotation of the aryl rings or if the inclusion of a gradient correction in the calculation of the excitation energies also contributes to this difference. In section 3.2.2 it was seen that including gradient corrections has little effect on the spectrum of the free ligand, but the assumption that this would also be true for the more complicated metal complexes is not justified without further investigation.

If the differences in figure 3.12 are due only to the different $C_1-N-C_4-C_5$ dihedral angle, the spectrum of the complex with the aryl rings fixed in a certain position but with all other geometric parameters optimised, calculated with and without gradient corrected methods, should result in very similar spectra. Table 3.10 contains the transitions that make up the intense band around 400 nm and shows that this is clearly not the case. The rotation of the phenyl rings from $\angle C_1-N-C_4-C_5=56^\circ$

Table 3.10: Calculated wavelengths (nm), transition energies (eV) and oscillator strengths for the band around 400 nm in **4**, using different exchange correlation functionals and rotating the aryl rings around C₁-N-C₄-C₅.

LDA(VWN) $\angle=56^\circ$		LDA(VWN) $\angle=62^\circ$		BP86 $\angle=62^\circ$	
Wavelength (Energy)	Osc. St.	Wavelength (Energy)	Osc. St.	Wavelength (Energy)	Osc. St.
419(2.96)	0.10	425(2.92)	0.04	444(2.79)	0.04
416(2.98)	0.02	419(2.96)	0.05	438(2.83)	0.05
450(2.75)	0.02	454(2.73)	0.02	472(2.63)	0.02
407(3.04)	0.07	405(3.06)	0.08	421(2.94)	0.03
391(3.17)	0.008	400(3.10)	0.003	427(2.90)	0.03

to 62° causes, just as was seen for the ligand in section 3.3.2, changes in oscillator strengths. However, significant differences can also be seen, especially in the excitation energies, between the transitions obtained with the LDA(VWN) at $\angle C_1-N-C_4-C_5=62^\circ$ and those obtained with the GGA(BP86) at $\angle C_1-N-C_4-C_5=62^\circ$. This prompted further studies to find the cause of these differences. Table 3.11 shows how the inclusion of gradient corrected methods in the calculation of the excitation energies, affects the spectrum. The first two transitions in table 3.11 are subject to a more significant separation in intensity when gradient corrections are included in the excitation energy calculations (compare column 1 with 2 and column 3 with 4), and experience a bathochromic shift when gradient corrections are included in the geometry optimisation (compare column 1 with 3 and column 2 with 4).

The last three transitions also experience a change in the oscillator strength when BP86 is used in the excitation energies. Once again a bathochromic shift is observed when including the gradient corrections in the geometry optimisation.

In summary, all transitions experience a small change in the oscillator strengths

Table 3.11: Calculated wavelengths (nm), transition energies (eV) and oscillator strengths for the band around 400 nm in **4**, using different XC-functionals and with the aryl rings fixed at $C_1-N-C_4-C_5=62^\circ$. The XC-functional used in the geometry optimisation is given first, followed by the XC-functional used in the calculation of excitation energies.

LDA(VWN)// LDA(VWN)		LDA(VWN)// BP86		BP86// LDA(VWN)		BP86// BP86	
Wavelength (Energy)	Osc. St.	Wavelength (Energy)	Osc. St.	Wavelength (Energy)	Osc. St.	Wavelength (Energy)	Osc. St.
425(2.92)	0.04	428(2.89)	0.03	442(2.80)	0.05	444(2.79)	0.04
419(2.96)	0.05	421(2.94)	0.06	436(2.84)	0.04	438(2.83)	0.05
454(2.73)	0.02	454(2.73)	0.01	474(2.61)	0.03	472(2.63)	0.02
405(3.06)	0.08	405(3.06)	0.04	427(2.90)	0.05	421(2.94)	0.03
400(3.10)	0.003	404(3.07)	0.05	419(2.96)	0.01	427(2.90)	0.03

when including gradients in the geometry optimisation but the most significant effect at this stage is the bathochromic shift (15-20 nm). Including gradient corrections in the excitation energy calculations has a minor effect on the transition energies but a more significant effect on the oscillator strengths. Overall, however, it was decided that the inclusion of the computationally more expensive gradient corrected methods in the metal complexes was not absolutely necessary, given that the main aim of the study was to establish the character of the transitions and approximate transition energies (particularly the long wavelength NIR transition). As discussed in section 3.2.2, there was no need for GGA methods in the investigations of the electronic transitions in the electronically less complicated ligands, and it was decided that it was justified to carry out all future calculations on the palladium complexes also using just the LDA(VWN).

3.5.2 Importance of Basis Set in Palladium Complexes

It was decided to model the Pd atom using the ADF type IV basis set (a SZ basis set for the core, DZ for the 4s orbitals, TZ for the 4p, 4d and 5s orbitals and an extra 5p function). Since the 2000 version of ADF, there is also the possibility to add a 4f polarization function to Pd when using the ZORA approach (ADF type V basis set). It was considered important to see how this polarization function on the metal would affect the transition energies in the palladium complexes. A geometry optimisation of **4** using the extended basis set and the LDA(VWN) results in a slight elongation of the Pd-Cl and Pd-N bonds (0.012 and 0.014 Å) and a small increase in the C₄-N-C₁ and N-C₁-C₁' angles (0.2 and 0.3°). The C₁-N-C₄-C₅ dihedral angle was allowed to rotate freely and the result was, with or without the extra polarization function, an angle of 56°. Table 3.12 shows the effect of the polarization function on the transition energies. There is a slight shift to shorter wavelengths when adding the 4f polarization function but the most noticeable result is the change in oscillator strength for the long wavelength band. Even though the changes in the intensities are noticeable, MO analysis suggested that the assignment of these transitions does not change, and since there is little information on the accuracy of the calculated intensities, it was decided that the changes induced by the extra 4f function do not justify their inclusion in further calculations.

It has thus been found that LDA(VWN) together with the ADF type IV basis set for Pd is sufficient for the aim of this project and is used for further calculations on the palladium complexes.

Table 3.12: Calculated wavelengths (nm), transition energies (eV) and oscillator strengths for 4 at the geometry optimised with and without a 4f polarisation function in the basis set of palladium. The transition energies are calculated with the same basis set that was used to optimise the geometry.

no polarisation function		4f polarisation function	
Wavelength (Energy)	Osc. St.	Wavelength (Energy)	Osc. St.
450(2.75)	0.021	444(2.79)	0.018
419(2.96)	0.102	416(2.98)	0.073
416(2.98)	0.025	412(3.01)	0.052
407(3.05)	0.067	402(3.08)	0.077
301(4.12)	0.014	299(4.14)	0.021
296(4.19)	0.001	295(4.20)	0.002
295(4.20)	0.069	285(4.35)	0.066
273(4.54)	0.029	271(4.57)	0.020
257(4.82)	0.033	255(4.86)	0.039
255(4.86)	0.032	248(5.00)	0.026
253(4.90)	0.041	251(4.94)	0.042
236(5.25)	0.047	235(5.27)	0.043

3.5.3 Comparison of Experimental and Calculated Geometries of the Palladium Complexes

Before proceeding further, a difficulty encountered in all geometry optimisations on the palladium complexes should be mentioned. The palladium complexes (see figure 3.3(b)) possess C_2 symmetry but constraining the geometry of the molecules to this point group proved problematic. An attempt to optimise the geometry of the model complex **4** in C_2 symmetry caused oscillations of the energy gradient and the geometry could not be optimised in this point group. Instead, the geometry optimisation could only be achieved by completely removing the symmetry constraints and hence all calculations on palladium complexes (both those already discussed and those below) were carried out without confining the molecule to any symmetry.

The geometry of the complexes, just as the free ligand, were calculated to be in good agreement with X-ray crystallographic data. As an example, table 3.13 shows the geometric parameters obtained experimentally for **11**³⁵ and computationally for **12** using the parameters established in sections 3.5.1 and 3.5.2.

Table 3.13: Selected experimental and computational geometric parameters for **11** and **12** respectively. Bond lengths are given in Å, bond/dihedral angles are given in °.

Comp.	$r(C_1-C_1')$	$r(C_1-N)$	$r(Pd-N)$	$r(Pd-Cl)$
11 (exp)	1.429	1.293	2.024	2.256
12 (calc)	1.441	1.311	1.985	2.241

Comp.	$\angle N-C_1-C_1'$	$\angle N-C_1-C_2$	$\angle N-Pd-N$	$\angle Cl-Pd-Cl$	$\angle C_1-N-C_4-C_5$
11 (exp)	115.2	124.5	79.1	90.7	77.5
12 (calc)	115.2	124.5	79.3	91.2	70.0

The diazabutadiene backbone in the complex was restricted to the *s-cis* conform-

ation to enable complexation with the palladium atom (as shown in figure 3.3(b)). Rotation of the phenyl rings around the N-C bond is still possible but the potential surface for this rotation turned out to be less shallow than for the free ligands (as noted in section 3.5.1), with energy differences between the lowest and highest energy conformations of around 150 kJ/mol compared to 20 kJ/mol for the free ligands. The effect of this deep well was that only one or two conformations had any significant contribution to the absorption spectra when the Boltzmann weighting was applied, making it much more crucial to establish the minimum energy structures correctly. This is discussed further for the individual complexes in their respective sections.

3.5.4 The Calculated Electronic Structure of 4 and Comparison of the Calculated Electronic Absorption Spectrum of 4 with the Experimentally Determined Spectrum of 3

Figure 3.13 shows the calculated molecular orbital diagram for 4 at the minimum energy geometry and figure 3.14 shows three dimensional representations of some of those orbitals. The five highest occupied orbitals are of palladium d, palladium s or chlorine π character. The HOMO-5 to the HOMO-8 are mainly the e_1 level of the aryl rings but with a contribution from the palladium d_{z^2} and the DAD N p π in the HOMO-5 and from the acetylene π bonding level in the HOMO-6. In square-planar palladium the d orbitals with z-character (d_{z^2} , d_{xz} and d_{yz}) are expected to be lower in energy than $d_{x^2-y^2}$ and d_{xy} . This is generally true in figure 3.13, although mixing with the ligand orbitals changes the pure crystal field theory ordering. The two d_{z^2} containing orbitals are of lower energy than the other orbitals that have palladium

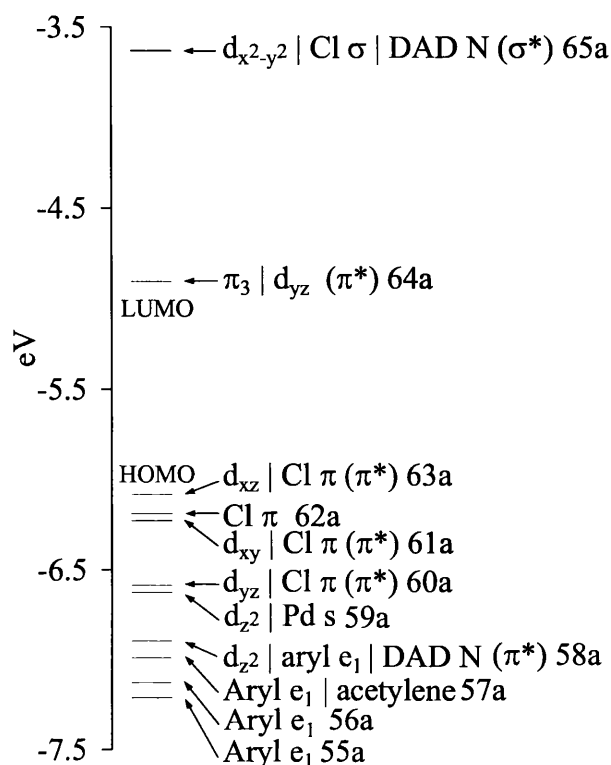


Figure 3.13: Molecular orbital energy level diagram for **4**.

character. The HOMO-4, which is mainly of Pd d_{z^2} character but with a small contribution from Pd s , is the most AO-like. Compared to this orbital, the HOMO-5 is stabilised by the contribution from the e_1 orbital level of the aryl rings despite the anti-bonding interaction with the nitrogen on the DAD backbone. There are two orbitals that are of d_{yz} character and one of d_{xz} character. The d_{xz} -based MO is antibonding with respect to the Cl p_π , as is one of the d_{yz} containing orbitals, but the latter interaction is smaller and this MO is therefore not destabilised to the same extent as the d_{xz} orbital. The other orbital containing the d_{yz} orbital is anti-bonding with the DAD π_3 level and is destabilised to become the LUMO. The d-based MO of highest energy contains the $d_{x^2-y^2}$ orbital and in **4** this orbital is σ anti-bonding with both the chlorines and the nitrogen.

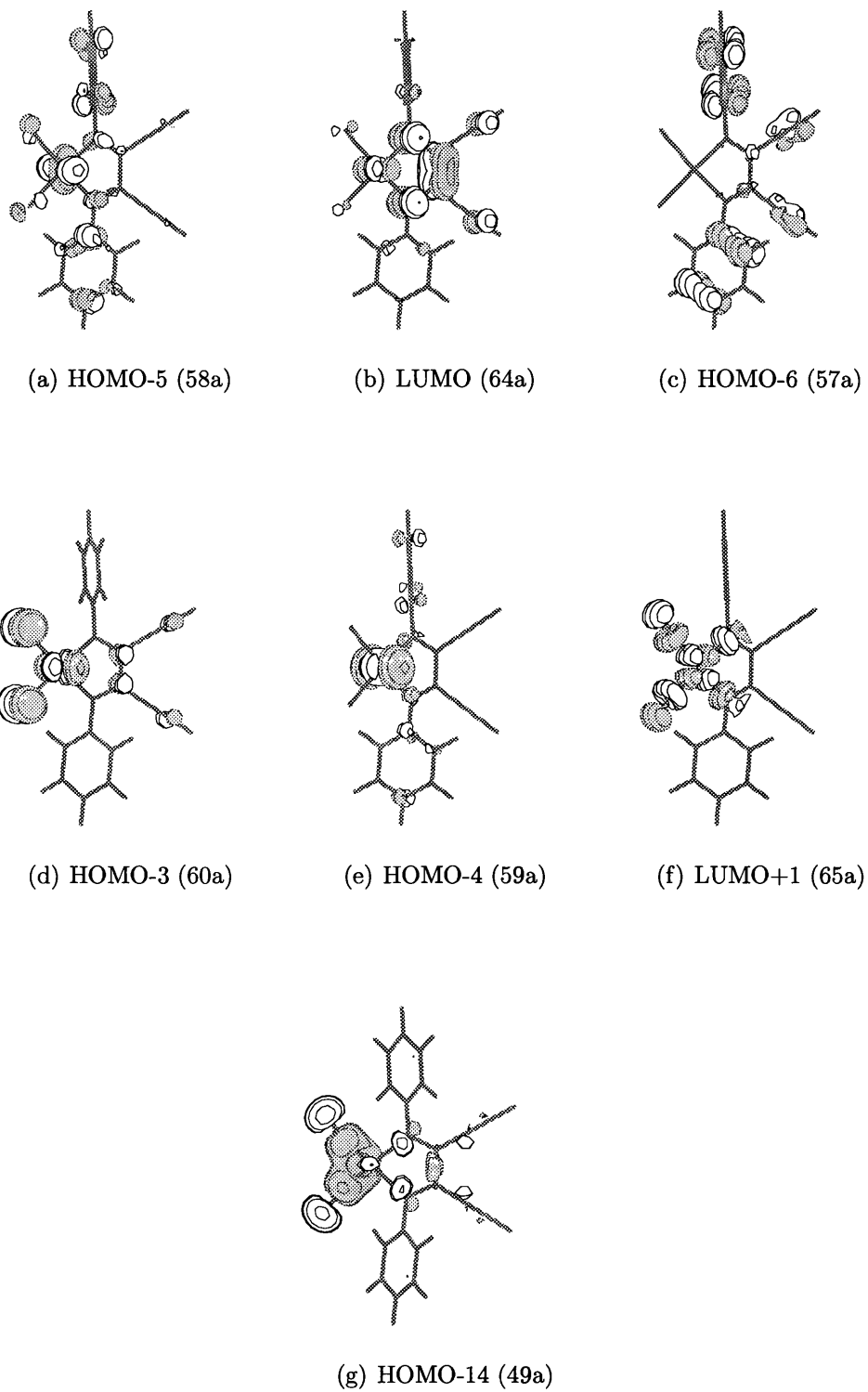


Figure 3.14: Three dimensional representations of selected MOs of 4.

Experimentally the absorption spectrum for the palladium complex of the unsubstituted molecule (**3**, see appendix A for experimental procedure and figure 3.15 for the absorption spectrum) shows three absorption bands, which is one more band than is found in the corresponding ligand (see figure 3.7). The additional peak is on the shoulder of the short wavelength peak (around 300 nm). The long wavelength band (around 400 nm), which looks as though it consists of more than one transition, is bathochromically shifted by 48 nm compared with **1** whereas the short wavelength band (around 250 nm) experiences only a minor hypsochromic shift of 17 nm compared with **1**. The intensities have increased for all of the peaks but the order is the same, i.e. the high energy band is still the most intense band.

Figure 3.15 also shows the computationally obtained spectrum of **4** and table 3.14 summarises the MO character of the calculated transitions. The lowest energy calculated transitions (511 and 449 nm) are of very low intensity and are therefore not included in table 3.14. However, these transitions, which are due to transitions from the palladium and chlorine centred orbitals to the LUMO (64a), can be seen in figure 3.15.

Computationally, a low energy band of significant intensity was found, mainly made up of two transitions, at 417 nm and 407 nm, and this band was equated to the band at 425 nm in the experimental spectrum. The transition at 417 nm, the more intense of the two, was found to be due to a transition made up almost entirely (81%) of the promotion of an electron from the HOMO-5 (58a) to the LUMO (64a). Figure 3.14(a) shows that the HOMO-5 is, as mentioned earlier, a mixture of the e_1 level of the aryl rings and the DAD N p_π , similar to the HOMO in **2**, but with a major contribution from the d_{z^2} orbital of the palladium. The LUMO (figure 3.14(b)) resembles the LUMO of the free ligand (**2**) in that it is of DAD π_3

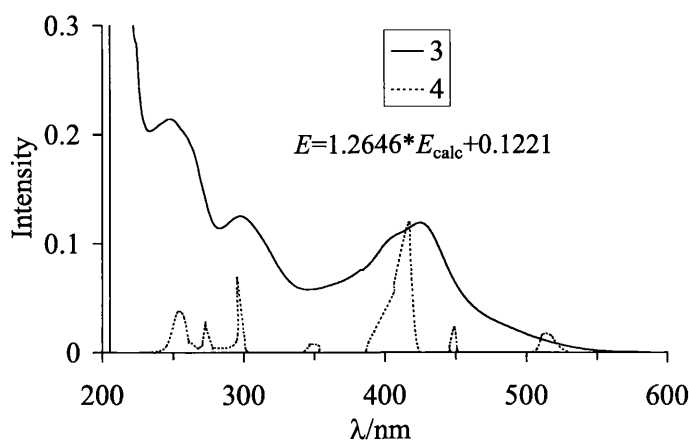


Figure 3.15: The experimental UV/Vis absorption spectrum of **3** (solid line) and the simulated spectrum of **4** (dashed line). The intensity of the most intense band in the simulated spectrum of **4** has been set equal to that of the longest wavelength transition band in **3**.

Table 3.14: Experimental and calculated wavelengths and energies, and calculated orbital characteristics of the bands in the UV/Vis spectra of DAD Palladium complexes. Calculated wavelengths and energies have been modified according to equation 3.1.

λ_{max}/nm (Energy/eV)		Principal character of initial and final MOs
Comp. 3 (exp) ^a	Comp. 4 (calc)	
425(2.91)	417(2.97)	aryl e_1 / d_{z^2} / DAD N p_π \rightarrow DAD π_3 / d_{yz} (81%)
	407(3.05)	aryl e_1 / acetylene π \rightarrow DAD π_3 / d_{yz} (41%) d_{yz} / Cl p_π \rightarrow DAD π_3 / d_{yz} (38%)
298(4.16)	295(4.19)	d_{z^2} / Pd s \rightarrow $d_{x^2-y^2}$ / Cl σ / DAD N p^* (64%)
248(5.00)	273(4.54)	acetylene π / d_{yz} / Cl p_π \rightarrow DAD π_3 / d_{yz} (56%)
	255(4.86)	aryl e_1 \rightarrow $d_{x^2-y^2}$ / Cl σ / DAD N p^* (81%)
	253(4.90)	d_{z^2} / Cl σ / DAD N p^* \rightarrow DAD π_3 / d_{yz} (65%)

^a See appendix A

character but the metal complex has an additional contribution from the palladium d_{yz} orbital. The receiving orbital in the transition at 407 nm was found to be the same as for the transition at 417 nm but the starting orbitals are the HOMO-6 (57a, 41%) and the HOMO-3 (60a, 38%). The HOMO-6 (figure 3.14(c)) is, as mentioned earlier, of pure ligand character and is a mixture of the e_1 level of the aryl rings and the acetylenic π bonding level. The HOMO-3 (figure 3.14(d)), on the other hand, is predominantly of d_{yz} and chlorine p_π character.

The experimental band at 298 nm, which is not present in **2**, is equated with the transition found computationally at 295 nm. This may be characterised as a palladium ligand field transition which is made up predominantly (64%) of promotion of an electron from the HOMO-4 (59a, figure 3.14(e)), that has Pd d_{z^2} and Pd s character, to the LUMO+1 (65a, figure 3.14(f)), that has Pd $d_{x^2-y^2}$, Cl σ and DAD N p character.

The high energy band found computationally between 273 to 253 nm is, just as the high energy band in **2**, made up of a number of almost isoenergetic transitions. The most intense of these transitions is the transition at 253 nm, which is made up mainly (65%) of the promotion of an electron from the HOMO-14 (49a, figure 3.14(g)) to the LUMO (64a). This is a transition from an MO of Pd d_{z^2} /Cl p /DAD N $p \sigma^*$ character to the π_3 orbital of the DAD ligand and the Pd d_{yz} level. The other two, less intense transitions at 273 and 255 nm, are due to transitions from acetylene $\pi/d_{yz}/Cl p_\pi$ to DAD π_3/d_{yz} and aryl e_1 to $d_{x^2-y^2}/Cl \sigma/DAD N p$ respectively. Just as was seen in the ligands, the intensities of these high energy transitions are significantly underestimated in comparison with experimental results.

3.5.5 Comparison of the Calculated Electronic Absorption Spectrum of **8** with the Experimentally Determined Spectrum of **7**

In section 3.4.3, it was shown that the introduction of the strongly electron donating Me₂N group at the para position of the aryl rings of the DAD causes a bathochromic shift of the long wavelength transition, and that this shift occurs in both the experimental and the calculated spectrum. The experimental spectrum of the Me₂N-substituted complex **7** also shows a bathochromic shift of the long wavelength transition (781 nm compared with the unsubstituted complex **3** (425 nm)).³⁵ This transition is also, just as in **3**, significantly shifted to a longer wavelength compared to the free ligand. It is of particular interest to determine the character of this transition as it lies in the NIR region of the spectrum. The spectrum also has two intense peaks at 229 and 257 nm and two less intense peaks at 308 and 399 nm.

The calculated potential energy curve for rotation of the aryl rings about the C-N bond of **8** (a model for **7**) consists of many local minima and a global minimum for this distortion could not be determined. This problem seemed to arise when including solvent in the calculation and therefore the corresponding energy curve for **8** was calculated in the gas phase. A $\angle C_1-N-C_4-C_5$ minimum was found at 47°. The potential energy curve obtained in gas-phase was used to carry out the Boltzmann weighting on transition energies obtained from calculations carried out in solution. As with **4**, the minimum found in vacuo for **8** is deep and hence only one structure makes a significant contribution to the absorption spectrum.

Figure 3.16, a valence molecular orbital energy level diagram for **8**, shows that, in contrast to **4**, where the HOMO is of palladium d character (figure 3.13), the

HOMO in **8** is made up of the e_1 level of the aryl rings and of dimethyl amino π^* character. In fact the HOMO is one of the two occupied aryl-centred orbitals in **4** that are destabilised by the antibonding interaction between the N p_π lone pair and the aryl ring and, as a result, are of higher energy than the five occupied palladium d and Cl π orbitals. This destabilisation of two aryl based orbitals is expected to have a major effect on the electronic absorption spectra. The remaining two aryl orbitals do not have any contribution from the dimethyl amino nitrogen and are therefore, more or less, unaffected by the substitution. Unlike in **4**, the low intensity transition from a palladium d-centred orbital to the LUMO is no longer the lowest energy transition possible (i.e. the HOMO is no longer of metal d character). This gives rise to the possibility of a more intense transition from the HOMO (81a) to the LUMO (82a) which will now be discussed.

Figure 3.17 shows the experimental spectrum of **7** and the calculated spectrum of **8** (modified according to equation 3.1) and the MO characters of the calculated transitions are given in table 3.15. As for the corresponding ligand (**6**), DFT underestimates the intensity of the short wavelength transitions with the result that they are barely visible compared with the longer wavelength transitions. A discussion of the shorter wavelength transitions (below 400 nm) in **6** is therefore not feasible and the discussion is confined to the longer wavelength transitions.

It can be seen in figure 3.17 that equation 3.1 do not work very well for this system, and there is still a reasonable difference between the experimentally obtained spectrum and the simulated spectrum.

The low energy transition at 697 nm is equated to the low energy band at 781 nm in the experimental spectrum. This transition was found to be due to a transition made up almost entirely (91%) of the promotion of an electron from the HOMO

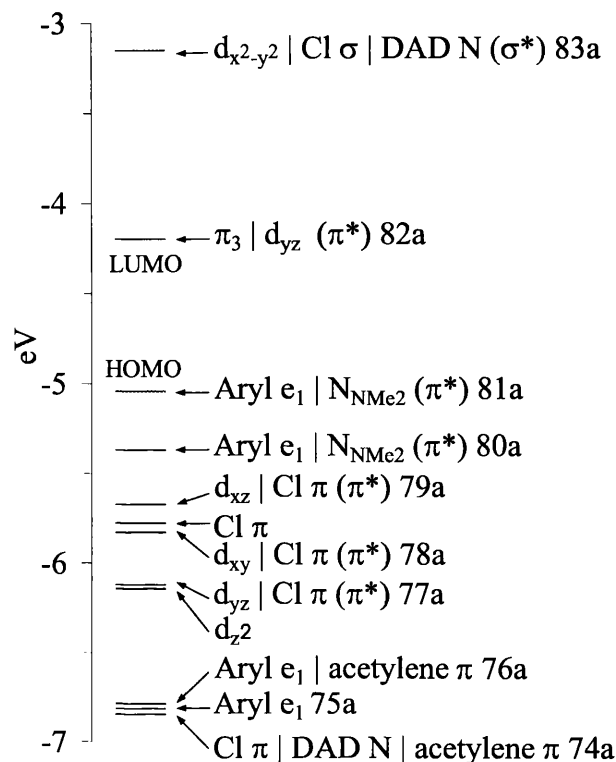


Figure 3.16: Molecular orbital energy level diagram of **8**.

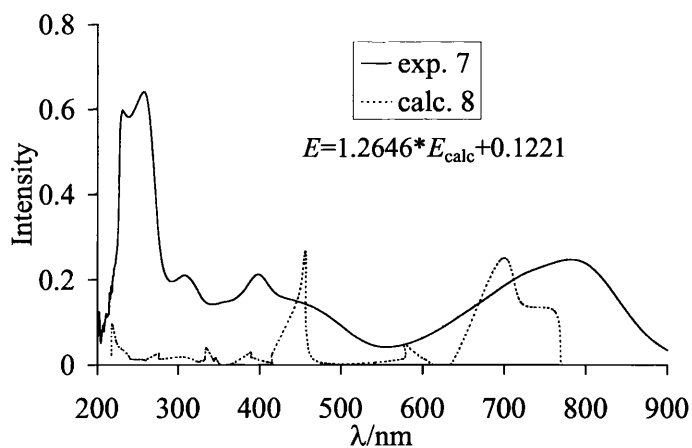


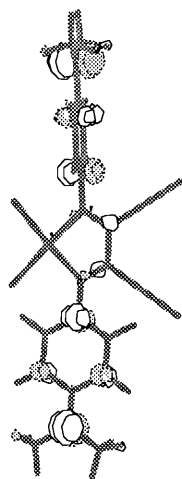
Figure 3.17: The experimental UV/Vis absorption spectrum of **7** (solid line) and the simulated spectrum of **8** (dashed line). The intensity of the longest wavelength peak in **7** has been set equal to that of the second longest wavelength peak in the simulated spectrum of **8**.

Table 3.15: Experimental and calculated wavelengths and energies, and calculated orbital characteristics of the bands in the UV/Vis spectra of DAD Palladium complexes. Calculated wavelengths and energies have been modified according to equation 3.1.

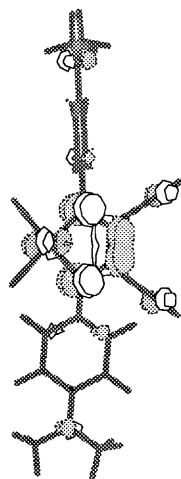
λ_{max}/nm (Energy/eV)		Principal character of initial and final MOs
Comp. 7 (exp) ³⁵	Comp. 8 (calc)	
781(1.59)	697(1.78)	aryl e_1 / Me ₂ N N π \rightarrow DAD π_3 / d_{yz} (91%)
399(3.11)	456(2.72)	aryl e_1 / Me ₂ N N π \rightarrow $d_{x^2-y^2}$ / Cl π / DAD N (68%) d_{z^2} \rightarrow DAD π_3 / d_{yz} (23%)
308(4.02)		
257(4.82)		
229(5.41)		

(81a) to the LUMO (82a). Figure 3.18(a) shows that the HOMO, as mentioned earlier, is a mixture of the e_1 level of the aryl rings and the p_π AO of the dimethyl amino nitrogens. The LUMO (figure 3.18(b)) has similar character to the LUMO of **4**, i.e. DAD π_3 and palladium d_{yz} character. The long wavelength transition in **8** is thus found to be an intramolecular charge transfer from the outer aryl rings to the central DAD backbone and the palladium.

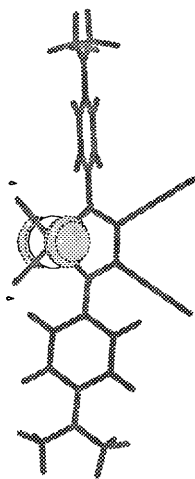
The only other intense transition, at 456 nm, is equated to the 399 nm band in the experimental spectrum and is found to be due to the promotion of an electron from the HOMO (81a) to the LUMO+1 (83a, 68%) and to a lesser extent from the HOMO-6 (75a) to the LUMO (82a, 23%). The LUMO+1 (83a, figure 3.18(d)) is made up of contributions from the palladium $d_{x^2-y^2}$, the Cl σ and one of the lone pair combinations of the DAD nitrogen. The HOMO-6 (75a, figure 3.18(c)) is made up of the d_{z^2} level of the palladium with a small contribution from palladium s.



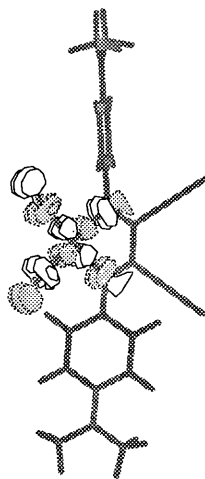
(a) HOMO (81a)



(b) LUMO (82a)



(c) HOMO-6 (75a)



(d) LUMO+1 (83a)

Figure 3.18: Three dimensional representations of selected MOs of **8**.

3.5.6 Comparison of the Calculated Electronic Absorption Spectrum of **12** with the Experimentally Determined Spectrum of **11**

The study of the palladium complexes has so far been concerned with complexes with a hydrogen or an electron withdrawing dimethyl amino group in the para position of the aryl rings. Just as in the study of the free ligands, it was also of interest to examine **11**,³⁵ which has electron donating nitro groups in the para position.

The longest wavelength band in the experimentally recorded spectrum of **11** (data given in table 3.16) lies at 436 nm, which is only slightly bathochromically shifted (by 11 nm) compared to **3** (425 nm) but significantly shifted to a longer wavelength compared to **9** (360 nm). The long wavelength band has a shoulder at 416 nm, of only marginally lower intensity. The most intense band is the high energy band which consists of two peaks at 264 and 230 nm.

Table 3.16: Wavelength (nm), energies (eV), extinction coefficients and oscillator strengths, calculated for **12** and obtained experimentally for **11**. The calculated orbital characteristics are also presented.

Comp. 11 exp ³⁵ λ (Energy)	Ext. coeff.	Comp. 12 calc λ (Energy)	Osc. st.	Principal character of initial and final MOs
436(2.84)	12900	445(2.78)	0.07	$d_{yz} / \text{Cl } \pi \rightarrow \text{DAD } \pi_3 / d_{yz}$ (80%)
416(2.98)	10900	377(3.29)	0.07	$\text{aryl } e_1 / d_{xz} / \text{DAD } \text{N} \rightarrow \text{DAD } \pi_3 / d_{yz}$ (42%)
264(4.69)	38300	282(4.40)	0.03	$d_{xz} / \text{DAD } \text{N} / \text{aryl } e_1 \rightarrow d_{x^2-y^2} / \text{Cl } \sigma /$ $\text{DAD } \text{N} / \text{O-N-O } \pi^*$ (72%)
230(5.39)	32300	276(4.49)	0.04	$\text{aryl } e_1 / \text{O-N-O } \pi^* \rightarrow \text{O-N-O } \pi^*$ (41%)
		264(4.70)	0.05	$d_{z^2} / \text{Pd } s \rightarrow d_{x^2-y^2} / \text{Cl } \sigma / \text{DAD } \text{N} /$ $\text{O-N-O } \pi^*$ (54%)

Figure 3.19 shows the calculated molecular orbital diagram for **12**, a model for

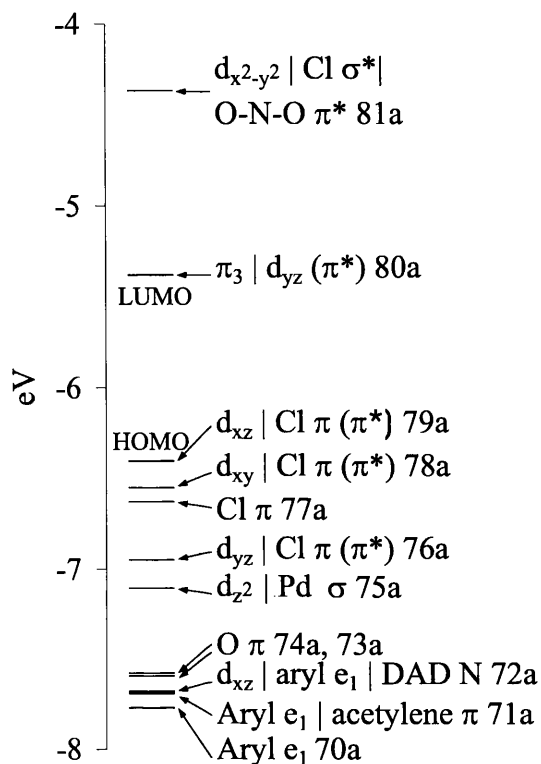


Figure 3.19: Molecular orbital energy level diagram for **12**.

11. The diagram is very similar to that of **4** (figure 3.13), with the HOMO to the HOMO-4 being located on the palladium and the chlorines, and with the orbitals made up of the aryl e_1 MO, appearing at lower energy. However, in between the metal-centred and the aryl-centred orbitals, there are two orbitals made up of the π AOs of the oxygens in the nitro groups (74a and 73a).

Computationally a transition at 445 nm was found, which is equated to the experimentally observed long wavelength band at 436 nm (see table 3.16). This transition was found to be due to the promotion of an electron from the HOMO-3 (76a) to the LUMO (80a, 80%). The HOMO-3 is made up of the d_{yz} level of the palladium and the π AO of the chlorines. The LUMO, like the LUMO in **4** and **8**, is made up of the DAD π_3 and Pd d_{yz} . An equivalent transition is also present in **4** at

449 nm, but it is much less intense and was therefore not included in section 3.5.4. The shoulder found experimentally at 416 nm, is found computationally at 377 nm. This is a transition between the HOMO-7 (72a) and the LUMO (80a). The HOMO-7 is of d_{xz} , aryl e_1 and DAD N p_π character and is thus very similar to the HOMO-5 in **4** with the exception of the palladium contribution.

In the region between 250-300 nm, a number of almost isoenergetic transitions are found and are equated to the high energy peaks at 264 and 230 nm in the experimental spectrum. The three most intense transitions are included in table 3.16. The transition at 282 nm is made up mainly (72%) of a transition between the HOMO-7 (72a) to the LUMO+1 (81a). The LUMO+1 is very similar to the LUMO+1 in the previously discussed complexes in that it has $d_{x^2-y^2}$, Cl σ and DAD N p character but the LUMO+1 in **12** also has a contribution from the O-N-O π^* . The transition at 276 nm is a transition between the HOMO-5 (74a) and the LUMO+2 (82a) which both have O-N-O π^* character but the HOMO-5 also has a small amount of aryl e_1 character. The marginally more intense transition at 264 nm is due to promotion of an electron from the HOMO-4 (75a) to the LUMO+3 (83a). The HOMO-4 is of Pd d_{z^2} and Pd s character and the LUMO+3 is made up of the same orbital character as LUMO+1 but with a stronger contribution from the $d_{x^2-y^2}$, Cl σ and DAD N p . Once again it can be seen that the intensities of the high energy transitions are significantly underestimated.

3.5.7 Comparison of the Calculated Electronic Absorption Spectrum of **16** with the Experimentally Determined Spectrum of **15**

In the study of the free ligands (section 3.4.5) it was shown that **13**, which has one Me₂N substituent and one NO₂ substituent, has a long wavelength transition (468 nm) at almost the same wavelength as **5**, which has two Me₂N substituents (486 nm). The palladium complex of **13**, i.e. **15**, shows similar behaviour to the free ligand;³⁵ table 3.17 indicates that **15** has a long wavelength transition at 777 nm, which is only slightly hypsochromically shifted compared to the long wavelength transition at 781 nm found in **7**. Three other transitions were found at 415, 257 and 228 nm (the latter two transitions are more intense).

Table 3.17: Wavelength (nm), energies (eV), extinction coefficients and oscillator strengths, calculated for **16** and obtained experimentally for **15**. The calculated orbital characteristics are also presented.

Comp. 15 exp ³⁵ λ (Energy)	Ext. coeff.	Comp. 16 calc λ (Energy)	Osc. st.	Principal character of initial and final MOs
777(1.59)	15600	736(1.68)	0.14	Me ₂ N aryl e ₁ / Me ₂ N N π → d _{yz} / DAD π ₃ (69%)
415(2.99)	13500	667(1.86)	0.10	d _{xz} / Clπ → d _{yz} / DAD π ₃ (47%)
		441(2.81)	0.08	d _{yz} / Cl π → d _{yz} / DADπ ₃ (66%)
		406(3.05)	0.06	Me ₂ N aryl e ₁ / Me ₂ N N π → d _{x²-y²} / Cl σ / DAD N (84%)
		353(3.51)	0.08	Me ₂ N aryl e ₁ / Me ₂ N acetylene π → d _{yz} / DAD π ₃ (39%)
257(4.82)	40200	290(4.27)	0.04	d _{xz} / Cl π → DAD π ₄ / acetylene π* (34%)
228(5.43)	37000	242(5.12)	0.08	d _{yz} / Cl π → DAD π ₄ / acetylene π* (41%)

Figure 3.20 shows the calculated molecular orbital diagram for **16**, a model for

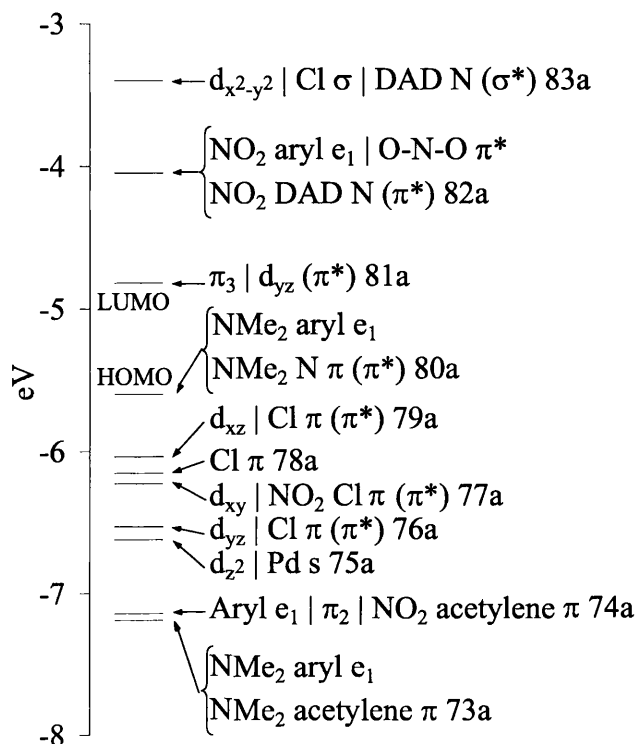


Figure 3.20: Molecular orbital energy level diagram for **16**.

15. It can be seen that **16** has one aryl-based orbital that has been destabilised by the dimethyl amino lone pair (the HOMO). This orbital is situated completely on the side of the molecule to which the dimethyl amino group is attached, and is of the same character as the HOMO in **8**, i.e. the e_1 level of the aryl ring and the π AO of the dimethyl amino nitrogen.

Computationally, the long wavelength band was found to be made up of two transitions at 736 and 667 nm. Of these, the transition at 736 nm is the most intense and was found to be due to the promotion of an electron from the HOMO (80a) to the LUMO (81a, 69%). The HOMO is, as mentioned earlier, located on the electron-rich amine half of the molecule and the LUMO, just as in **4**, **8** and **12**, is of DAD π_3 and d_{yz} character. The lower intensity transition is made up of a number

of transitions, the biggest of which (47%) is a transition from the HOMO-1 (79a) to the LUMO (81a). The HOMO-1 is of d_{xz} and Cl p_π character.

Three transitions at 441, 406 and 353 nm are equated to the band found experimentally at 415 nm. The transitions at 441 nm and 353 nm have the LUMO as the finishing orbital with the former having the HOMO-4 (76a) and the latter having the HOMO-7 (73a) as starting orbitals. The HOMO-4 is of d_{yz} and Cl p_π character. The HOMO-7 is located on the dimethyl amino molecular half of the molecule and is made up of the e_1 level of the aryl ring and the acetylenic π bonding level. The transition at 406 nm is, once more, a transition starting with the HOMO (80a) but finishing with the LUMO+2 (83a). The LUMO+2 was found to be of the same character as the LUMO+1 in the previously discussed complexes, i.e. $d_{x^2-y^2}$, Cl σ and DAD N p , but with no O-N-O π^* character. The high energy band found experimentally at 257 and 228 nm, was found computationally at 290 and 242 nm. Several, almost isoenergetic transitions, are also present but are of lower intensity. The transitions at 290 and 242 nm are due to $d_{xz}/\text{Cl } p_\pi$ to DAD $\pi_4/\text{acetylene } \pi^*$ and $d_{yz}/\text{Cl } \pi$ to DAD $\pi_4/\text{acetylene } \pi^*$ respectively.

The HOMO \rightarrow LUMO transition, found at 688 nm in the corresponding ligand (**14**), was also found in **16** (not shown in table 3.17 due to its extremely low intensity of 0.0015) at 597 nm but is now a HOMO \rightarrow LUMO+1 transition. The reason for the hypsochromic shift is that the energy of the receiving orbital is almost unaffected when going from **14** to **16**, with only a slight destabilisation in energy (+0.14 eV). The energy of the starting orbital, on the other hand, is stabilised in the complex relative to the free ligand (-0.37 eV). This results in a higher energy transition in **16** than in **14**. In all spectra, it is seen that the higher the energy of the transition, the more underestimated the intensity is. This might be the reason for the comparatively

high intensity of this transition in **14** and the low intensity of the transition in **16**.

3.5.8 Further Studies of Electronic Excitation Energies in Diazabutadiene Palladium Complexes

From the four molecular diagrams discussed in the previous sections (figure 3.13, 3.16, 3.19 and 3.20), some general conclusions can be drawn about the nature of the highest occupied orbitals in **4**, **8**, **12** and **16**. Figure 3.21 presents a summary of MO diagrams for these compounds. All complexes have five orbitals that are centred at the palladium and the chlorines. Each compound also has four orbitals made up predominantly of the e_1 level of the aryl rings. If the substituent in the para position of the aryl rings has a lone pair that can interact in an antibonding manner with the aryl π -system (as in the case for **8** and **16**), one of the four aryl-centred orbitals is destabilised to a higher energy. In **8**, which has two such substituents, two of the aryl-centred orbitals are destabilised to the point at which they become the HOMO and the HOMO-1. **16** only has one such substituent with a lone pair and therefore only one aryl orbital is destabilised significantly. The NO_2 substituent, having no N-based lone pair to interact with the aryl π system, has an orbital that is based solely on the substituent. **12** has two such substituents and has two orbitals made up of the O π AOs, whereas **16** has one and therefore only has one orbital of O π character.

All compounds have a transition from the highest aryl-centred orbital to the LUMO. This transition is, in all but one compound (**12**), the lowest energy transition of significant intensity. It would therefore seem that in order to construct a chromophore with a low energy absorption band, one has to find a substituent that can antibond with the aryl π -system so that the energy of that orbital becomes as

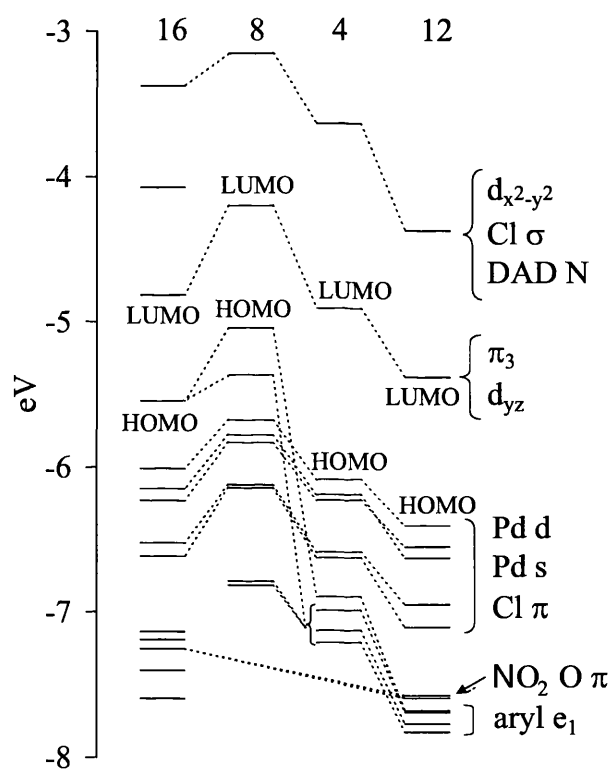


Figure 3.21: Molecular orbital energy level diagrams for 4, 8, 12 and 16.

high (least negative) as possible. An atom or group with lone pairs out of the aryl plane would seem to be the obvious choice. To further investigate this, calculations of a complex with two chlorine substituents in the *para* positions of the aryl rings were carried out as well as calculations of a complex with two fluorine substituents. It should be noted that no full investigation of the potential energy curve was done; the aryl rings were set to rotate freely and the geometry obtained from this was used to calculate the transition energies. Neither F or Cl destabilise the two orbitals of aryl e_1 character to the same extent as NMe_2 . They are only destabilised to become the HOMO-3 and the HOMO-5 as opposed to in **8** where they are destabilised to become the HOMO and the HOMO-1. As a result, the lowest transition in both halogen complexes that is of significant intensity, is found to be a transition from the HOMO-3 to the LUMO. Table 3.18 shows the wavelengths, energies and oscillator strength of the lowest energy transition of significant intensity in complexes with H (**4**), NMe_2 (**8**), F and Cl substituents. As can be seen, both fluorine and chlorine cause a bathochromic shift (98 nm and 112 nm) of the long wavelength transition compared to the unsubstituted complex (**4**) but are hypsochromically shifted relative to **8** (by 182 nm and 168 nm). Neither of the halogens gives rise to a transition of higher intensity than the intensity calculated for **8**. The long wavelength transition in the chlorine-substituted complex is of lower energy than the corresponding transition in the fluorine-substituted complex. This can be attributed to the orbital composition of the starting orbital (HOMO-3), in which it is seen that there is less F π character in the orbital in the fluorine complex than there is Cl π character in the orbital in the chlorine complex and thus less destabilisation occurs. It should also be noted that chlorine is a better π donor than fluorine.

Figure 3.22 shows the changes in the MO energies between the unsubstituted

Table 3.18: Calculated wavelength (nm), energies (eV) and oscillator strengths for H, NMe₂, F and Cl substituted complexes (adjusted by equation 3.1).

Substituent	λ (Energy)	Osc. St.
H (4)	417(2.97)	0.12
NMe ₂ (8)	697(1.78)	0.25
F	515(2.40)	0.03
Cl	529(2.34)	0.08

diazabutadiene (**2**), the dimethyl amino substituted diazabutadiene (**4**) and their palladium complexes (**4** and **8**). It can be seen that the occupied orbitals in **2** are destabilised when adding the dimethyl amino substituent (**6**). When complexing **6** with palladium dichloride (**8**), the most significant energy difference occurs in the LUMO, which becomes lower in energy than in either **2** or **6**. This stabilisation of the LUMO with respect to the free ligand is also observed in **4**. It should be noted that the LUMO in the complexes is not of the same character as the LUMO of the free ligands; the complexes' LUMOs feature a Pd d_{yz} contribution as well as the DAD π_3 that makes up the LUMO in the free ligands. Figure 3.22 strongly suggests that both the dimethyl amino substituent and the palladium are necessary to obtain a low energy transition in the NIR region.

Another question may be asked; is the acetylene moiety necessary to obtain a low energy transition such as the one present in **7**? The orbitals involved in the transition have, as can be seen in figure 3.18(a) and figure 3.18(b) (page 77), little contribution from the acetylenic AOs. A geometry optimisation and a transition energy calculation of a complex, in which the acetylene has been replaced by hydrogen, and with NMe₂ in the para position of the aryl rings, was carried out. The aryl rings were allowed to rotate freely and a minimum with the aryl rings at the

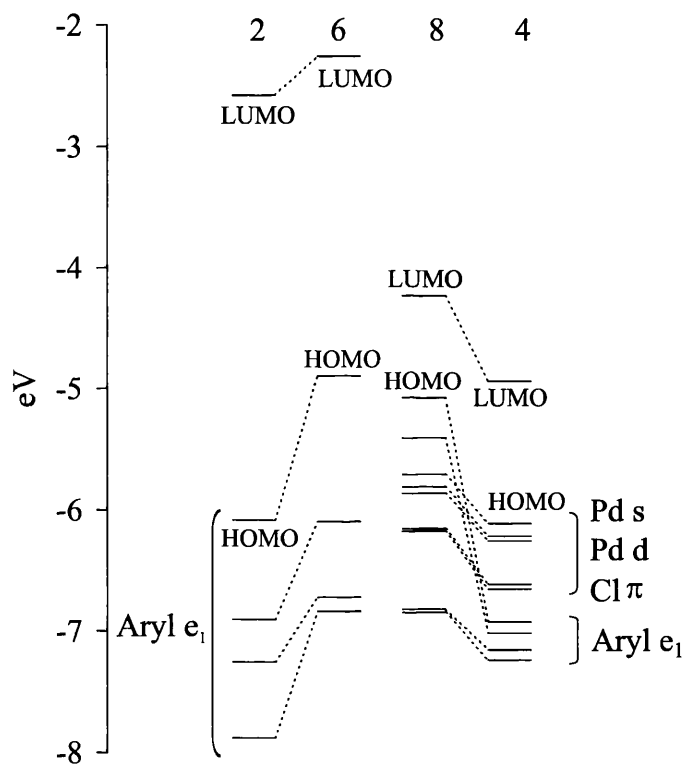


Figure 3.22: Molecular orbital energy level diagrams for **2**, **6**, **4** and **8**

exact same angle (47°) as in **8** was found. The low energy band was found to be shifted hypsochromically by 61 nm to 636 nm, as compared to 697 nm in **8**. This suggests that the small contribution of the acetylenes to the LUMO of **8** results in a shift of the longest wavelength band in the absorption spectrum and, together with the synthetic advantages (see section 3.1), indicates that the acetylenic groups are desirable in generating NIR chromophores.

3.5.9 Solvent Dependence of **7**

7 was synthesised according to literature procedures³⁵ and the UV-spectra in different solvents were recorded. The long wavelength transition in **7** was found to be sensitive to the choice of solvent. Figure 3.23 shows the shift observed when recording the absorption spectra in solvents of different dielectric constants. To see how well ADF could reproduce this shift, the electronic absorption spectrum for **8** was calculated in diethyl ether and in acetone. The results were compared with those discussed earlier that were carried out in DCM and are gathered in table 3.19.

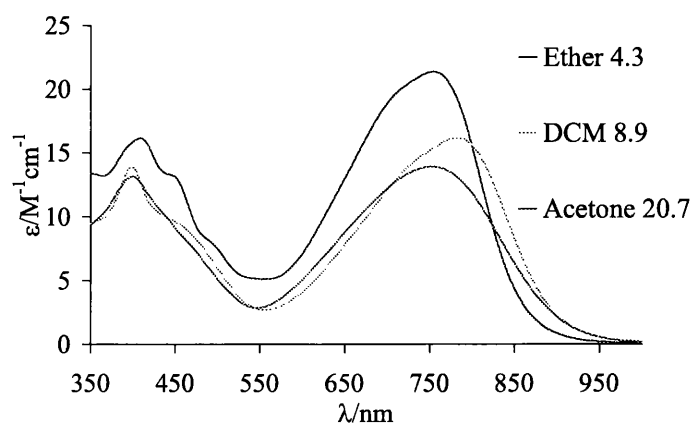


Figure 3.23: Absorption spectra for **7** in different solvents. The dielectric constant is given next to the solvent.

Experimentally a shift of 27 nm, from 754 nm to 781 nm, was observed when

Table 3.19: Calculated and experimental wavelength (nm) and energies (eV) for the low energy transition in **8** in different solvents (adjusted by equation 3.1).

Solvent (Dielectric const.)	λ_{exp} (Energy)	λ_{calc} (Energy)
Ether($\epsilon=4.3$)	754(1.64)	692(1.79)
DCM($\epsilon=8.9$)	781(1.59)	697(1.78)
Acetone($\epsilon=20.7$)	752(1.65)	708(1.75)

exchanging diethyl ether ($\epsilon=4.3$) for DCM ($\epsilon=8.9$). Computationally this shift is significantly underestimated and a shift of only 5 nm (692 nm to 697 nm) is observed. In the experimental spectrum, the long wavelength band in acetone ($\epsilon=20.7$), is shifted to shorter wavelength (752 nm) compared to the spectrum recorded in diethyl ether and DCM. Unfortunately the calculation carried out in acetone results in a shift to a longer wavelength (708 nm).

There are some possible explanations as to why the calculated energies do not reproduce the shifts observed experimentally; the experimental shifts are small and as observed for previously discussed compounds, the calculated energies are somewhat different from the experimental values even after being altered by equation 3.1. The discrepancies are usually larger than the experimental shift caused by the solvent. Additionally, COSMO may not be able to calculate such small effects as those observed here.

When including a solvent using COSMO there are, as discussed in chapter 3.2.3, different methods of how the solvent radius is calculated. The results presented so far were all carried out with a solvent whose radius has been calculated using the central atom (C in DCM, O in diethyl ether and $C_{C=O}$ in acetone) as the centre of the sphere. An alternative way to calculate the radii is by using the centre of mass

as the centre instead of the central atom.

To establish what effect these different methods of calculating the solvent radii have on the palladium complexes discussed here, a geometry optimisation of **8** was carried out using the centre-of-mass method to establish the solvent radius of DCM. The radius used previously is 3.58 Å and the radius when using the centre of mass method is 3.09 Å. The somewhat shorter radius was found to make no significant difference to the geometry of **8** and an energy minimum equal to the previous minimum was found. A calculation of excitation energies was carried out and as with the geometry, no significant differences were observed. Thus it can only be concluded that the COSMO approach in ADF can not adequately reproduce the small shifts observed due to changing solvent.

3.5.10 Conclusions

It has been previously observed experimentally that it is possible to tune the energy of the longest wavelength in the UV/Vis absorption spectra of DAD molecules by, for example, *para* substitution of the aryl rings and/or complexation to metal dichloride units. The computational work presented in this thesis provides a rationalisation for these observations, and makes direct connections between the electronic structures of the DADs (and their complexes) and their electronic absorption spectra. Thus, *para* substituents on the aryl rings with a lone pair which can interact with the aryl π system, destabilise one aryl-based MO per substituent present. The strongly electron-donating Me₂N substituent destabilises these orbitals to the extent that they become the HOMO (and HOMO-1 if two substituents are present). Halogens, such as F and Cl, do not destabilise these orbitals to the same extent as Me₂N.

Complexation with palladium causes the LUMO to be stabilised due to interac-

tion between the Pd d_{yz} and the DAD π_3 . The result of the stabilised LUMO and the destabilised HOMO (or HOMO-x depending on the substituent) is a significantly smaller HOMO-LUMO gap and thus a bathochromically shifted low energy transition.

The role of the acetylenic substituents on the DAD backbone has not been investigated as extensively as those of the palladium and dimethyl amino groups, but the calculations suggests that they also have a role to play, it is therefore clear that the empirical observation that the best NIR chromophores which can be obtained from this type of DAD system require (a) NMe_2 substitution of the *para* position of the aryl rings, (b) complexation to PdCl_2 and (c) acetylenic substitution of the DAD backbone, has a firm basis in the electronic structure of the compounds.

Chapter 4

The Strength of the X_2 Bond; $X=F, Cl, Br, I$

4.1 Introduction

It is well known that the bond energy of F_2 is significantly less than would be expected from extrapolation of the I_2 , Br_2 and Cl_2 values (I_2 : -149kJ/mol, Br_2 : -190, Cl_2 : -239, F_2 : -154).⁴⁹ Indeed, the F-F bond is one of the weakest of all covalent bonds. This anomaly has prompted numerous studies going back to the middle of the last century and includes contributions from chemists such as Pitzer, Pauling, Coulson and Mulliken.

In 1955, Pitzer proposed that London (dispersion) attractive forces between the nonbonding electrons might significantly contribute to the bonding energy in the X_2 family.⁵⁰ These forces can be seen as being due to electrons in the outer region of an atom or a molecule moving around so that there is an instantaneous dipole. This then affects the electrons on the other atom and thus gives rise to a weak bond. The

London formula is written as

$$-E_L = -\frac{3}{4} \frac{\alpha^2 h\nu}{R^6} \quad (4.1)$$

where α is the polarisability, R is the separation and $h\nu$ can be approximated by the ionisation potential. Table 4.1 shows that according to Pitzer, the London term accounts for approximately 35% of the bond energy for Cl_2 whereas it only has a small contribution to the bond energy for F_2 (c. 10%). By subtracting this term from the total bond energy, the anomaly of the bond energy of F_2 is reduced significantly.

Table 4.1: The effect of the London dispersive energy (E_L) on the dissociation energy (D_0) of the X_2 molecules according to two different studies. Energies in kJ/mol.

	Pitzer			Caldow and Coulson		
	D_0	E_L	$D_0 - E_L$	D_0	E_L	$D_0 - E_L$
F_2	163	17	146	158	6	152
Cl_2	239	84	155	239	16	223
Br_2	189	71	118	190	45	145
I_2	149	54	95	149	-	-

Some years later, Caldow and Coulson came to a different conclusion by using different polarisabilities and ionisation potentials than Pitzer.⁵¹ Caldow and Coulson's results are presented together with Pitzer's results in table 4.1 and it can be seen that according to Caldow and Coulson the dispersion effect is much less significant and can only account for a small part of the anomaly observed in F_2 .

Also in 1955, Mulliken invoked the idea of hybridisation to explain why Cl_2 has a stronger bond than F_2 .⁵² Specifically 'the greater strength of the "single" bond in Cl_2 can be understood as a consequence of pronounced partial multiple bond

character made possible by d hybridisation'. Thus, Mulliken suggests that F_2 is not anomalously weak but Cl_2 is anomalously strong.

Pauling shared Mulliken's view that hybridisation is important but for a different reason.⁵³ He stated that the reason for di-fluorine's low bonding energy is due to destabilising interactions between unshared electron pairs on the separate atoms. This destabilising effect is decreased by hybridisation and the heavier halogens will have more pronounced d-hybridisation than fluorine and thus be less destabilised by the electron pairs.

In 1962 Caldow and Coulson calculated the Coulomb energies of X_2 , which showed the same trends as seen in their bond energies.⁵¹ The anomaly in F_2 compared to Cl_2 , Br_2 and I_2 was traced to all three electrostatic energy contributors (electron-electron and nucleus-nucleus repulsion, and nucleus-electron attraction). These terms are all heavily dependent on the interatomic distance and Caldow and Coulson suggested that the fluorine atoms would prefer to be closer together (there is a small σ - σ overlap in F_2) but are prevented from this due to some repulsive force.

In 1983 Jolly and Eyermann showed for the first time that F_2 experiences lone pair/lone pair repulsion, whereas no such repulsion could be found in Cl_2 , Br_2 and I_2 .⁵⁴ They used photoelectron spectroscopy data to calculate localised ionisation potentials (LOIPs), i.e. the energies that atomic orbitals (in molecules) would have if they were non-bonding. These LOIPs were then compared with the ionisation potentials of the valence π and π^* molecular orbitals. Consequently, Jolly and Eyermann came to the conclusion that the anomalies observed for F_2 can, at least to some extent, be explained by lone pair repulsion.

Most modern inorganic chemistry textbooks favour the lone pair/lone pair repulsion argument of Jolly and Eyermann, Pauling and, implicitly, Caldow and

Coulson.^{55,56}

This work presents the results of my own investigation into the bond energy of the diatomic halogens F_2 , Cl_2 , Br_2 and I_2 . Modern density functional theory has been used to probe the electronic structure of the molecules as a function of internuclear separation, and the bond energy has been broken down into chemically useful components using the energy decomposition scheme developed by Ziegler and Rauk (see section 1.8.2).^{31,32} The aims were two-fold; to see how the previous explanations of the weakness of the F_2 bond stand up to modern quantum chemical analysis and ultimately to find why the F_2 bond is so weak. It should be noted that there have been many other quantum chemical studies of F_2 , which are discussed later in this chapter, although I am aware of only one using the present methodology. This work, currently in press is by Esterhuysen and Frenking, and is discussed after the presentation of my results. My study has already been published (see reference 57).

4.2 Determining the Most Suitable Computational Parameters

4.2.1 Exchange-Correlation Functional

The initial aim of this study was to determine the most suitable parameters, e.g. basis set and XC-functional, for calculating the bond energy in the diatomic halogen molecules as well as other key data such as bond lengths and vibrational frequencies. There have been many attempts in the literature to accurately calculate the bond energy of these molecules using many different methods, and success has been mixed. Table 4.2 summarises some of the data found in the literature together with some results from this study. These have been obtained using DFT, as implemented in the ADF program, together with a number of *ab initio* and DFT calculations using the Gaussian98 program.

(a) ***Ab initio* methods** It can be seen that Hartree-Fock (HF) predicts the two fluorine atoms to be unbound by 114 kJ/mol when employing the cc-pVQZ basis set⁵⁸ and by 164 kJ/mol when employing the 6-311+G(df) basis set. HF also gives the weakest bonds for Cl₂ and Br₂. HF usually underbinds molecules as no electron correlation is taken into account but the poor agreement with experimental data for F₂ is exceptionally poor. Indeed, it has been known for the past 40 years that Hartree-Fock is unable to give a correct potential energy curve for F₂.^{67,68} It was later found that the lowest unoccupied orbital, $3\sigma_u$, plays a significant role in the binding and the calculated bond energy is significantly improved by using a two-determinantal wave function consisting of both the Hartree-Fock determinant and the $(3\sigma_g^2) \rightarrow (3\sigma_u^2)$ determinant.⁶⁹⁻⁷¹ However, the calculated bond energy was still

Table 4.2: Bond energies (kJ/mol) for the diatomic halogen molecules. No zero point energies (ZPE) are included unless stated.

Method	Basis set	F ₂	Cl ₂	Br ₂	I ₂
Experimental ⁴⁹ E		-154	-239	-190	-149
<i>Ab initio</i>					
HF ⁵⁸	cc-pVQZ	114			
HF	6-311+G(df)	164	-57	-62	
MRCISD-6 ⁵⁹	5s4p2d1f	-152			
MP2	6-311+G(df)	-149	-210	-201	
G2(MP2,SVP) ⁶⁰	6-31G(d)	-153	-244		
G2(MP2,SVP) ⁶¹	6-311+G(3df,2p)			-182	
CCSD(T) ⁶²	cc-pVQZ	-154			
CCSD(T) ⁶³	cc-pVQZ		-234		
CCSD(T)	6-311+G(df)	-116	-203	-192	
CASSCF+1+2 ⁵⁸	cc-pVQZ	-142			
DFT					
X-only/PW91x/PBEc/ZORA	QZ4P(STO)	-237	-253	-215	-187
X-only/PW91x/PBEc/ZORA/ spin-orbit	QZ4P(STO)	-233	-244	-186	-135
X-only/PW91x/PBEc/ZORA/ spin-orbit/ZPE	QZ4P(STO)	-227	-241	-184	-134
PBE(local part only) ⁶⁴	TZ2P(GTO)	-327	-347		
PBE ⁶⁴	TZ2P(GTO)	-223	-272		
Meta-GGA(PBE) ⁶⁴	TZ2P(GTO)	-181	-249		
BLYP/ZORA	QZ4P(STO)	-258	-257	-217	-187
BLYP	6-311+G(df)	-185	-219	-211	
BLYP ⁶⁵	6-311G(d)	-208			
BLYP ⁶¹	6-311+G(3df)/ MP2(fu)/6-31G(d)			-183	
Hybrid DFT					
B3LYP	6-311+G(df)	-133	-206	-200	
B3LYP ⁶⁶	TZ2P(GTO)	-146	-217		
B3LYP ⁶¹	6-311+G(3df)/ MP2(fu)/6-31G(d)			-173	

not satisfactory and in 1981 Blomberg and Siegbahn⁵⁹ published a paper which showed that the inclusion of the $2\pi_u$ in the reference space further improves the bond energy. A six-reference wave function containing configurations $(3\sigma_g)\rightarrow(3\sigma_u)$ and $(3\sigma_g)(1\pi_u)\rightarrow(3\sigma_u)(2\pi_u)$ was found to be necessary to give a reliable result. Also, it was found that a basis set including f functions is needed and dynamic electron correlation has to be properly described. A brief summary of calculations striving to accurately reproduce the bond energy of F_2 has recently been given by Pittner et al.⁷² This paper states that single-reference methods such as MP2 and CCSD(T) might give reasonable bond energies (see table 4.2 and below) but the potential energy curve begins to deviate from a realistic potential curve deduced from experiment at $r=2.3 \text{ \AA}$.

Inclusion of correlation through second order Møller-Plesset (MP2) theory gives satisfactory results for F_2 , as well as Cl_2 and Br_2 . Both the Coupled Cluster (CCSD(T)) method^{62,63} and the Complete Active Space Self-Consistent Field (CAS-SCF) method⁵⁸ in conjunction with cc-pVDZ also yield bond energies close to the experimentally recorded energies.

(b) DFT methods Even though Density Functional Theory (DFT) in some ways accounts for electron correlation, using the simplest forms of DFT, i.e. the Local Density Approximation (LDA), the molecular binding energy is significantly overestimated. This can be seen in table 4.2 where the local part of Perdew, Burke and Ernzerhof's PBE functional⁶⁴ predicts the bond energy of F_2 and Cl_2 to be 173 and 108 kJ/mol greater than the respective experimentally recorded values. Moving to the gradient corrected part of the PBE functional, or using Becke's 1988 exchange corrections in combination with Lee, Yang and Parr's (BLYP) corrects for this over-

estimation to some extent but the bond energies for F_2 and Cl_2 are still too large. Applying the 6-311G(d) basis set with BLYP⁶⁵ to F_2 gave slightly poorer values than using the 6-311+G(df) basis set. The QZ4P STO basis set results in an even more overestimated bond energy for F_2 than the GTO basis sets. This is a general trend in the halogen series even though the difference between the two types of basis sets becomes smaller for the heavier halogens. The bond energy for Br_2 can be calculated very accurately using BLYP and the GTO 6-311+G(3df) basis set at the MP2/6-31G(d) optimised geometry,⁶¹ whereas direct GTO 6-311+G(df) or STO QZ4P overestimates the energy.

The best results for the bond energy in the halogen series are achieved by using hybrid DFT functionals such as B3LYP. B3LYP is especially good at estimating the bond energy for F_2 , which is the diatomic halogen where most of the other methods do worst. The meta functional based on Perdew, Burke and Ernzerhof's functional⁶⁴ also performs well and gives much more accurate bond energies than the corresponding gradient corrected functional. Unfortunately, the Amsterdam Density Functional (ADF) program, which has been used throughout the work presented here, does not support hybrid DFT functionals, and meta-GGA functionals can only be employed in single point calculations.

The reason for using the ADF program is to give access to the energy decomposition scheme described in section 1.8.2. Limitations of the ADF program mean that pure DFT methods and STO basis sets have to be applied even though the data in table 4.2 indicate that more accurate bond energies could be obtained by using hybrid DFT functionals instead of pure DFT functionals or applying GTO basis sets instead of STO basis sets.

The ADF program offers a wide range of XC-functionals. To find a suitable

LDA description, pure Slater exchange (X-only, $\alpha = 2/3$) and the parameterisation of Vosko, Wilk and Nusair (VWN) which includes some electron correlation were used. Unless otherwise stated, the QZ4P basis set was used with relativistic effects taken into account through ZORA. Neither spin-orbit coupling nor zero-point energy are included. The tendency for DFT to overestimate the correlation results in VWN giving a larger bond energy than X-only by 35-45 kJ/mol and is further away from the experimentally recorded energy. Therefore X-only was used for further studies unless otherwise stated. Figure 4.1 shows a few examples of the difference between using X-only or VWN as the local part of the XC-functional.

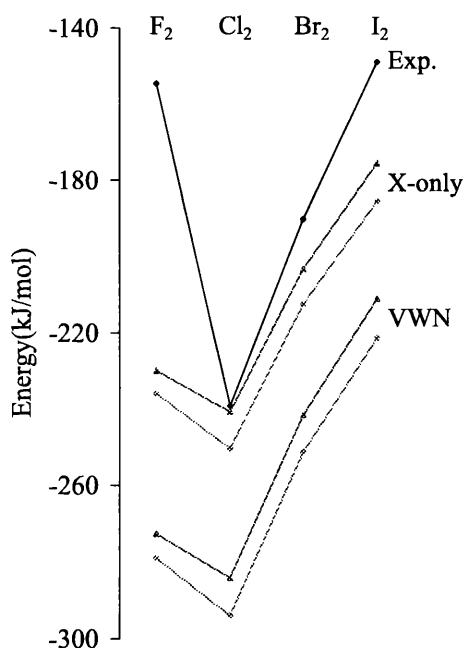


Figure 4.1: Difference between X-only and VWN as the LDA option using two common GGA functionals and the QZ4P basis set. Red=BP86, green=PW91.

The search for the most suitable gradient corrected functional turned out to be more difficult than that for the most suitable local functional. One of the key

experimental facts is that F_2 has a weaker bond than Cl_2 , and hence one way to determine which functional is best suited for this study is to look at the calculated difference in energy between F_2 and Cl_2 . Experimentally F_2 is 85 kJ/mol weaker than Cl_2 . Any combination with LYP as the GGA correlation functional resulted in F_2 being almost equal or greater in bond energy than Cl_2 . The same was found when PBE_{ex} was used as exchange functional with Perdew's 1986 or Perdew and Wang's 1991 correlation corrections. These combinations were therefore discarded and not considered for further studies. The other tested functionals (BP86, BPBE_c, BPW91_c, PW86xP86, PW86xPBE_c, PW86xPW91_c, PW91xP86, PW91xPBE_c and PW91) resulted in the bond energy of F_2 being 5-21 kJ/mol less negative than Cl_2 . Even though the calculated difference in bond energy between F_2 and Cl_2 was significantly smaller than the experimental value, the correct trend where F_2 is weaker than Cl_2 is reproduced.

From figure 4.2, which shows the bond energy obtained using the functionals that predict F_2 to be weaker than Cl_2 , it can be seen that the X-only LDA option with Becke's exchange correlation combined with any of the three correlation corrections (PW91_c, Perdew or PBE_c) gives a good estimation of the bond energy for Cl_2 but overestimates the energy for F_2 , Br_2 and I_2 . The best XC-functionals for Br_2 was found to be the X-only option PW86x⁵ with any of PW91_c, Perdew or PBE_c's correlation corrections. However, these combinations of functionals overestimate the energy of F_2 and I_2 and underestimate the energy for Cl_2 . Using PW91_x as the exchange functional causes overbinding for all of the molecules independent of the correlation corrections applied. However, all nine combinations seen in figure 4.2 were considered accurate enough for further studies.

Table 4.3 shows the calculated bond lengths that are obtained by employing

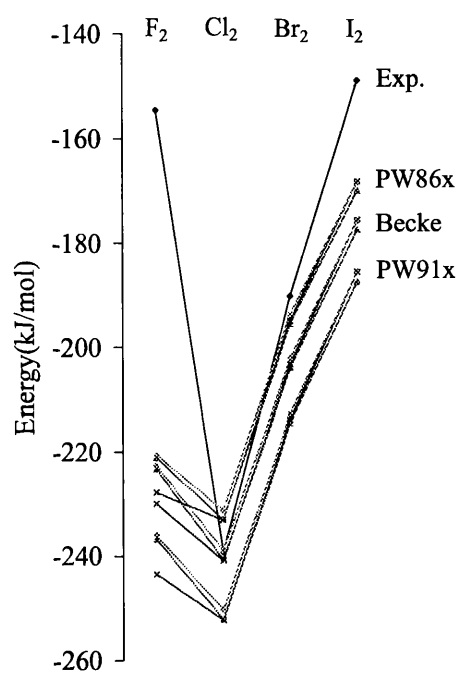


Figure 4.2: A selection of calculated bond energies for X₂ (X=F, Cl, Br, I) using different GGA functionals with X-only for the LDA part. Blue=Perdew, red=PBEC and green=PW91c.

Table 4.3: Selection of calculated bond lengths (\AA) using different XC-functionals.

X-only was used for the LDA part of the XC-functional.				
Exchange-correlation functional	F ₂	Cl ₂	Br ₂	I ₂
Experimental ⁴⁹	1.412	1.988	2.281	2.667
PW86x/PW91c	1.456	2.059	2.377	2.772
PW86x/Perdew	1.456	2.062	2.380	2.783
PW86x/PBEc	1.455	2.057	2.374	2.775
Becke/PW91c	1.438	2.045	2.350	2.741
Becke/Perdew	1.437	2.049	2.353	2.745
Becke/PBEc	1.436	2.043	2.347	2.738
PW91x/PW91c	1.436	2.043	2.346	2.737
PW91x/Perdew	1.435	2.046	2.349	2.740
PW91x/PBEc	1.434	2.040	2.343	2.732

the nine combinations of functionals discussed in the previous paragraph. It should be noted that using the VWN functional for the local part results in shorter bond lengths than the X-only option and therefore resulted in more accurate bond lengths. However, since the bond energy was so poorly represented using that functional, X-only was considered to be a better method for further studies.

Using the PW86x exchange functional results in the least accurate bond lengths for all discussed diatomic halogens regardless of the correlation functional employed. The best estimate of the bond lengths is obtained using the PW91x or Becke exchange functionals. The differences in the calculated bond lengths between these two exchange functionals are small, independent of which correlation functional is applied. Therefore, both of these exchange functionals were used in further studies together with the PW91c, PBEc and Perdew options for the correlation corrections, and the PW86 exchange functional was discarded and not considered further.

Table 4.4 shows the vibrational frequencies for the diatomic halogen molecules.

Table 4.4: Selection of calculated vibrational frequencies (cm^{-1}) using different XC-functionals. X-only was used for the LDA part of the XC-functional.

Exchange-correlation functional	F ₂	Cl ₂	Br ₂	I ₂
Experimental ⁴⁹	917	560	325	215
Becke/PW91c	947	505	296	198
Becke/Perdew	954	502	294	197
Becke/PBEc	951	507	297	199
PW91x/PW91c	954	508	298	199
PW91x/Perdew	959	505	296	198
PW91x/PBEc	958	511	299	200

Both of the considered exchange functionals, PW91x and Becke, result in vibrational frequencies that are too high for F₂ (by 30-42 cm^{-1}) and that are too low for Cl₂ (by 49-58 cm^{-1}), Br₂ (by 26-31 cm^{-1}) and I₂ (by 15-18 cm^{-1}). The best result for F₂ was obtained using a combination of Becke's exchange corrections and PW91c's correlation corrections whereas the most accurate frequencies for the other halogens (Cl₂, Br₂ and I₂) were obtained using the PW91x's exchange corrections and PBEc's correlation corrections. Given that no functional combination does a good job of calculating the bond energy for F₂, it was decided to go with the combination of functionals that best reproduced the bond energies, bond lengths and vibrational frequencies of the other diatomic halogens. Therefore the X-only/PW91x/PBEc combination was used for further calculations unless otherwise stated.

4.2.2 Basis Set

The all electron ZORA relativistic basis sets for the halogens which are available in the ADF program are double-zeta (DZ), triple-zeta plus one polarisation (TZP), triple-zeta plus two polarisations (TZ2P) and quadruple-zeta plus four po-

larisations (QZ4P). Table 4.5 shows the experimentally recorded X_2 bond energies and the calculated bond energies using these four different basis sets with the X-only/PW91x/PBEC functional. The only basis set that gives a good energy for F_2 is DZ, but this also results in the worst agreement for Cl_2 , Br_2 and I_2 and does not reproduce the general trend in bond energy ($Cl_2 < Br_2 < F_2 < I_2$). A much better agreement for all halogens but F_2 was given when employing a basis set that included at least one polarisation function (TZP). TZ2P and QZ4P gave very similar results, which would indicate that there is a basis set saturation at the TZ2P level. The best overall bond energy was obtained with the TZP basis set but, pre-empting the following section, it should be noted that, for the heavier molecules, spin-orbit coupling will make the bond energy less negative and thus cause a TZP basis set to underbind Br_2 and I_2 . It was therefore decided to use the QZ4P basis set, which are ‘intended for near basis set limit calculations on small systems’, according to the ADF User’s Guide.

Table 4.5: Bond energies (kJ/mol) obtained using different basis sets. No spin-orbit coupling was included.

Basis set	F_2	Cl_2	Br_2	I_2
Experimental ⁴⁹	-154	-239	-190	-149
QZ4P	-237	-252	-215	-187
TZ2P	-233	-251	-217	-188
TZP	-223	-236	-200	-152
DZ	-159	-141	-139	-120

4.2.3 Spin-Orbit Coupling

The inclusion of spin-orbit coupling will affect the heavy halogens more than the lighter halogens. Using the QZ4P basis set and different XC-functionals it was observed that the effect of including spin-orbit coupling at the already optimised geometry is only 3.3-3.8 kJ/mol for the bond energy of F₂, but 49.0-51.9 kJ/mol for the bond energy of I₂ (Note that these spin-orbit coupling results are derived from spin-orbit coupling calculations on both the X₂ molecules and the basic atom fragments). The corresponding values for Cl₂ and Br₂ are 7.5 and 26.4-28.9 kJ/mol. The bond energies of Cl₂, Br₂ and I₂ obtained for the two largest basis sets, QZ4P and TZ2P, are reduced and therefore improved by the inclusion of spin-orbit coupling. This is not the case for the TZP basis set, which gives better results without accounting for spin-orbit coupling.

It is currently only possible to implement spin-orbit coupling in single-point calculations, not in geometry optimisations. To investigate the effect of spin-orbit coupling on the geometries and the corresponding bond energies of the halogens, a series of single-point calculations (using the QZ4P basis set) was carried out close to the scalar geometry optimised minima. The bond lengths for the three lightest molecules, F₂-Br₂, were, more or less, unaffected by spin-orbit coupling. On the other hand, the bond length of I₂ was slightly longer (2.75-2.77 Å) than the one obtained from a normal geometry optimisation (2.73 Å) and therefore further away from the experimental value (2.67 Å). However, this change in geometry due to spin-orbit coupling gives rise to little or no difference in the bond energy.

4.2.4 Conclusions

The well-known problem of reproducing the bond energy in F_2 has once again proven to be difficult and the F_2 experimental energy is reproducible by the ADF code only at the cost of accuracy of the other halogen molecules. The QZ4P basis set combined with the X-only, PW91 exchange and PBE correlation functionals has given the best general fit to the bond energy, bond lengths and vibrational frequencies. Table 4.6 shows a summary of the results obtained with these parameters. The best values obtained for the bond energies (scalar geometry optim.+SOC s.p.+ZPE) leave F_2 overbound by 73 kJ/mol, but are very good for the heavier X_2 , and the abnormal trend in the bond energy of the halogens (i.e. that Cl_2 has a stronger bond than F_2) is reproduced. This is also found to be the case at the scalar geometry optimised level (F_2 : -237, Cl_2 : -252). Thus, both the DFT method and basis set were considered to be sufficiently reliable for further studies (especially the energy decomposition analysis) on this group of molecules and all further calculations were carried out using the above-mentioned parameters (the X-only, PW91 exchange and PBE correlation with the QZ4P basis set) without correcting for spin-orbit coupling or zero-point energy.

4.3 Population Analysis

One recurring explanation for the abnormally low bond energy in F_2 is, as has been mentioned earlier, that of d-orbital hybridisation effects. Both Mulliken⁵² and Pauling⁵³ stated that the small hybridisation in F_2 causes the repulsion effect of the lone pairs to be greater than in the more hybridised heavier molecules (see section 4.1). As table 4.7 shows, there is little hybridisation in any valence orbitals,

Table 4.6: Bond lengths, total bonding energies and frequencies calculated using the X-only/PW91x/PBEC functional and QZ4P basis set.

Bond lengths (Å)	F ₂	Cl ₂	Br ₂	I ₂
Experimental ⁴⁹	1.412	1.988	2.281	2.667
Scalar Geometry optim.	1.434	2.040	2.343	2.732
SOC optim.	1.42-1.44	2.04-2.05	2.34-2.36	2.75-2.77

Total Bonding Energy (kJ/mol)	F ₂	Cl ₂	Br ₂	I ₂
Experimental ⁴⁹	-154	-239	-190	-149
Scalar Geometry optim.	-237	-252	-215	-187
Scalar Geometry optim.+SOC s.p.	-233	-244	-186	-135
SOC optim.	-233	-244	-186	-136
Scalar Geometry optim.+ZPE	-231	-249	-213	-186
Scalar Geometry optim.+SOC s.p.+ZPE	-227	-241	-184	-134

Frequencies (cm ⁻¹)	F ₂	Cl ₂	Br ₂	I ₂
Experimental ⁴⁹	917	560	325	215
Geometry optim.	958	511	299	200

Table 4.7: % contribution to valence π_g , π_u and σ_g MOs. Minimum contribution

1%.				
MO	F ₂	Cl ₂	Br ₂	I ₂
π_g	99p	98.9p, 2.1d	99.2p, 1.7d	99.6p, 1.5d
π_u	99.4p	97.5p, 2.5d	98.2p, 1.8d	97.6p, 1.8d
σ_g	93.0p, 6.5s	91.4p, 8.0s, 1.2d	94.9p, 4.7s	94.6p, 4.4s

especially in π_g and π_u orbitals. It is thus extremely unlikely that the weak bond energy of F₂ is due primarily to hybridisation effects, although they might make a slight contribution to the observed abnormalities.

4.4 Energy Decomposition

ADF uses the the Ziegler-Rauk decomposition scheme (see section 1.8.2) to divide the bond energy into three major parts: the electrostatic energy (E^{elstat}), the Pauli repulsion energy (E^{Pauli}), and the orbital interaction energy (E^{oi}).

In order to gain some insight, not only into the different energy terms at the equilibrium bond distance but also into how they vary with the bond length, linear transit calculations were carried out at 0.01 Å intervals in $r(\text{X-X})$. Note that in a diatomic molecule a linear transit calculation as the sole geometric variable is effectively an automated series of single point calculations. Figure 4.3 shows the variation of the bonding energy and its component parts for F₂ as the bond length changes. E^{elstat} is negative and as $r(\text{X-X})$ shortens, E^{elstat} becomes increasingly stabilised. But at $r \sim 0.7$ Å the nucleus-nucleus repulsion begins to dominate and the electrostatic energy becomes more positive. The orbital interaction energy on the other hand is always negative and is more stabilised as the bond distance decreases.

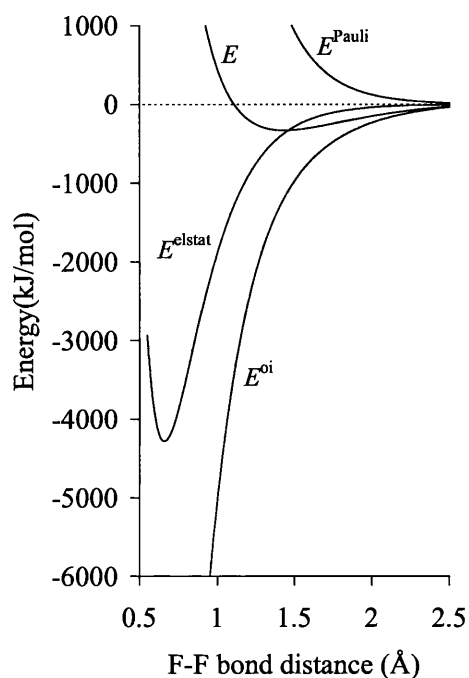
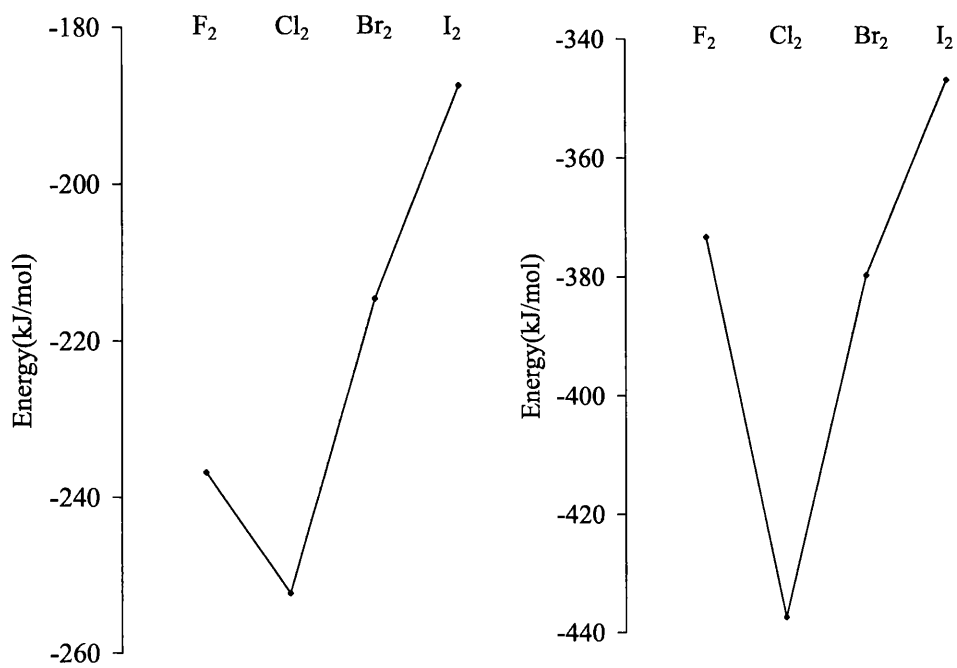


Figure 4.3: Decomposition of the bond energy, E , in F_2 when changing the F-F bond distance. E^{elstat} =electrostatic energy; E^{Pauli} =Pauli repulsion energy; E^{oi} =orbital interaction energy.

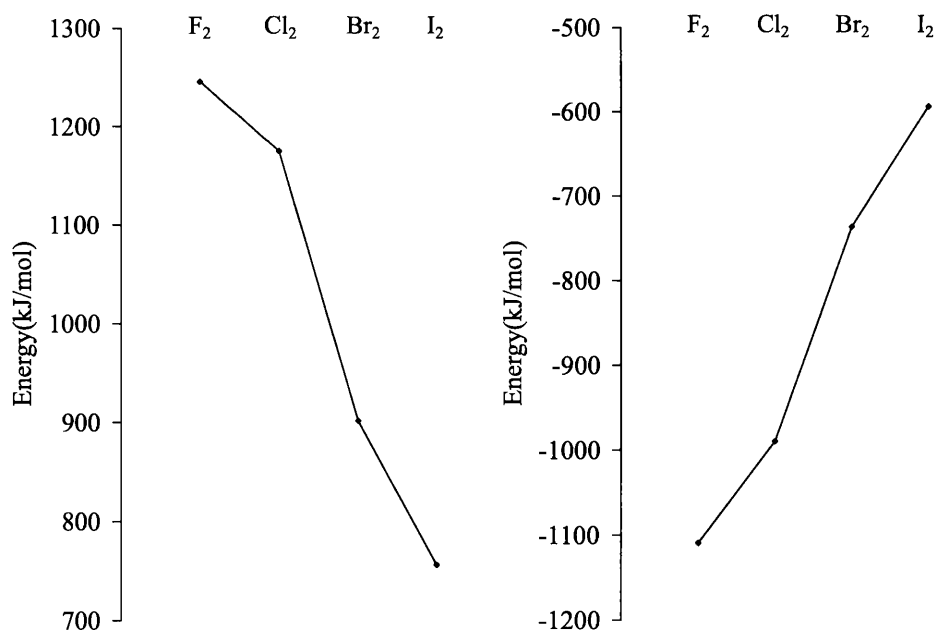
This is the opposite behaviour to the Pauli repulsion energy, which is always positive and becomes more repulsive as the bond distance decreases. The result of all these energy terms is the total bonding energy, E , which is quite small in comparison to the individual terms. As seen in figure 4.3, E changes from zero, at long bond distances, to a minimum at the equilibrium bond distance, and then becomes destabilised at shorter bond distances. These energy trends in the total energy and its component terms are the same for all diatomic halogen molecules.

Figure 4.4 shows the bond energies and its component terms for all four investigated halogen molecules at their equilibrium bond distances. It can be seen that the electrostatic energy mirrors the trend in the total bond energy when going from F_2 to I_2 . Indeed, it is the only energy term which does not show an almost lin-



(a) Bond Energy

(b) Electrostatic Energy



(c) Pauli Repulsion Energy

(d) Orbital Interaction Energy

Figure 4.4: Energy decomposition analysis terms at equilibrium bond distance.

ear trend along the halogen series. This suggests that the origin of the weak F-F bond lies within the electrostatic energy. This is in agreement with the findings of Caldow and Coulson⁵¹(see section 4.1) who suggested that the unusually weak F-F bond comes from abnormalities in all three electrostatic terms (Q_{ee} , Q_{nn} and Q_{en}). Unfortunately, to the best of our knowledge, it is not possible to extract the individual contributions to E^{elstat} from the ADF program. However, the nucleus-nucleus repulsion can be easily obtained using equation 4.2.

$$\Delta V_{\text{nn}} = \sum \frac{Z_{\alpha}Z_{\beta}}{R_{\alpha\beta}} \quad (4.2)$$

Contrary to what Caldow and Coulson found, the calculation using equation 4.2 results in a steady increase in the nucleus-nucleus repulsion when going from F₂ to I₂. This difference is due to electron screening. Whereas I did not take any electron screening into account Caldow and Coulson incorporated it in their calculation by using the effective nuclei charge, Z_{eff} . Since the present calculated trend in nucleus-nucleus repulsion shows no anomalies, it was believed that the deviation in the electrostatic energy lay in one of the other two terms. It is known that when the densities ρ_{α} and ρ_{β} approach each other and begin to overlap, the electron-electron repulsion term will decrease and at very short bond distances it is more or less insignificant.³⁰ The AO overlap matrix has been calculated and table 4.8 shows the sum of all the overlaps between the two halogen atoms. It is clear that both the electrostatic energy and the total overlap follow approximately the same trend, in which Cl₂ has the largest absolute value. This is consistent with the idea that the electron-electron repulsion is larger than would be expected for F₂ since the atom/atom overlap is not as large as the Cl₂-I₂ trend would indicate. This increase in electron/electron repulsion accounts for the reduction in E^{elstat} from Cl₂ to F₂.

Table 4.8: Sum of all overlaps in the S -matrix and the electrostatic energy for F_2 , Cl_2 , Br_2 and I_2 at their equilibrium bond distance.

	F_2	Cl_2	Br_2	I_2
S	11.1	13.4	11.3	11.5
E^{elstat}	-373	-438	-380	-347

If the small total overlap is the reason for the abnormally low bond energy in F_2 , one might ask why is the bond length not shorter. This would then increase the overlap and, as shown in figure 4.3, would give a more negative electrostatic energy.

If we for a moment leave the halogens and instead look at the neighbouring chalcogen series in which no abnormalities in the bond energy trend are seen, we might get some answers to our question. Table 4.9 shows the optimised bond lengths and the electrostatic energy for the first three diatomic molecules in the chalcogen series and the halogen series. The difference in bond length between Cl_2 and S_2 and between Br_2 and Se_2 is approximately 0.1 Å, whereas the difference between F_2 and O_2 is 0.19 Å. Looking at it from a simplistic viewpoint, one can say that going from the diatomic chalcogen molecules to the corresponding halogen molecule will give an increase in the bond distance of 0.1 Å. The ‘extra’ 0.09 Å increase that F_2 experiences must be due to something else. If the F-F bond were 0.09 Å shorter, i.e. 1.34 Å, the electrostatic energy would be -531 kJ/mol (see table 4.10) and thus follow the same trend as the other halogens; the heavier the halogen the less negative the electrostatic energy. Thus, there must be something in the Pauli repulsion energy or the orbital interaction energy that causes the equilibrium bond length to be at the longer, less-electrostatic-advantageous, value.

Table 4.10 shows the changes in the energy decomposition analysis terms for F_2 when going from the equilibrium bond length (1.43 Å) to 1.34 Å. It can be seen that

Table 4.9: Optimised bond distance r (Å) and electrostatic energy (kJ/mol) for the first three diatomic molecules in the chalcogen series and the halogen series.

	F ₂	Cl ₂	Br ₂	O ₂	S ₂	Se ₂
E^{elstat}	-373	-438	-380	-904	-691	-581
r	1.43	2.04	2.34	1.24	1.94	2.23

Table 4.10: Energy decomposition of the bond energy (kJ/mol) for F₂ at different bond distances.

	E	E^{elstat}	E^{Pauli}	E^{oi}
$r=1.43$	-331	-373	1246	-1203
$r=1.34$	-314	-531	1805	-1588
Δ	+17	-158	+559	-385

the largest change with decreasing the bond length occurs in E^{Pauli} . This change is destabilising and results in a less negative bond energy of the F₂ molecule when decreasing the bond length.

Bickelhaupt and Baerends note that the overlap of the separate fragments strongly affects the kinetic energy component of the Pauli repulsion energy.³⁰ As it is this component that is responsible for the overall destabilisation in the exchange repulsion as the bond length is shortened, the total Pauli repulsion energy becomes more repulsive the more the fragments overlap. Figure 4.5 shows the Pauli repulsion energy together with the total X/X overlap as a function of the bond distance. It can be seen that the change in overlap as a function of the bond distance over the r scale used is greatest in F₂ (black solid line). As a result, the total Pauli repulsion energy as a function of the bond distance also changes most rapidly in F₂. This is presumably a result of the compact nature of the F atom. This steep increase in

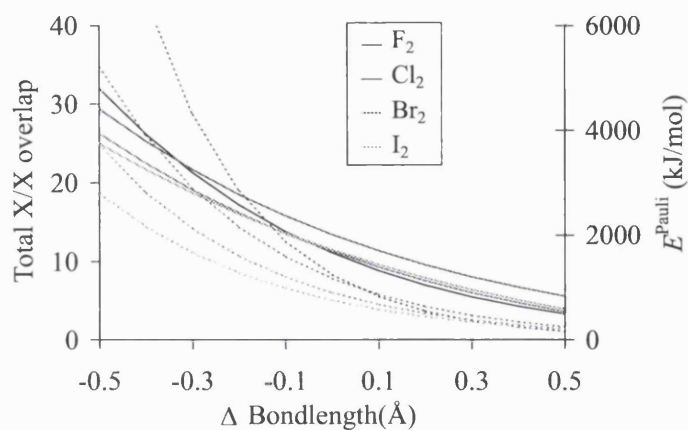


Figure 4.5: Pauli repulsion energy (hashed line) and total overlap (solid line) as a function of change in bond length from r_{eqm} .

overlap and thus in the Pauli repulsion energy causes an energy wall that prohibits the F-F bond distance from being any shorter than 1.43 Å and consequently the F₂ bond is weaker than expected.

4.5 Conclusions

In this study a detailed discussion of how modern density functional methods address the weakness of the F₂ bond has been presented. The bond energy and its electrostatic, Pauli and orbital contributions have been investigated as a function of $r(\text{X-X})$ using the Ziegler-Rauk scheme. The main conclusions are as follows:

1. There is little evidence that hybridisation of d-orbitals contributes significantly to the abnormalities seen in the bond energy in the halogen series.
2. At the optimised bond distance, E^{Pauli} and E^{oi} show an almost linear trend from I₂→F₂ whereas E^{elstat} mimics the bond energy (F₂<Cl₂>Br₂>I₂). E^{elstat} of F₂ is approximately 125 kJ/mol weaker than would be expected on extrapolation of the I₂→Cl₂ data and hence suggests that the weakness in the bond energy lies here. It is suggested that the unexpected low value of E^{elstat} for F₂ arises from larger electron-electron repulsion at r_{eqm} compared to the heavier dihalogens.
3. The surprisingly small value of E^{elstat} for F₂ is due to the long F-F bond. The calculations indicate that there is an electrostatic driving force toward a shorter F-F bond.
4. The long F-F bond is a result of the kinetic energy component of E^{Pauli} , which produces a significantly larger destabilisation in the total energy in F₂ around r_{eqm} than in the other X₂ molecules. E^{elstat} cannot compensate for this change and the result is an inner wall of the potential well occurring at a longer bond distance for F₂ than would be predicted from the other diatomic halogens.

5. The greater rate of increase in E^{Pauli} for F_2 as the bond distance is decreased is due to the greater change in X-X atomic overlap as a function of r in F_2 compared with the heavier X_2 molecules.

These conclusions are therefore partly in agreement with most inorganic textbooks where the weakness of the F_2 bond is usually attributed to large electron-electron repulsion.^{55,56} However, it should be stated that this is in turn due to the behaviour of the Pauli repulsion and hence that the weak F_2 bond is a quantum mechanically-driven electrostatic effect.

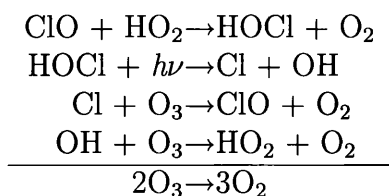
During the course of writing up this project it came to my attention that Estehuysen and Frenking have approached the problem of the nature of the chemical bond in molecules from group 15, group 17, CO and BF using the Ziegler-Rauk energy decomposition scheme as implemented in the ADF program.⁷³ They concluded that the weakness in the F_2 bond is due to a rather large Pauli repulsion energy, as I have shown. This result is clearly comforting as well as being of considerable interest, as it stems from the only study to date which employs the same methodology as mine.

Chapter 5

Investigations of the Potential Energy Surface of the ClO + HO₂ Reaction

5.1 Introduction

The reaction between the chlorine monoxide (ClO) and the hydroperoxy radical (HO₂) is important in atmospheric chemistry as it is believed to be involved in the destruction of ozone in the middle and lower stratosphere. The destruction cycle is:



The reaction of ClO with HO₂ has several possible reaction channels, although the channel (shown above), which leads to the formation of HOCl and O₂, is believed

to be the most important. Other possible reaction paths are shown in table 5.1. The reaction giving HCl and O₃ is exothermic but it has not been possible to observe the product ozone so far in experimental studies.

Table 5.1: Possible reaction channels for the ClO + HO₂ reaction.

		$\Delta_r H$ (298K)/kJ mol ⁻¹ (^a)
ClO + HO ₂ →	ClOO + OH	12
	OCIO + OH	25
	HOCl + O ₂	-191
	HClO + O ₂	71
	HCl + O ₃	-62

^a see reference 74–76

HOCl has a long lifetime and acts as a chlorine ‘reservoir’ which decreases the ozone destruction but, on the other hand, HOCl can undergo photo dissociation to form OH and Cl (as shown above), which accelerates the ozone destruction.

Experimental results show that the ClO + HO₂ reaction has complicated temperature dependence which suggests that the reaction takes place via one or more intermediates, but these are difficult to isolate and observe experimentally due to their short lifetimes.^{77–79} Therefore a number of computational studies have been carried out in recent years, using different levels of theory. Mozurkevich was the first to approach the problem computationally by carrying out a series of RRKM (Rice-Ramsperger-Kassel-Marcus) calculations on reactions of HO₂ with different radicals.⁸⁰ He found that the ClO + HO₂ reaction is most likely to take place through direct attack on the hydrogen by ClO to form HOCl and O₂.

Toohey and Anderson calculated the reaction between HO₂ and a number of atoms and radicals using UHF and MP2.⁸¹ They found that under C_s symmetry constraints the ClO + HO₂ → HOCl + O₂ reaction may have two mechanisms

on the triplet reaction surface; at low temperatures the ClO radical attacks the terminal oxygen of the bent HO₂ and forms a cyclic intermediate, whereas at high temperatures there is a direct attack on the hydrogen atom.

Buttar and Hirst studied both the triplet and singlet reaction surfaces of the ClO + HO₂ reaction without any symmetry constraints using RHF/UHF and MP2.⁸² They found that it was important to include correlation to be able to determine the saddle points correctly. On the triplet surface they found an intermediate from direct attack on the hydrogen atom as described by Toohey and Anderson. The forward path from this intermediate lead to the products HOCl and O₂ and the backward path resulted in a local minimum with a very low activation barrier. Buttar and Hirst found a singlet reaction surface that was more complex than the triplet surface. The multistep reaction takes place through ClO attacking the terminal oxygen to form a loosely bound intermediate, from which the hydrogen migrates to the ClO radical through a number of intermediates. The final product was found to be the same as on the triplet surface but with singlet oxygen, i.e. HOCl and O₂.

Nickolaisen *et al.* carried out calculations using a mixture of hybrid DFT (B3LYP) and coupled cluster methods to see if they could find any reaction path leading to the formation of HCl and O₃.⁸³ The singlet reaction surface that they found was even more complex than that found by Buttar and Hirst and consisted of three different paths. The most energetically favourable channel was similar to the path found at the RHF and MP2 levels of theory; the chlorine attacks the oxygen to form HOOClo and then forms a cyclic intermediate before finally falling apart into the products HOCl and O₂. The other two channels first form the very stable HOOOCl. This can then either form a cyclic intermediate before forming the products HCl and O₃, or form a cyclic intermediate which excludes the chlorine and then forms the

products HOCl and O₂. The activation barriers for these two channels are very high and the reaction is therefore not likely to take place through either of these paths. They found the triplet surface to be consistent with previous findings at UHF and MP2 level of theory.

Almost simultaneously to Nickolaisen *et al.*, Kaltsoyannis and Rowley carried out calculations of both the singlet and triplet energy surfaces at the CCD//CCSD(T) level of theory using the 6-311G** basis set.⁸⁴ The most favourable reaction path found by Nikolaisen *et al.*, the formation of HOCl and O₂(¹Δ) via the HOOCLO minimum, was found by coupled cluster theory to be unlikely to occur due to the high activation barrier (74 kJ/mol). The results obtained by Kaltsoyannis and Rowley will be discussed more in detail in section 5.3, as they are used as a starting point in this study.

To summarise the previous published computational results discussed above, it can be said that, independent of the level of theory, the formation of HOCl and O₂ on the triplet surface is found to be the most favourable path.

To my knowledge, no purely DFT-based calculations have previously been carried out on the ClO + HO₂ energy potential surface. Considering the computational benefits of using DFT compared to the much more expensive CCD//CCSD(T), it was interesting to see how well DFT performs and if it could be used for getting approximate starting structures for higher level *ab initio* calculations. Studies of other energy potential surfaces using DFT have shown that LDA methods are unreliable and should be used with caution, if at all.¹ GGA methods can give better results but the energy barriers are usually underestimated.

5.2 Computational Details

All calculations were carried out using the geometries found at the CCD level of theory as starting geometries, without any symmetry constraints.⁸⁴

All calculations using the ADF program were carried out using all-electron triple-zeta Slater type basis sets with one polarisation function (TZP) together with the Becke Perdew XC-functional (BP86) unless otherwise stated. Scalar relativistic corrections were included via the ZORA method. The ADF numerical integration parameter was set to 5, and the energy gradient convergence criterion was set to 1×10^{-4} au/Å in all geometry optimisations. The default settings were used for frequencies and IRC calculations.

All calculations using the Gaussian 98 program⁸⁵ were carried out using the default settings with the BP86 XC-functional and the 6-311G** basis sets. No relativistic effects were included.

5.3 Studies of the Potential Energy Surface using the ADF Program

5.3.1 Singlet Surface

Three different paths are found on the singlet surface at the CCD level of theory (see figure 5.1).⁸⁴ By using DFT, as implemented in the ADF program, all minima found by Kaltsoyannis and Rowley could be found but none of the transition states could be readily obtained. To establish if the problems in finding the transition states were due to the choice of exchange-correlation functional and basis set, a number of different XC-functionals (SVWN, BVWN, SLYP, BLYP and BP86) as well as different sizes of basis set (DZ, DZP and TZP) were employed. The high-energy transition state, **ts1** (see figure 5.2), could be found when employing a small basis set (DZ) with any of the above mentioned functionals. If a polarisation function was added to the basis set (DZP) the transition state search showed sensitivity towards the choice of XC-functional in that **ts1** could not be found when using the BVWN functional. By increasing the basis set further to the TZP level this sensitivity is enhanced and the transition state could only be obtained with the LDA or the SLYP functionals. This would suggest that a small basis set such as DZ is more stable for locating **ts1** than a bigger basis set.

In the search for **ts5** (see figure 5.2), the basis set and XC-functional were altered as above for **ts1** but the result of these alterations did not show any similarities with the trend seen in the search for **ts1**. When employing the DZ basis set, no transition state could be found independent of the choice of XC-functional and the calculations aborted while using electron smearing. Including a polarisation function

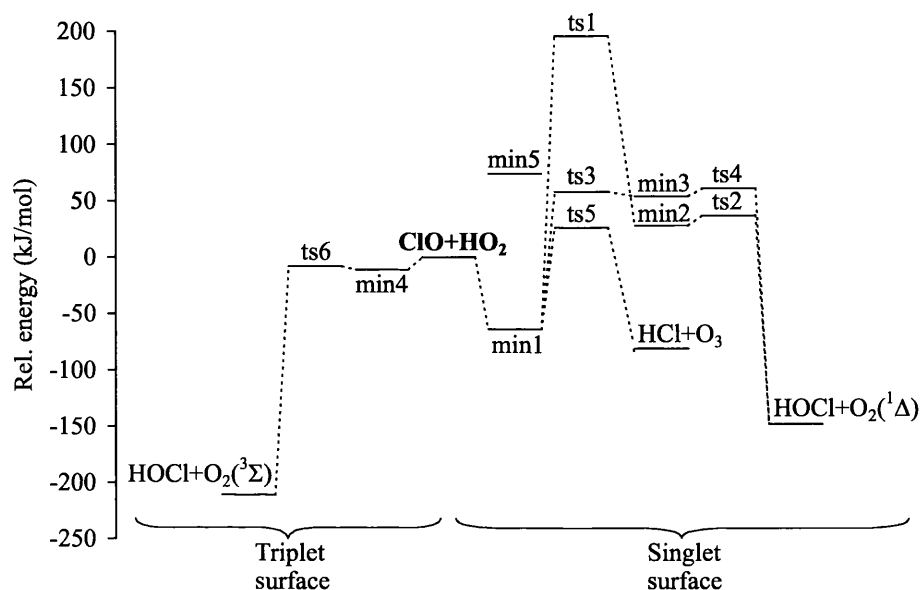


Figure 5.1: The energies of the stationary points on the ClO + HO₂ potential energy singlet and triplet surface relative to a zero for the reactants, as obtained at the CCD//CCSD(T) level of theory.

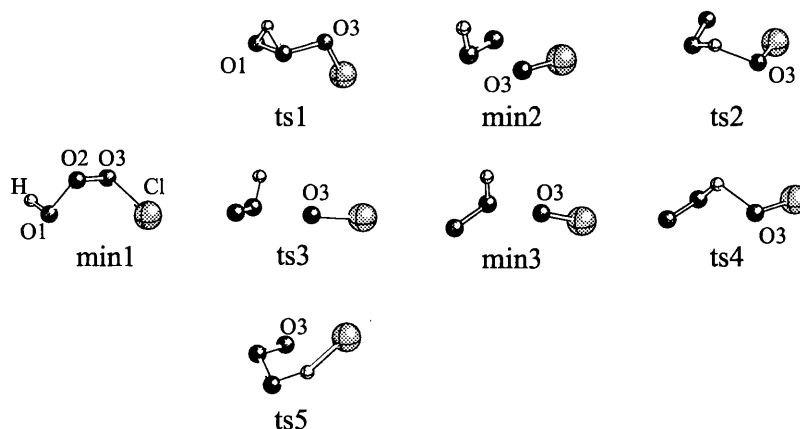


Figure 5.2: Ball and stick representations of the stationary points on the ClO + HO₂ singlet potential energy surface as obtained at CCD level of theory.

(DZP) gave a somewhat better result and a transition state could be found when employing either the BP86 or the BLYP functional. The TZP basis set showed further improvement and transition states were found when using any of the applied XC-functionals. Contrary to what is observed in the search for **ts1**, the larger TZP basis set now show more stability than the smaller DZ and DZP basis sets. This indicates that there is no specific trend in transition state searches like these, but only random results.

The search for the remaining transition states (**ts2**, **ts3** and **ts4** (see figure 5.2)) were carried out using only the parameters mentioned in section 5.2, i.e. the TZP basis set in conjunction with the BP86 functional. The first two of these transition states, **ts2** and **ts3**, could not be found at all whereas **ts4** was obtained and verified by its vibrational frequencies.

The IRC calculations from the transition states also proved to be problematic. Most points along the path corresponding to the imaginary mode of **ts1** (1524i cm^{-1} with the DZ basis set) did not converge and the final result was two almost identical structures which bore resemblance to the **min2** obtained by Kaltsoyannis and Rowley (see figure 5.2). As a result no path from other stationary points can be traced to this transition state. The IRC calculation on **ts4** proved to be even less successful and the calculation halted almost immediately due to problems with the electronic configuration. In an attempt to overcome this problem, the electronic configuration was frozen for a number of scf cycles but this only resulted in a non-Aufbau configuration as soon as this constraint was loosened and the process halted again.

The IRC calculations from **ts5** showed once again a dependence on the choice of basis set and XC-functional. A problem similar to that seen for **ts1** was observed for

ts5 when employing the DZP basis set, that is, two almost identical structures were found on both sides of the transition state. Both paths now lead to a minimum that either resembles **min1** (see figure 5.2) or the products, HCl and O₃. This problem was also observed when the bigger TZP basis set was employed in conjunction with the BLYP functional. However, this bigger basis set in conjunction with the BP86 or the VWN functional yielded a forward path that lead to the dissociated products of HCl and O₃ and a backward path that lead to a minimum. This minimum (**minA**) is similar to **min1** found by Kaltsoyannis and Rowley but with the hydrogen and the chlorine in *cis* conformation instead of *trans* (figure 5.3(a)). The transition state (see figure 5.3(b)) is almost identical to **ts5** found by Kaltsoyannis and Rowley, and will hereafter be referred to as **tsB** to avoid confusion. The cited energies and geometries for **tsB** will be those obtained with the TZP basis set and the BP86 functional.

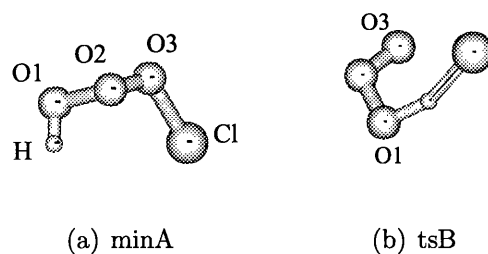


Figure 5.3: Ball and stick representations of the stationary points on the ClO + HO₂ singlet potential energy surface.

In figure 5.4 the only reaction path that could be found on the singlet potential energy surface is presented. Whereas **ts5** (figure 5.1) was found to be less stable than the reactants by 26 kJ/mol, **tsB** is more stable than the reactants by 34 kJ/mol. This difference should have a drastic effect on the kinetics of this reaction in that no activation energy is needed for the hydrogen abstraction of H by ClO from HO₂ at the

DFT level of theory and an increase in temperature would slow down the reaction, i.e. negative temperature dependence. Experimental studies of this reaction channel have shown that the ratio of $\text{HCl} + \text{O}_3$ increases at lower temperatures.^{78,86-88} A path to the products $\text{HOCl} + \text{O}_2(^1\Delta)$, which at the CCD//CCSD(T) level of theory were found to be more stable than the $\text{HCl} + \text{O}_3$ products, could not be found by using DFT.

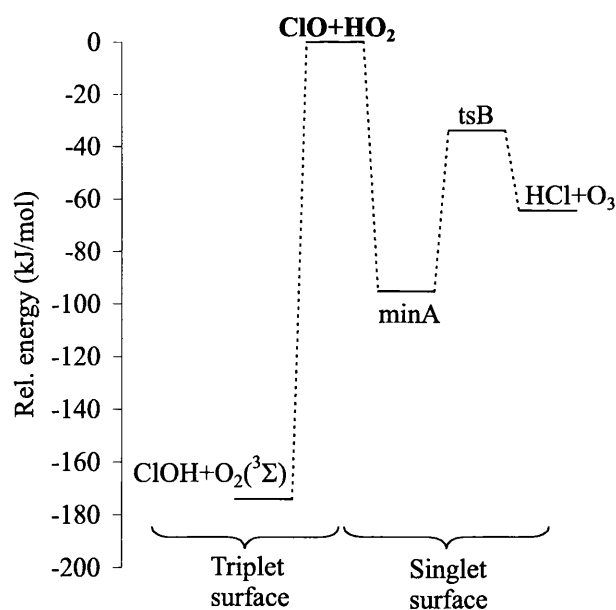


Figure 5.4: The energies of the stationary points on the $\text{ClO} + \text{HO}_2$ potential energy surface relative to a zero for the reactants using the BP86 functional and the TZP basis set.

5.3.2 Triplet Surface

Kaltsoyannis and Rowley found, at the CCD//CCSD(T) level of theory, that the reaction on the triplet surface takes place via a loosely bound intermediate (**min4**, figure 5.5), which dissociates to HOCl and O₂(³Σ) via **ts6** (see figure 5.1 and 5.5).⁸⁴ However, using DFT no intermediate structure analogous to **min4** could be found on the triplet surface. A transition state search for **ts6** and a minimum energy search for **min4** produced unconverged geometries tending towards the products HOCl and O₂.

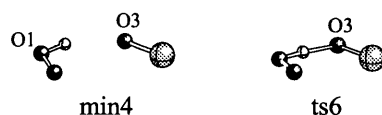


Figure 5.5: Ball and stick representations of the stationary points on the ClO + HO₂ triplet potential energy surface as obtained at CCSD(T) level of theory.

In order to probe this further, single point calculations were performed, using the geometric parameters of **ts6** and changing the O1-H distance stepwise. These showed no stationary point but a steadily stabilised energy from $r(\text{O1-H})=0.8\text{-}1.4$ Å. At longer distances than 1.4 Å, the energy is quickly destabilised again due to the hydrogen being forced too close to the O3 atom. At $r(\text{O1-H})=1.4$ Å the H-O3 distance is 1.01 Å. At the CCD level of theory **ts6** has an O1-H distance of 1.07 Å (indicated by the arrow in figure 5.6). The same type of single point calculations with the geometric parameters of **min4** caused problems with electron smearing at O1-H distances between 0.9 and 1.1 Å. This is the region in which **min4** was found by Kaltsoyannis and Rowley to have its optimised geometry ($r(\text{O1-H})=0.97$ Å, as indicated by the arrow in figure 5.6). These results, especially those obtained with

the **ts6** structure, support the findings that no stationary points are present in the region of the DFT triplet surface and that the reactants proceed in a barrierless manner directly to HOCl and O₂(³Σ) (figure 5.4).

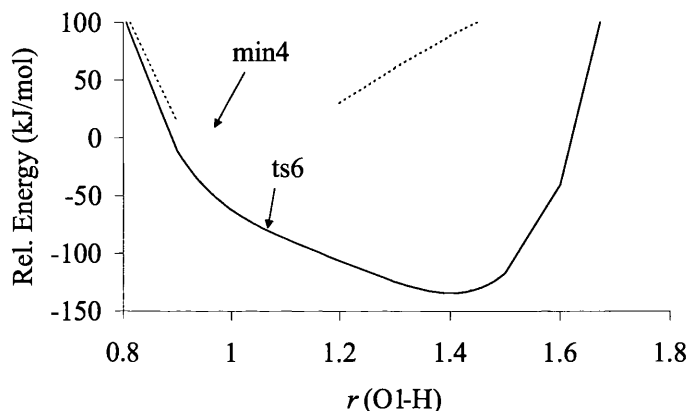


Figure 5.6: The relative energy as a function of the O1-H distance using **min4** (hashed line) or **ts6** (solid line) as the fixed geometry.

The activation barrier towards HOCl and O₂(³Σ) was found to be only 3 kJ/mol at the CCD//CCSD(T) level of theory (see figure 5.1) and since it is known that gradient corrected DFT methods somewhat underestimate energy barriers,¹ this activation barrier would be expected to be even lower in a DFT calculation. This may well lead to dissociation to the products without any intermediates, which is exactly what is seen here.

The DFT products (HOCl and O₂(³Σ)) are found to be 174 kJ/mol more stable than the reactants (ClO and HO₂). This is a somewhat smaller stabilisation than was found by Kaltsoyannis and Rowley⁸⁴ who found the reaction enthalpy on the triplet surface to be 211 kJ/mol.

5.4 Studies of the Potential Energy Surface using the Gaussian 98 Program

To investigate whether the problems with transition state searches and IRC calculations that were described in the previous section are due to the ADF program's inability to handle this type of radical reaction surface, or if it is a problem of DFT irrespective of the program used, an attempt to model the singlet potential energy surface using DFT (BP86) as implemented in Gaussian 98 was carried out.

By using the default settings, it was noted that, just as when using the ADF program, there are no problems in finding the minima that were found at the CCD level of theory. The problems arise in the transition state searches and the IRC calculations. **Ts1** (figure 5.1) could be found and was confirmed by analysis of its vibrational frequencies, but the IRC calculation only found a structure similar to **min2**. This minimum was found on both sides of the transition state using IRC in ADF. In the other direction, Gaussian 98 encountered scf convergence problems.

Scf convergence problems were seen in the transition state searches for **ts2** and **ts3**, consistent with ADF's inability to find **ts2** and **ts3**. An optimised structure was found for **ts4** but it bore no resemblance to the **ts4** obtained by Kaltsoyannis and Rowley. However, it was, just as **ts1**, confirmed as a transition state by its vibrational frequencies. The IRC calculation, resulted in a reaction path which, in both directions, found a structure with more or less the same geometry and energy as that of **ts4**. In ADF, no successful IRC path could be obtained for **ts4**.

The transition state search for **ts5** found a stationary point which was confirmed as a transition state, but which looked like the dissociated product HCl and O₃. The IRC calculation gave the same type of result as that observed for **ts4**, i.e. a path

in both directions giving end products of similar geometries and energies as the transition state. The path via **ts5** was the only reaction path that was found on the singlet surface using ADF.

Gaussian 98 therefore experiences similar problems to those seen in ADF for transition state searches and the following IRC calculations. This indicates that the problem lay within DFT itself and not its implementation in Gaussian 98 or ADF.

5.5 Conclusions

Two reaction channels were found using DFT as implemented in the ADF program. They show that the reaction can take place either on the triplet surface, to form HOCl and $O_2(^3\Sigma)$ without any activation barrier being present and with the products being 174 kJ/mol more stable than the reactants, or on the singlet surface, to form HCl and O_3 via a transition state which is 34 kJ/mol more stable than the reactants. The products on the singlet surface are stabilised by 65 kJ/mol compared to the reactants. The experimental value of -191 kJ/mol for the $ClO + HO_2 \rightarrow HOCl + O_2$ reaction corresponds well with the gain in energy calculated on the triplet surface (-174 kJ/mol).

Characterising the potential energy surface of the $ClO + HO_2$ reaction using DFT proved difficult. Whereas the minima found at the CCD level of theory could easily be obtained using DFT, the transition state searches and IRC calculations proved more complicated. It was found that this was not a problem specific to the ADF program but the Gaussian 98 program showed similar problems. This suggests that DFT calculations of the potential energy surface of radical reactions are not reliable and should not be trusted without backup of data obtained from more reliable methods such as high level *ab initio* or hybrid DFT. Given that one of the aims of this study was to establish if DFT can be used for initial mappings of the potential energy surfaces of radical-radical reactions, the conclusion must emphatically be that it should not.

Appendix A

Procedure for the synthesis of N,N'-bis(phenyl)-1,6- bis(triisopropylsilyl)-hexa-1,5- diyne-3,4-diimine palladium dichloride (compound 3, chapter 3)

88 mg (0.15 mmol) N,N'-bis(phenyl)-1,6-bis(triisopropylsilyl)-hexa-1,5-diyne-3,4-diimine (**1**) and 27 mg (0.15 mmol) palladium dichloride were dissolved in dichloromethane (20 mL) and refluxed for 15 hours. The solution was filtered through celite and the solvent was removed *in vacuo*. Any excess **1** was washed away with hexane to give the product as an orange solid (yield 54 mg, 0.07 mmol, 48 %).

IR: $\nu=2943\text{ cm}^{-1}$ (s, C-H str.); 2865 cm^{-1} (s, C-H str.); 2152 cm^{-1} (w, C \equiv C str.)

UV(CH₂Cl₂: $\lambda_{max}(\epsilon)$ =248 nm (22900); 298 nm (13400); 425 nm (12700)

¹H-NMR (CDCl₃, 500 MHz): δ =7.42(t, J=7.7, 4H, aromatic CH_m), 7.34(t, J=7.4, 2H, aromatic CH_p), 7.23(d, J=8.0, 4H, aromatic CH_o), 0.95-0.76 (m, 42H, CH, CH₃)

¹³C-NMR (CDCl₃, 125.8 MHz): δ =155.1(C=N), 146.5(C-N), 129.0(aromatic CH), 128.6(aromatic CH), 123.1(aromatic CH), 119.9(C≡C), 97.6(C≡C), 18.4(CH₃), 10.9(CH)

MS(FAB⁺), m/z(%): 711(7.31)[M⁺²-Cl], 570(12.9)[DAD⁺³], 284(10.56)[DAD⁺/2]

m.p.: 238-240°C

Bibliography

- [1] W. K. Koch and M. C. Holthausen. *A Chemist's Guide to Density Functional Theory*. Wiley-VCH, 2 edition, 2001.
- [2] J. C. Slater. *Phys. Rev.*, 81(3):385, 1951.
- [3] S. H. Vosko, L. Wilko, and M. Nusair. *Can. J. Phys.*, 58:1200–1211, 1980.
- [4] A. D. Becke. *Phys. Rev. A*, 38:3098–3100, 1988.
- [5] J. P. Perdew and Y. Wang. *Phys. Rev. B*, 33(12):8800–8802, 1986.
- [6] J. P. Perdew, J. A. Chevary, S. H. Vosko, K. A. Jackson, M. R. Pederson, D. J. Singh, and C. Fiolhais. *Phys. Rev. A*, 46(11):6671–6687, 1992.
- [7] C. Lee, W. Yang, and R. G. Parr. *Phys. Rev. B*, 37(2):785–789, 1988.
- [8] B. G. Johnson, P. M. W. Gill, and J. A. Pople. *J. Chem. Phys.*, 98(7):5612–5626, 1993.
- [9] T. V. Russo, R. L. Martin, and P. J. Hay. *J. Chem. Phys.*, 101(9):7729–7737, 1994.
- [10] J. P. Perdew. *Phys. Rev. B*, 33:8822–8824, 1986.

- [11] P. J. Stephens, F. J. Devlin, C. F. Chabalowski, and M. J. Frisch. *J. Phys. Chem.*, 98(45):11623–11627, 1994.
- [12] S. J. A. van Gisbergen, J. G. Snijders, and E. J. Baerends. *Comput. Phys. Commun.*, 118:119–138, 1999.
- [13] M. Petersilka, U. J. Gossmann, and E. K. U. Gross. *Phys. Rev. Lett.*, 76(8):1212–1215, 1996.
- [14] S. J. A. van Gisbergen, J. A. Groeneveld, A. Rosa, J. G. Snijders, and E. J. Baerends. *J. Phys. Chem. A*, 103(34):6835–6844, 1999.
- [15] E. K. U. Gross and W. Kohn. *Adv. in Quant. Chem.*, 21:255, 1990.
- [16] N. Kaltsoyannis. *Chem. Soc. Rev.*, 32:9–16, 2003.
- [17] F. Jensen. *Introduction to computational chemistry*. Wiley, Chichester, 1999.
- [18] E. van Lenthe, A. Ehlers, and E. J. Baerends. *J. Chem. Phys.*, 110(18):8943–8953, 1999.
- [19] ADF2.3, 1999, 2000 and 2002, Department of Theoretical Chemistry, Vrije Universiteit, Amsterdam.
- [20] E. J. Baerends, D. E. Ellis, and P. Ros. *Chem. Phys.*, 2:41–51, 1973.
- [21] L. Versluis and T. Ziegler. *J. Chem. Phys.*, 88(1):322–328, 1988.
- [22] G. te Velde and E. J. Baerends. *J. Comp. Phys.*, 99:84–98, 1992.
- [23] C. Fonseca Guerra, J. G. Snijders, G. te Velde, and E. J. Baerends. *Theor. Chem. Acc.*, 99:391–403, 1998.

- [24] G. te Velde, F. M. Bickelhaupt, E. J. Baerends, S. J. A. van Gisbergen, C. Fonseca Guerra, J. G. Snijders, and T. Ziegler. *J. Comput. Chem.*, 22(9):931–967, 2001.
- [25] C. C. Pye and T. Ziegler. *Theor. Chem. Acc.*, 101:396–408, 1999.
- [26] A. Klamt and G. Schüürmann. *J. Chem. Soc. Perkin Trans. 2*, pages 799–805, 1993.
- [27] A. Klamt. *J. Phys. Chem.*, 99(7):2224–2235, 1995.
- [28] A. Klamt. *J. Phys. Chem.*, 100:3349–3353, 1996.
- [29] J. L. Pascual-Ahuir, E. Silla, and I. Tuñon. *J. Comput. Chem.*, 15(10):1127–1138, 1994.
- [30] F. M. Bickelhaupt and E. J. Baerends. *Reviews in Computational Chemistry*, volume 15, pages 1–86. Wiley-VCH, New York, 2000.
- [31] T. Ziegler and A. Rauk. *Theoret. Chim. Acta*, 46:1–10, 1977.
- [32] T. Ziegler and A. Rauk. *Inorg. Chem.*, 18(6):1558–1565, 1979.
- [33] For details on both MOLDEN and ADFFrom99, see <http://www.caos.kun.nl/~schaft/molden/molden.html>.
- [34] D. D. Perrin and W. L. F. Armarego. *Purification of Laboratory Chemicals*. Pergamon, New York, 3 edition, 1988.
- [35] B. Göbelt. PhD thesis, University of Heidelberg, 1999.

- [36] G. J. P. Britovsek, S. Mastroianni, G. A. Solan, S. P. D. Baugh, C. Redshaw, V. C. Gibson, A. J. P. White, D. J. Williams, and M. R. J. Elsegood. *Chem. Eur. J.*, 6(12):2221–2231, 2000.
- [37] G. van Koten and K. Vrieze. *Adv. Organomet. Chem.*, 21:151–239, 1982.
- [38] K. Vrieze. *J. Organometallic Chem.*, 300:307–326, 1986.
- [39] R. Faust, B. Göbelt, and C. Weber. *Synlett*, pages 64–66, 1998.
- [40] R. Faust, B. Göbelt, C. Weber, C. Krieger, M. Gross, J.-P. Gisseelbrecht, and C. Boudon. *Eur. J. Org. Chem.*, pages 205–214, 1999.
- [41] J. Fabian. *Chem. Rev.*, 92(6):1197–1226, 1992.
- [42] J. H. Flanagan Jr., C. V. Owens, S. E. Romero, E. Waddell, S. H. Kahn, R. P. Hammer, and S. A. Soper. *Anal. Chem.*, 70(13):2676–2684, 1998.
- [43] R. Bonnett. *Rev. Contemp. Pharmacother*, 10:1–17, 1999.
- [44] L. E. Forslund, R. Faust, and N. Kaltsoyannis. *J. Chem. Soc. Perkin Trans. 2*, 2:494–501, 2002.
- [45] N. N. Matsuzawa, A. Ishitani, D. A. Dixon, and T. Uda. *J. Phys. Chem.*, 105:4953–4962, 2001.
- [46] D. J. Tozer, R. D. Amos, N. C. Handy, B. O. Roos, and L. Serrano-Andrés. *Mol. Phys.*, 97(7):859–868, 1999.
- [47] H. H. Heinze, A. Görling, and N. Rösch. *J. Chem. Phys.*, 113(6):2088–2099, 2000.

- [48] P. Boulet, H. Chermette, C. Daul, F. Gilardoni, F. Rogemond, J. Weber, and G. Zuber. *J. Phys. Chem. A*, 105(5):885–894, 2001.
- [49] K.P. Huber and G. Herzberg. *Molecular spectra and molecular structure, IV. Constants of diatomic molecules*. Van Nostrand Reinhold, New York, 1979.
- [50] K.S. Pitzer. *J. Chem. Phys.*, 23:1735, 1955.
- [51] G.L. Caldow and C.A. Coulson. *Trans. Faraday Soc.*, 58:633–641, 1962.
- [52] R.S. Mulliken. *J. Am. Chem. Soc.*, 77:884–887, 1955.
- [53] L. Pauling. *The nature of the chemical bond*. Cornell University Press, Ithaca, N.Y., 3rd edition, 1960.
- [54] W.L. Jolly and C.J. Eyermann. *Inorg. Chem.*, 22:1566, 1983.
- [55] C. E. Housecroft and A. G. Sharpe. *Inorganic Chemistry*. Prentice Hall, Harlow, 2001.
- [56] D. F. Shriver and P. W. Atkins. *Inorganic Chemistry*. OUP, Oxford, 3rd edition, 1999.
- [57] L. E. Forslund and N. Kaltosyannis. *New J. Chem.*, 27:1108–1114, 2003.
- [58] K. A. Peterson, R. A. Kendall, and T. H. Dunning Jr. *J. Chem. Phys.*, 99:9790–9805, 1993.
- [59] M. R. A. Blomberg and P. E. M. Siegbahn. *Chem. Phys. Lett.*, 81(1):4–13, 1981.
- [60] L.A. Curtiss, B.C. Redfern, B.J. Smith, and L. Radom. *J. Chem. Phys.*, 104:5148–5152, 1996.

- [61] P.C. Redfern, J.-P. Blaudeau, and L.A. Curtiss. *J. Phys. Chem. A*, 101:8701–8705, 1997.
- [62] A.G. Császár and W.D. Allen. *J. Chem. Phys.*, 104:2746–2748, 1996.
- [63] J. M. L. Martin and O. Uzan. *Chem. Phys. Lett.*, 282:16–24, 1998.
- [64] J.P. Perdew, S. Kurth, A. Zupan, and P. Blaha. *Phys. Rev. Lett.*, 82:2544–5179, 1999.
- [65] F. Moscardó, A. J. Pérez-Jiménez, and J. Américo Cjuno. *J. Comput. Chem.*, 19:1899–1908, 1998.
- [66] M. Filatov and W. Thiel. *Phys. Rev. A*, 57:189–199, 1998.
- [67] K. Hijikata. *Rev. Mod. Phys.*, 32(2):445–446, 1960.
- [68] K. Hijikata. *J. Chem. Phys.*, 34(1):231–239, 1961.
- [69] G. Das and A. C. Wahl. *J. Chem. Phys.*, 44(1):87–96, 1966.
- [70] G. Das and A. C. Wahl. *Phys. Rev. Lett.*, 24(9):440–443, 1970.
- [71] G. Das and A. C. Wahl. *J. Chem. Phys.*, 56(7):3532–3540, 1972.
- [72] J. Pittner, J. Šmydke, P. Čársky, and I. Hubač. *J. of Mol. Str. Theochem*, 547:239–244, 2001.
- [73] C. Esterhuysen and G. Frenking. *Theor. Chem. Acc.* in press.
- [74] J. D. Cox, D. D. Wagman, and V. A. Medvedev. *CODATA. Key Values for Thermodynamics*. Hemisphere Publishing, New York, 1989.

- [75] M. W. Chase Jr. *NIST-JANAF Thermochemical Tables*. National Institute of Standards, New York, 4 edition, 1998.
- [76] G. Hirsch, P. J. Bruna, S. D. Peyerimhoff, and R. J. Buenker. *Chem. Phys. Lett.*, 52(3):442–448, 1977.
- [77] F. C. Cattell and R. A. Cox. *J. Chem. Soc. Faraday Trans. 2*, 82:1413–1426, 1986.
- [78] T. J. Leck, J. L. Cook, and J. W. Birks. *J. Chem. Phys.*, 72(4):2364–2373, 1980.
- [79] R. M. Stimpfle, R. A. Parry, and C. J. Howard. *J. Chem. Phys.*, 71(12):5183–5190, 1979.
- [80] M. Mozurkewich. *J. Phys. Chem.*, 90:2216–2221, 1986.
- [81] D. W. Toohey and J. G. Anderson. *J. Phys. Chem.*, 93:1049–1058, 1989.
- [82] D. Buttar and D. M. Hirst. *J. Chem. Soc. Faraday Trans.*, 90(13):1811–1817, 1994.
- [83] S. L. Nickolaisen, C. M. Roehl, L. K. Blakeley, R. R. Friedl, J. S. Francisco, R. Liu, and S. P. Sander. *J. Phys. Chem. A*, 104:308–319, 2000.
- [84] N. Kaltsoyannis and D. M. Rowley. *Phys. Chem. Chem. Phys.*, 4:419–427, 2002.
- [85] M. J. Frisch, G. W. Trucks, H. B. Schlegel, G. E. Scuseria, M. A. Robb, J. R. Cheeseman, V. G. Zakrzewski, J. A. Montgomery Jr., R. E. Stratmann, J. C. Burant, S. Dapprich, J. M. Millam, A. D. Daniels, K. N. Kudin, M. C. Strain, O. Farkas, J. Tomasi, V. Barone, M. Cossi, R. Cammi, B. Mennucci, C. Pomelli,

C. Adamo, S. Clifford, J. Ochterski, G. A. Peterson, P. Y. Ayala, Q. Cui, K. Morokuma, D. K. Mailck, A. D. Rabuck, K. Raghavachari, J. B. Foresman, J. Cioslowski, J. V. Ortiz, B. B. Stefanov, G. Liu, A. Liashenko, P. Piskorz, I. Komaromi, R. Gomperts, R. L. Martin, D. J. Fox, T. Keith, M. A. Al-Laham, C. Y. Peng, A. Nanayakkara, C. Gonzalez, M. Challacombe, P. M. W. Gill, B. Johnson, W. Chen, M. W. Wong, J. L. Andres, M. Head-Gordon, E. S. Replogle, and J. A. Pople. Gaussian 98. Gaussian Inc., 1998.

[86] J. P. Burrows and R. A. Cox. *J. Chem. Soc. Faraday Trans. 1*, 77:2465–2479, 1981.

[87] M. Finkbeiner, J. N. Crowley, O. Horie, R. Müller, G. K. Moortgat, and P. J. Crutzen. *J. Phys. Chem.*, 99(44):1624–16275, 1995.

[88] G. P. Knight, T. Beiderhase, F. Helleis, G. K. Moortgat, and J. N. Crowley. *J. Phys. Chem. A*, 104(8):1874–1685, 2000.